Studying Cool Dwarfs and their Mass Function using infrared surveys

NIALL DEACON

Institute for Astronomy

School of Physics

Doctor of Philosophy

The University of Edinburgh

2006

Abstract

Anyone seeking to understand the physical processes of star formation must make reference to the spectrum of masses (mass function) produced by such processes. The low mass end of this mass function in particular is poorly constrained.

The two leading environments in which to measure the mass function are in open clusters and star forming regions and in the solar neighbourhood. Studies of some star forming regions claim to constrain the mass function down to a few tens of Jupiter masses. However the validity of results in young clusters and star forming regions has been called into question, with the accuracy of the evolutionary models that all studies are based on being considered debatable at young ages. Hence a study in the field, where there is a spread of ages, provides a useful, possibly more robust, method for measuring the mass function.

Low mass stars and brown dwarfs in the field are usually identified by either infrared surveys or by proper motion surveys. Here these techniques are combined for the first time to produce an infrared proper motion survey. This has produced a sample of over 7000 low mass objects with proper motions greater than 0.1"/yr. It has also found several common proper motion binary systems and SIPS1259-4336, an M8.5 dwarf within 10pc.

This sample on its own will not yield a constraint on the mass function. In the field the range of ages and the luminosity evolution of objects leads to the mass function being intertwined with the stellar birthrate. Here this problem is dealt with by detailed simulations. By drawing ages from a birthrate and masses from a mass function, simulated objects can have space positions, velocities and absolute magnitudes assigned using a simple model of the Galaxy, evolutionary models of low mass objects and empirical relations. These can then be converted into observables and passed through

a survey selection mechanism. By varying the underlying birthrate and mass function the effect these have on the survey results can be found. These results can then be compared with those of the actual survey to constrain the mass function and birthrate.

Here the mass function parameter α is found to be 0.66 ± 0.44 in the range $0.2\mathrm{M}_{\odot} > m > 0.075\mathrm{M}_{\odot}$, that the birthrate parameter β is -0.01 ± 0.10 and that the space density of objects in the mass range $0.09\mathrm{M}_{\odot} < m < 0.1\mathrm{M}_{\odot}$ is $0.0053 \pm 0.0002/\mathrm{pc}^3$. It should be noted that due to noise in the probability surface, the constraint on β should be treated with caution.

Finally the results of the future infrared surveys by UKIDSS are simulated and the potential constraints that could be set by them outlined.

Declaration

I declare that this thesis is not substantially the same as any that I have submitted for a degree or diploma or other qualification at any other University. I further state that no part of my thesis has already been or is being concurrently submitted for any such degree, diploma or other qualification.

This thesis is the outcome of my own work except where specifically indicated in the text.

Contents

List of Figures

List of Tables

Acknowledgements

I'd like to thank my family, my supervisors Nigel Hambly and John Cooke, everyone at the Royal Observatory Edinburgh who helped me with various things and those at other institutions who provided useful comments and data.

Chapter 1

Preface

1.1 Motivation

The nature of the physical mechanisms which result in the spectrum of stellar masses is one of the most fundamental open questions left in astrophysics at the start of this century. One of the main constraints that can be set on models of star formation is that the range of masses produced is in good agreement with that observed in the local universe. Currently the numbers of cool dwarfs (objects cooler than approximately 3500K) are not well constrained, hence the constraints for star formation set by their statistics are poor.

While the number of cool dwarfs provides an important measuring rod for star formation theorists both it and their birthrate have wider ramifications for other areas of astrophysics. Low mass stars have lifetimes much greater than a Hubble time, while brown dwarfs simply cool with time. Therefore they can be considered sinks for baryonic matter. Hence the number of low mass stars and brown dwarfs that exist will impact on how much baryonic mass is locked up in such objects and therefore unavailable for star formation. Better constraints on the low mass spectrum of masses will help to constrain this idle mass and hence improve models of galaxy evolution.

The measurement of the stellar birthrate is a bye-product of measuring the distribution of masses of cool dwarfs in the field. The stellar birthrate in an individual galaxy will be affected by the way that galaxy formed. If a galaxy formed quickly star formation would be much more common in the past meaning available gas would have

been hoovered up leaving a population of low mass stars which are old and cool. Conversely a gentle formation scenario (more likely for a spiral galaxy like our own) will have a virtually constant star formation rate, possibly trailing off as less gas becomes available for star formation. In addition the accretion of or encounters with smaller satellite galaxies will lead to spikes in the birthrate.

Finally individual, low mass objects could provide interesting information on atmospheric physics or stellar multiplicity. In particular, objects close to the boundary between the L and T spectral types could help to identify the reasons for this sudden shift in spectral type. Any information on this will feed back into models of giant planets.

For an overview of the subject area see Reid & Hawley (2005).

1.1.1 Cool Dwarfs In The Field

Studies in open clusters allow an easy determination of the mass function (a histogram binned in intervals of $\mathrm{d}\log_{10}\mathrm{m}$) as all the stars in the sample are of the same age. Hence the cluster's luminosity function (LF, a histogram binned by luminosity) can be easily converted into a mass function using a single mass-luminosity relation. However stars in the field will have a range of ages and as objects' luminosities evolve with time (e.g. brown dwarfs lack any internal energy source and hence cool with time) a single mass-luminosity relation cannot be used. So in order to measure the mass function in the field, the creation function (CF, the number of objects formed per unit volume per unit time in a mass interval $\mathrm{d}\log\mathrm{m}$), which is a combination of the mass function and the stellar birthrate (the number of objects formed per unit time), must first be considered. Next computational and theoretical models for the luminosity evolution of stars can be used to convert this to an LF. This can then be compared to the observed LF to see if the CF used is accurate.

1.2 Thesis Structure

In the next two chapters background material on both the bulk statistical properties (mass function and birthrate) and the individual properties (internal and atmospheric physics) of low mass stars and brown dwarfs will be outlined. Next, details of the

Southern Infrared Proper Motion survey (see Deacon et al. 2005a and Deacon & Hambly 2007a) will be given, outlining the methods used and the objects discovered. Follow-up observations on these will be detailed in a separate chapter. Details of these follow-up observations can also be found in Deacon et al. (2005a) and Deacon et al. (2005b). The simulations of the results of this infrared survey will be described in the next chapter leading to constraints on the mass function and birthrate (Deacon & Hambly, 2007b). The potential results of future, similar surveys will also be shown (Deacon & Hambly, 2006).

Chapter 2

The Stellar Initial Mass Function And Birthrate

The initial stellar mass function and the stellar birthrate are two of the most fundamental statistical distributions in stellar astrophysics. As stars (and brown dwarfs) evolve in luminosity over time, any description Galactic stellar population needs both the distribution of stellar masses (initial mass function) and the distribution of stellar ages (the birthrate). These two must be combined to study the cool dwarf population. This combination of the initial mass function and birthrate was defined by Miller & Scalo (1979) to be the creation function,

$$C(\log m, t) = \xi(\log_{10} m)\frac{b(t)}{T_{\rm G}} \tag{2.1}$$

where $\xi(\log_{10} m)$ is the initial mass function, $b(t)$ is the relative birthrate and $T_{\rm G}$ is the age of the Galaxy.

The initial mass function is defined to be the number of stars in a volume V formed at time t in a mass interval $d\log_{10} m$. By assuming that there is no post main sequence evolution of low mass stars (a sensible assumption given their lifetimes are greater than a Hubble time), that there is not a significant interacting binary population [1] and using the time independent mass function assumption from the creation function it is possible

[1] Ramsay & Hakala (2005) identify 45 short period variables from a sample of over thirty thousand objects, half of which are pulsating variables. It is therefore sensible to assume that the alteration of the Mass Function caused by mass transfer in interacting binaries will be very small.

to consider the initial mass function (IMF, that produced by star formation) and the present day mass function (PDMF, that observed) as the same thing. Hence here the distribution of stellar masses is simply described as the mass function. The definition of the mass function is shown below,

$$\xi(\log_{10} m) = \frac{dn}{d\log_{10} m} \tag{2.2}$$

where n is the number density $n = N/V$.

Often the mass function is quoted in linear (rather than logarithmic) units. This is more correctly called the mass spectrum (Scalo, 1986),

$$\psi(m) = \frac{dn}{dm} \tag{2.3}$$

Often authors refer to this as the mass function, hence vigilance as to what form they are in fact using is required [2].

The two most commonly used forms for the mass function (and mass spectrum) are the power law,

$$\begin{aligned} \xi(\log_{10} m) &\propto m^{-\alpha} \\ \psi(m) &\propto m^{-\alpha} \end{aligned} \tag{2.4}$$

and the lognormal,

$$\begin{aligned} \xi(\log_{10} m) &= \frac{A}{\sqrt{2\pi}\sigma} \exp\{-\frac{(\log_{10} m - \log_{10} m_c)^2}{2\sigma^2}\} \\ \psi(m) &= \frac{A}{\sqrt{2\pi}\sigma} \exp\{-\frac{(\log_{10} m - \log_{10} m_c)^2}{2\sigma^2}\} \end{aligned} \tag{2.5}$$

where $\log_{10} m_c$ is some mean characteristic mass and σ is the standard deviation of the distribution.

Also the lognormal mass function and mass spectrum are sometimes quoted as a parabola in log-log space.

$$\begin{aligned} \log_{10} \xi(\log_{10} m) &= a_0 + a_1 \log_{10} m + a_2 (\log_{10} m)^2 \\ \log_{10} \psi(m) &= a_0 + a_1 \log_{10} m + a_2 (\log_{10} m)^2 \end{aligned} \tag{2.6}$$

Stellar masses are only directly observable in multiple systems. It is more common to measure the luminosity function (LF) (see Equation 2.7 below) and convert this to

[2] Note that for ease of comparison for the reader, any studies referenced here which use a power law, mass spectrum will have their power law indices converted into the index of the appropriate mass function. Hence in all cases the α is the index of the mass function not the mass spectrum.

a mass function using a mass-luminosity relation.

$$\phi(M) = \frac{dn}{dM} \tag{2.7}$$

The birthrate used in this thesis is the relative birthrate, i.e. the absolute birthrate divided by the mean birthrate. This is shown below,

$$b(t) = \frac{dn/dt}{n_{tot/T_G}} \tag{2.8}$$

Some authors also refer to the star formation rate (SFR). This is simply the amount of mass converted into stars per year and can be converted to the absolute birthrate by dividing by the mean mass of a star.

For an overview of the stellar mass function see Chabrier (2003b).

2.1 Observational studies of the Mass Function

The Mass Function has been studied over a wide range of masses and in many different environments. Here the study of the low mass Mass Function $M < 0.5M_{\odot}$ in the field, clusters and star forming regions is focused on. However the high-mass Mass Function $M > 5M_{\odot}$ is also looked at to compare the Galactic Mass Function with those found in extragalactic studies (Massey et al., 1995).

2.1.1 Observational studies of the Disk Mass Function

The definitive paper in the observational study of the Galactic Disk Mass Function is Salpeter (1955). This builds on the earlier work of Luyten (1941) and Van Rhijn (1936). After separating out giants, subgiants and white dwarfs, Salpeter finds that the mass function for main sequence stars with masses ranging from $0.4 - 10M_{\odot}$ is well fitted by a power law. The value of α (the index of the power law Mass function times minus one) is found to be 1.35.

Recent studies of the IMF have focused on its variation from the Salpeter form. Miller & Scalo (1979) used similar techniques to Salpeter. Their work was based on the Luminosity Functions of Wielen (1974), Luyten (1968) and McCluskey (1966). This was converted into a PDMF using a mass-luminosity relation derived from the literature. Non-main sequence stars were also removed. In addition to this they took the novel

approach of collapsing their Mass Function down onto the Galactic Plane to remove scale height effects. Their results showed that the PDMF flattened off below $0.5M_{\odot}$. This led them to conclude that the mass was distributed lognormally.

In recent years several groups have used these techniques to both improve the determination of the Mass Function in the regions previously studied and to extend these studies to lower masses.

Reid et al. (2002) utilities Hipparcos data in addition to their own allowing them to create a volume complete sample of stars down to $M_V = 15.5$. They have used this V band solar neighbourhood Luminosity Function to produce a (after corrections for binarity) local field Mass Function. They fit a broken power law with the region $0.1M_{\odot} < m < 1.0M_{\odot}$ being fitted by $\alpha = 1.35 \pm 0.2$. They also use a volume limited 8pc sample in which this region is fitted by $\alpha = 1.15 \pm 0.2$. Kroupa (2001), building on the studies of others while examining underlying problems such as binarity, finds that the IMF is well fitted by a four segment power law such that for $0.01M_{\odot} < m < 0.08M_{\odot}$ being fitted by $\alpha = -0.7 \pm 0.7$, $0.08M_{\odot} < m < 0.5M_{\odot}$ by $\alpha = 0.3 \pm 0.5$, $0.5M_{\odot} < m < 1.0M_{\odot}$ by $\alpha = 1.3 \pm 0.3$ and $1.0M_{\odot} < m$ by $\alpha = 1.3 \pm 0.7$. Allen et al. (2005) use a series of assumptions about the birthrate and a Bayesian method to yield a value of -0.7 in the range $0.04M_{\odot} < m < 0.1M_{\odot}$. Chabrier (2001) uses both V and K band volume limited 5pc Luminosity Functions to produce a Mass Function well fitted by a lognormal form. The parameters of this are $m_0 = 0.08M_{\odot}$ and $\sigma = 0.79$.

2.1.2 Observational Studies of the IMF in Open Clusters and Star Forming Regions

Open Clusters and Star Forming Regions (SFR) provide an easier route to measuring the stellar IMF. As the objects in such environments are all created at a similar time they are all of the same age. Hence a single isochrone is required to model the Luminosity Function. This means the IMF is not entangled with the Birthrate. Studies of such clusters do however have their problems, the main one being background contamination. There are two methods for dealing with this photometric selection where photometric properties (such as position on a colour-magnitude diagram) are used to select out background objects and astrometric studies where the cluster's common proper

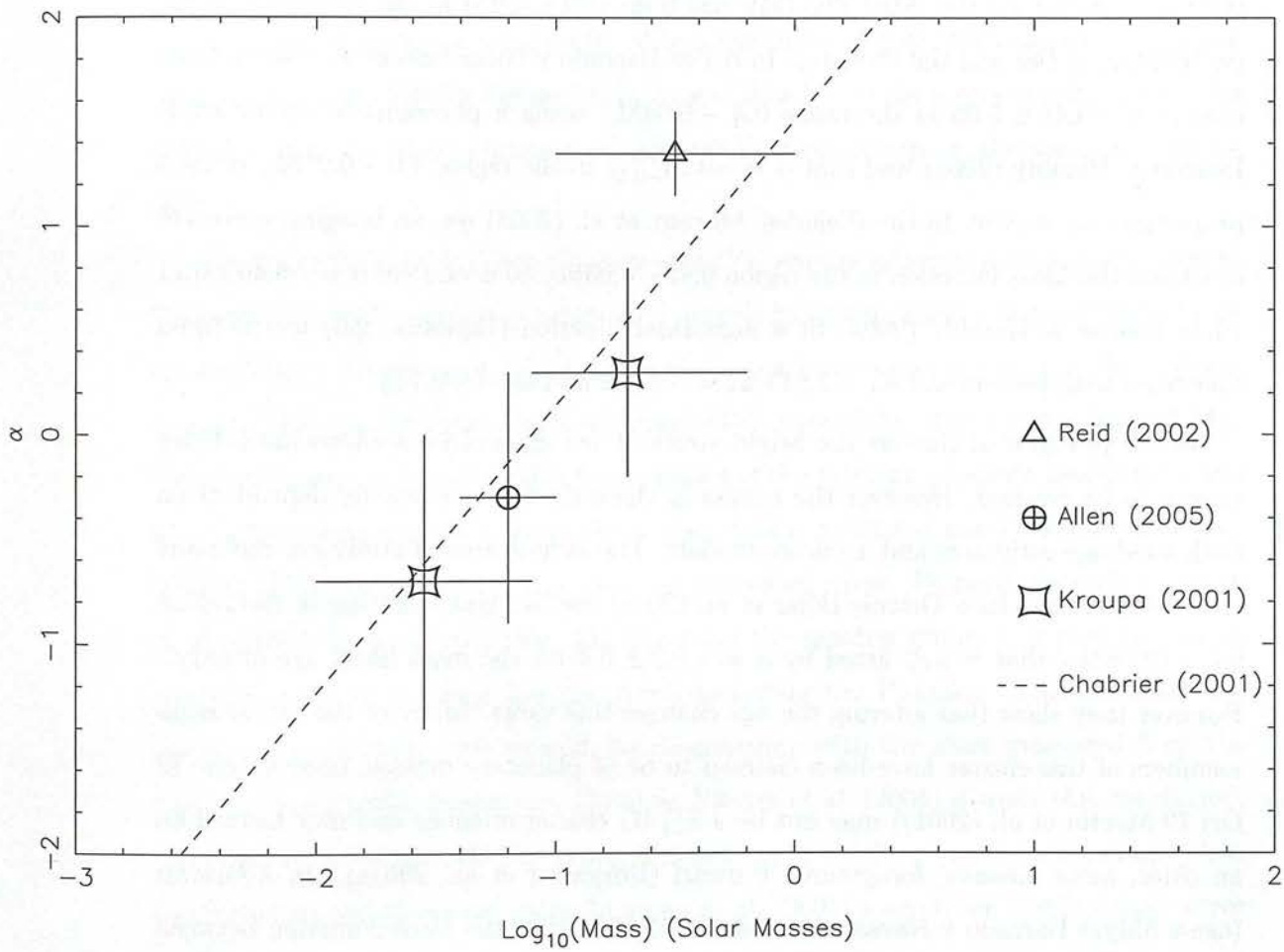

Figure 2.1: A plot showing the results of different studies of the mass function. The values of α are shown along with their errors. The error bars in the x-axis represent a range in mass rather than an error. Only studies of the mass function in the field are shown here.

motion is used as a discriminator.

In older clusters such as the Hyades (age$\approx$ 50Myr) there is a dearth of low mass objects Dobbie et al. (2002). This is most likely due not to a change in the IMF but due to dynamical evolution. Hence younger clusters than this must be studied to yield information on the IMF. The IMF has been well studied in the intermediate age ($\approx$ 100Myr) α Per and the Pleiades. In α Per Barrado y Navascués et al. (2002), finds that $\alpha = -0.41 \pm 0.05$ in the range $0.3 - 0.04\mathrm{M}_{\odot}$ using a photometric survey while Deacon & Hambly (2004) find that $\alpha = -0.14^{+0.14}_{-0.19}$ in the region $1.0 - 0.25\mathrm{M}_{\odot}$ using a proper motion survey. In the Pleiades, Moraux et al. (2003) use an imaging survey to constrain the Mass Function in the region $0.48 - 0.03\mathrm{M}_{\odot}$ to a value of $\alpha = -0.40 \pm 0.11$ while Deacon & Hambly (2004) fit a lognormal function (Equation 2.6) to the Mass Spectrum with parameters $a_0 = 2.213, a_1 = -2.069$ and $a_2 = -0.745$.

In the youngest of clusters the bright youth of low mass objects allows much lower masses to be reached. However the results in these clusters are heavily dependent on both good age estimates and accurate models. The richest area of study are the many clusters in Orion. In σ Orionis Béjar et al. (2001) find a Mass Function in the region $0.2 - 0.005\mathrm{M}_{\odot}$ that is well fitted by $\alpha = -0.2 \pm 0.4$ for the most likely age of 5Myr. However they show that altering the age changes this value. Many of the lowest mass members of this cluster have been claimed to be of planetary masses, however one (S Ori 70 Martín et al. (2001)) may not be a $3^{+5}_{-1} M_{\mathrm{J}}$ cluster member and may instead be an older, more massive, foreground T dwarf (Burgasser et al., 2004a). In λ Orionis (age$\approx$ 5Myr) Barrado y Navascués et al. (2004) find that the Mass Function between $0.14 - 0.03 M_{\odot}$ has $\alpha = -0.4 \pm 0.06$. In the Orion Nebula Cluster, Slesnick et al. (2004) find that the CF peaks at around $0.2\mathrm{M}_{\odot}$ and may have a small secondary peak around $0.05\mathrm{M}_{\odot}$. Finally in the Trapezium Cluster, Lucas et al. (2005) finds that the Mass Function peaks at around $0.15 M_{\odot}$ for an age of 1Myr or at $0.6\mathrm{M}_{\odot}$ for an age of 10Myr [3].

In the ρ Ophiuchi star forming region Luhman & Rieke (1999) find that the Mass Function peaks at $0.4\mathrm{M}_{\odot}$ and declines with a slope of $\alpha \approx -0.5$ down to $0.02\mathrm{M}_{\odot}$. Interestingly Motte et al. (1998) find that the Mass Function for the prestellar clumps

[3] This picture is confused by the possible mixing of populations of different ages.

on the same region has a value of $\alpha \approx 0.5$ below $0.5M_{\odot}$. These values appear to differ drastically. However the Mass Functions in both cases have a completeness limit of approximately $0.1M_{\odot}$. Below this Luhman & Rieke (1999) use an estimate of their survey's incompleteness and fit their power-law MF in this region as well as the region above the completeness limit. Conversely Motte et al. (1998) only fit a power-law in the fully complete region of the MF. When the plots of both MFs are examined (see Luhman & Rieke (1999)'s Figure 13) it is clear that both take a very similar form. This indicates that the Mass Function of the star forming clumps is the same as that for stars.

Studies of the IMF in Open Clusters and SFR require accurate evolutionary models. The accuracy of the current generation of models has been called into question by Close et al. (2005)'s discovery of AB Doradus C, a young low mass object in a close binary system. They use the binary orbit to measure the mass of this object as $0.090\pm0.005M_{\odot}$. Using this mass, an age of 50Myr from studies of the primary, absolute magnitudes and an effective temperature measurement, they find a predicted mass from evolutionary models. This is significantly less than the measured mass. However recently Luhman et al. (2005) have claimed that AB Dor (and the moving group it is part of) are in fact a member of a larger moving group including the Pleiades. This increases the age to approximately 100Myr and the discrepancy with the mass measured from the absolute magnitudes disappears. However Nielsen et al. (2005) dispute this conclusion, claiming both that the AB Dor group is significantly brighter (and hence younger than the Pleiades) and that even using Luhman et al. (2005)'s age there is still a large error in the effective temperature.

2.1.3 Observational Studies of the Extragalactic IMF

If the form of the Mass Function is determined by some underlying physical process then it should be universal. Hence extragalactic studies of the Mass Function should produce similar results to Galactic ones. Unfortunately it is not possible to study the low mass IMF in other galaxies so a comparison of the high mass IMF must be used. Such studies include those of Veltchev et al. (2004) and Förster Schreiber et al. (2003). In the former, studies of individual stars in OB associations in M31 find an index

for the Mass Function of $\alpha = 1.59 \pm 0.09$. This is reasonably similar to the Salpeter value. The latter study looks at the bulk properties of starburst regions within M82. They state that a Saltpeter IMF flattening at lower masses is consistent with their observations and analysis. In the LMC, Massey & Hunter (1998) study of the cluster of O stars R136 finds an IMF with values of α of 1.3 ± 0.1 or 1.4 ± 0.1 depending on the temperature scale used close to both Salpeter value and that of Massey et al. (1995) for OB associations in the Milky Way.

2.2 Mass Function Theory

It has been shown in the previous section that the Mass Function takes the same form in many different studies. This implies that the shape of the IMF is not random but derives from the physical processes of star formation. The Initial Mass Function produced by star formation theories must match the observed Mass Function from the studies mentioned in Section 2.1, namely a Salpeter slope at high-intermediate masses and a flattening and possible decline at low masses. This section deals with some of the most prominent current theories of star formation and demonstrates how they bridge the gap from the counting of stars to interesting underlying physics.

The two main theories outlined here both utilise the turbulent nature of Molecular Clouds (Larson (1979)) as the trigger for star formation. In the case of superalfvenic turbulent fragmentation (Padoan & Nordlund, 2002) the turbulence provides the mechanism for the fragmentation and defines the shape of the high mass IMF. In the case of competitive accretion (Bate & Bonnell, 2005) the turbulence drives the cloud to fragment but the final masses of the stars produced depend less on the cores they are formed in and more on the amount of matter they can accrete.

2.2.1 SuperAlfvenic Turbulent Fragmentation

Turbulence can be imagined as a series of eddies of a scale L with energy injected at a large scale (say by the galactic wind) and cascading down to the smallest scale eddies where the energy is dissipated. It can be shown that the velocity v_L at a certain scale L obeys the following relation.

$$v_L \propto L^a \tag{2.9}$$

This has been observed in molecular clouds by Larson (1981) [4] and is known as the Larson Relation. Observational studies have pinned the value of a down to 0.4. The Energy Power spectrum of the turbulence at a particular wavenumber k is,

$$E(k) \propto k^{-\beta} \tag{2.10}$$

where

$$a = \frac{\beta - 1}{2} \tag{2.11}$$

Shocked Gas

Assuming the magnetic pressure is greater than thermal pressure, a gas cloud will be affected by shocks relative to the alfven velocity v_A. Consider a sheet of thickness L, density ρ_1 and magnetic field B_1 before being shocked and thickness λ, density ρ_2 and magnetic field B_2 after being shocked. The Alfven Mach Number is given by,

$$M_\mathrm{A} = \frac{v}{v_\mathrm{A}} = \frac{\rho_2}{\rho_1} = \frac{L}{\lambda} = \frac{B_2}{B_1} \tag{2.12}$$

Now consider a spherical cloud of post-shock gas that may become a prestellar core. Assume it has a radius the same as the thickness of the sheet. Hence its mass will be,

$$m \approx \rho_1 \lambda^3 = \frac{\rho_0 L^3}{M_\mathrm{A}^2} \tag{2.13}$$

As the Mach number is proportional to the velocity the Larson relation, Equation 2.9 can be used to show that,

$$M_\mathrm{A} \propto L^\alpha \tag{2.14}$$

Introducing $M_{\mathrm{A},0}$ as the Alfven Mach number on the largest scale L_0, it can be shown that,

$$m = \frac{\rho_0 L_0^3}{M_{\mathrm{A},0}^2} \left(\frac{L}{L_0} \right)^{4-\beta} \tag{2.15}$$

[4] Larson used α for his exponent, a is used here to avoid confusion with the exponent of a power law Mass function.

Now consider two experiments of scales L_1 and L_2 ($L_2 > L_1$) with the same densities and Mach numbers [5]. The second experiment will have more mass by a factor of $(L_2/L_1)^3$, but the cores it forms will be more massive by a factor of $(L_2/L_1)^3$. Hence the same number of cores will be formed. As the total number of cores formed is scale independent the number density follows the relation $n \propto L^{-3}$. Hence,

$$n(m)d\log_{10} m \propto L^{-3}d\log_{10} m \propto m^{-3/(4-\beta)}d\log_{10} m \tag{2.16}$$

The exponent of the number of cores is the same as the exponent for a power law Mass Function. Inserting $a = 0.4$ ($\beta = 1.8$) gives a value of $\alpha = 1.36$; almost exactly a Salpeter slope.

Collapsing Cores

Now consider the probability these cores will collapse to form stars. In order to do this the probability density function of the number density must be considered. This has been found to be gaussian by numerical simulations (Padoan et al. (1997)),

$$p(\ln n')d\ln n' = \frac{1}{\sqrt{2\pi\sigma^2}}exp\left[-\frac{1}{2}\left(\frac{\ln n' - <\ln n'>}{\sigma}\right)^2\right]d\ln n' \tag{2.17}$$

where n' is the number density divided by the mean number density. $p(n')d\ln n'$ can be thought of as the density distribution per unit volume. To consider the density distribution per unit mass $p(n')d\ln n'$ must multiply by a factor of n'. Hence the probability distribution of Jeans masses is,

$$q(m'_{\rm J})dm'_{\rm J} = n'p(\ln n')\frac{d\ln n'}{dn'}\frac{dn'}{dm'_{\rm J}}dm'_{\rm J} \tag{2.18}$$

where $m'_{\rm J}$ is the Jeans mass divided by the Jeans mass at mean density. As,

$$m'_{\rm J} = n'^{-1/2} \tag{2.19}$$

it can be shown that,

$$q(m'_{\rm J})dm'_{\rm J} = \frac{2}{\sqrt{2\pi\sigma^2}}m'^{-3}_{\rm J}exp\left[-\frac{1}{2}\left(\frac{2\ln m'_{\rm J} + <\ln n'>}{\sigma}\right)^2\right]dm'_{\rm J} \tag{2.20}$$

Hence the Jeans mass varies through the cloud so the concept of a local Jeans mass must be considered rather than the global Jeans mass of the cloud. In order for a core

[5] This is an obvious shortcoming of this theory as the Mach number is scale dependent

to collapse it must have a mass greater than the local Jeans mass. The probability of this is the integral of the probability distribution for the Jeans mass,

$$\int_0^{m/m_{\mathrm{J},0}} q(m'_{\mathrm{J}})dm'_{\mathrm{J}} \tag{2.21}$$

This factor can be inserted into the mass function to yield,

$$n(m)d\log_{10} m \propto m^{-3/(4-\beta)} \left[\int_0^{m/m_{\mathrm{J},0}} q(m'_{\mathrm{J}})dm'_{\mathrm{J}}\right] d\log_{10} m \tag{2.22}$$

This introduction of the probability of collapse gives us the flattening off in the Mass Function we require to match observations. The high mass IMF is shown to be independent of the cloud conditions while the flattening off depends on the Jeans mass and hence the temperature and mean density of the cloud.

Hence this model produces an almost exact Salpeter slope at high masses (due to the spectrum of cores from fragmentation) and a flattening at low masses (due to the distribution of probabilities that those cores will collapse).

There are two main problems with this theory. The first is that in finding that $N \propto L^{-3}$, it is assumed that the two different scales have the same Mach number. This is incorrect as the Mach number is scale dependent (see Equation 2.14). Also there is no treatment of magnetic pressure in the collapsing cores. While one is presented in Padoan & Nordlund (2002) it is very sketchy. Finally this assumes that each core produces either one star or no stars. If it were to be found that cores produce multiple stars this would call this theory into question.

2.2.2 Competitive Accretion

In the competitive accretion theory objects form with an initial low mass (normally the opacity limited mass) of a few Jupiter masses. These objects then accrete gas until there is either no gas left or the objects are ejected from the gas cloud by dynamical interactions. Bate & Bonnell (2005) (and references therein) have used Smoothed Particle Hydrodynamics simulations to test the Mass Functions produced by such a process. The simulations are set up with a turbulent molecular cloud. The simulation is set running and soon (within a few tenths of a freefall time) the cloud begins to fragment. Objects form first in the densest regions, these then have the chance to

accrete more gas and hence gain more mass. The formation of objects is modelled by creating sink particles when a region exceeds a certain density. Crucially in this theory several stars are formed from each core. The clusters formed by each core then dissolve by dynamical interactions with many of the low mass objects being ejected from the system entirely preventing them from accreting any more gas.

The simulations produce an IMF which broadly matches observational studies (ie Kroupa (2001) and Chabrier (2001)). The median mass of the objects produced is found to be lower (and hence more Brown Dwarfs were produced) in a simulation with a lower thermal Jeans mass.

An Analytical Model

Bate & Bonnell (2005) have developed an analytical treatment for the process of competitive accretion. It is a simple model where the accretion rate of an object is lognormal. Such that,

$$p(\dot{M}) = \frac{1}{\sqrt{2\pi}\sigma\dot{M}} \exp\left(\frac{-(log_{10}(\dot{M}) - log_{10}(\bar{\dot{M}}))^2}{2\sigma^2}\right) \tag{2.23}$$

The probability distribution of masses $f(M)$ is thus,

$$f(m) = p(\dot{M})\frac{d\dot{M}}{dM} \tag{2.24}$$

Using a simple relation between an objects final mass and the accretion rate (assuming the object is created by fragmentation at some minimum mass M_{min}),

$$M = M_{\rm min} + \dot{M}t \tag{2.25}$$

This gives a relation between the probability of each mass at a particular time ($f(M,t)$) and a series of parameters ($\bar{\dot{M}}$, $M_{\rm min}$ and σ) which characterise the accretion and fragmentation processes. In addition to the accretion rate the time during which an object accretes must be taken into account. As mentioned earlier the accretion process is terminated by dynamical ejections. This is modelled as the probability of ejection $e(t)$ such that,

$$e(t) = \frac{1}{\tau_{\rm eject}} \exp\left(\frac{-t}{\tau_{\rm eject}}\right) \tag{2.26}$$

Hence the final mass distribution is,

$$f(M) = \int_0^\infty f(M,t)e(t)dt \tag{2.27}$$

The approximate values of the parameters are $\bar{\dot{M}} \approx 10^{-6}\mathrm{M}_\odot/yr$, $\sigma \approx 0.5$ and $\tau_{\mathrm{eject}} \approx 10^4$. Parameter values such as these produce an IMF with an approximately Salpeter slope at high masses and flattening and falling below the Hydrogen Burning limit ($\approx 0.7\mathrm{M}_\odot$ Burrows et al. 1997). The theory presented by Bate & Bonnell (2005) does produce a Mass Function similar to that observed. However as they admit themselves this theory does not take into account the effects of stellar winds or jets which would reduce the efficiency of the star forming process. Recently Krumholz et al. (2005) have calculated the efficiency of competitive accretion as a star forming process. They find that while it could be significant in some circumstances no star forming region matches these circumstances. They also claim that the simulations produce significant results because the clouds used are of a much lower mass than a typical Galactic cloud. Bonnell & Bate (2006) counter this claim, pointing out that Krumholz et al. (2005) uses properties globally averaged for the clouds, not for the denser regions inside the clouds where stars form. This, they say, is why Krumholz et al. (2005)'s estimate of the accretion rate is so low.

2.2.3 The Central Limit Theorem

The final model of Star Formation described in this subsection is that outlined by Adams & Fatuzzo (1996). They produce a model in which a near infinite series of parameters from many underlying processes produces (via the central limit theorem) a near lognormal Mass Function. However this model is based on spherical infall onto a protostar being shut off by stellar winds and bipolar jets. It is difficult to see (as noted by Chabrier (2003a)) how objects below the Hydrogen Burning limit could stop this accretion in the absence of such winds. Hence if this were correct there would be a discontinuity in the IMF around the Hydrogen Burning limit.

2.3 The Stellar Birthrate

The simplest model for a birthrate is that assumed by Salpeter (1955), a constant. Here all ages from the start of formation of the Galactic disk to the present day are equally probable. More complex models of star formation within the Galaxy produce more complicated forms of the birthrate.

Schmidt (1959) utilises a simple model in which the number of stars formed in a particular area is proportional to the mass of gas available to form stars (in that area) raised to some power n. Put simply if stellar feedback is ignored this can be expressed as,

$$n_{\rm tot} b(t) \propto \left[m_{\rm g}(0) - \int m\xi(m) dm \int_0^t b(t) dt \right]^n \tag{2.28}$$

where $m_g(0)$ is the initial gas mass. It is possible to produce a constant birthrate by introducing an additional term on the right hand side of Equation 2.28 representing gas infall to the disk. If this were to balance the mass of the gas lost to star formation then a constant birthrate would be a solution. Additionally if $n = 0$ then the star formation rate would be constant (i.e. the birthrate and gas density were unrelated). If the power law index n is equal to one then $b(t)$ is proportional to its own integral. Hence an exponential solution would be possible such that,

$$b(t) \propto e^{-t/\tau} \tag{2.29}$$

Here the stellar birthrate declines exponentially as more gas is used up in star formation (a negative value of τ would give an increasing birthrate). If n is greater than one then the general form of the solution would be,

$$b(t) \propto \left[1 + (n-1)\frac{t}{\tau} \right]^{-n/(n-1)} \tag{2.30}$$

Again, star formation slows down as less gas becomes available. Both the forms found in Equations 2.29 and 2.30 are derived in Schmidt (1959).

Larson (1976) uses a similar principle to Schmidt (1959) with the rate of change of stellar mass density being proportional to the density of gas to some power n. However here he expands the technique to include a simple model of Galactic disk formation. This produces a birthrate which he considers typical for a disk galaxy. This rises sharply

as matter falls inwards and reaches a peak. It then decays as more mass is locked into stars.

One addition to these smooth forms of the birthrate is possible. Instead of the Galactic disk forming smoothly on its own it could undergo interactions with satellite galaxies and may even accrete them. Such processes would lead to bursts of star formation due both to shocks and to new gas entering the disk. This would produce a sharply varying birthrate.

2.3.1 Observational studies of the stellar birthrate

In his early paper which outlines the form of birthrate if it is dependent on the density of interstellar gas, Schmidt (1959) also seeks to constrain the power law index n (see Equation 2.28). He uses both the luminosity function of stars and the evolution of the abundance of helium to deduce that the value of n is approximately two. However, as noted by Miller & Scalo (1979), because his work came before the widespread acceptance of a hot Big Bang (and hence primordial nucleosynthesis) he uses an initial helium abundance of zero. Clearly this is not correct. Miller & Scalo (1979) go on to use a continuity constraint, that the mass function should be smooth to derive the birthrate. They reject Schmidt (1959)'s declining form instead preferring a roughly constant birthrate.

Twarog (1980) uses the metalicity distribution of F dwarfs to claim that the birthrate takes a similar form to that suggested by Larson (1976) where the birthrate is high just after the formation of the disk 10Gyrs or so ago and has declined since then. Conversely the observations and modelling of Boissier & Prantzos (1999) suggest that the disk formed slowly and that there was no early burst of star formation.

Rocha-Pinto et al. (2000) use the chromospheric activity of stars to derive their ages. From this age distribution they yield a birthrate that shows a series of three or four bursts of star formation in the last 10Gyrs. They note some of the bursts may be linked to close encounters with the Large Magellenic Cloud.

Chapter 3

Properties of Low Mass Stars and Brown Dwarfs

3.1 The M, L and T spectral types

The spectral type M was the coolest of Cannon's original spectral types. The spectra of these stars are dominated by metal oxides such as TiO and VO. The current classification system which was developed by Boesharr (1976) and extended to later types by Kirkpatrick et al. (1991) uses the appearance of different TiO bands to determine the spectral types of early M dwarfs. Dwarfs later than M5 have their spectral type defined by the ratio of the strengths VO 5736Å band to the TiO 5759Å band. A CaOH feature at $5530 - 60$Å begins to appear at M3.5 and clearly increases with later spectral type.

The L and T spectral classes define objects cooler than M9.5. L dwarfs cover a temperature range from $T_{\rm eff} \approx 2200 - 2000K$ to $T_{\rm eff} \approx 1300 - 1500K$. The spectral class was defined by Kirkpatrick et al. (1999), which contains spectral diagnostics and sample spectra for each spectral subtype from L0V to L8V. While the hotter M dwarfs have spectra dominated by bands from metal oxides (TiO and VO) these decline with increasing L subtype and have virtually disappeared by L2 and L4 respectively. By contrast the strengths of certain metals (Rb, Cs and K) increase along with features from metal hydrides (CrH and FeH). L dwarfs are red in both the optical (I-J) and infrared (J-K).

The T dwarf spectral type was defined by Burgasser et al. (2002) and Geballe et al.

(2002) for the near infrared and Burgasser et al. (2003) for the red optical region with subindices ranging from T1V to T8V. The T dwarf spectra contains (like the L dwarf spectra) metals (Rb, K and Cs) and metal hydrides (FeH, CaH and CrH). There are also increasing spectra features from methane, hence the alternative name methane dwarf. The infrared spectrum also contains features from water. While, like L dwarfs, T dwarfs are red in the optical (I-J) they are, by contrast, blue in the near infrared (J-K).

3.2 Internal Physics

3.2.1 Nuclear Reactions

Brown Dwarfs are objects which in plain speak lack sufficient mass to commence hydrogen burning (in Low Mass Stars this is dominated by the p-p chain). In order for hydrogen burning to begin a star must have a core temperature greater than $T_c = 3 \times 10^6 K$. This appears to be a clean line dividing stars which have sufficient mass to attain such a temperature and those which do not. The real picture is somewhat less clear as some transitional objects with masses in the range $0.07\mathrm{M}_\odot < m < 0.08\mathrm{M}_\odot$ can begin Hydrogen burning but cease to do so due to the effects of core degeneracy. The composition of a low mass object will also affect the internal temperature and hence the mass at which stable Hydrogen burning will be possible. The lower limit at which divides Brown Dwarfs from planets is also set by a nuclear reaction. Primordial Deuterium is converted in to ^3He in the process shown in Equation 3.1 at a temperature of 6×10^5K

.

$$d + p \rightarrow^3 He + \gamma \tag{3.1}$$

This temperature is only reached by objects with masses greater than $0.012\mathrm{M}_\odot$ (Grossman, 1970) and hence this has been adopted by the IAU as the lower mass limit for a Brown Dwarf. However it appears that Deuterium burning plays no significant role in star formation Chabrier (2003a), hence this division is purely schematic.

The Lithium Test

A useful spectroscopic test for potential substellar objects was proposed by Pozio (1991). Above a temperature of 2.4×10^6 K primordial Lithium is burned by the reaction,

$$^7Li + p \rightarrow ^4He + ^4He \tag{3.2}$$

Due to this, objects with masses lower than $M = 0.06M_\odot$ Magazzu et al. (1993) which never reach this temperature will retain Lithium at primordial abundance. Objects which have slightly higher masses will have some Lithium depletion as they will only reach the required temperature (and hence burn Lithium) for a short period in their evolution. As Low Mass Stars and Brown Dwarfs are fully convective (see Section 3.2.2) Lithium from the envelope will be transported into the core where it will be burned. This will result in a depletion of Lithium at the surface and hence an absence of Lithium spectral features. The Lithium depletion boundary is set at the point where 90% of primordial Lithium has been destroyed. This includes all stars with masses below $M = 0.1M_\odot$ at an age of 0.1Myr but as stars with sufficient temperatures gradually burn their Lithium it drops to include only stars which have either not reached the Lithium burning temperature or those which only reached this temperature for a time too short to burn enough Lithium. This means that the 6708Å Li I line provides an excellent diagnostic as to the nature of a candidate Low Mass Star or Brown Dwarf.

3.2.2 Convection

As mentioned already Low Mass Stars and Brown Dwarfs are fully convective. This means that there is a convective envelope stretching from the core to the surface, resulting in the object becoming well mixed. In order for an object to become convective it must first meet the condition for convective instability known as the Schwarzchild criterion.

Consider a parcel of gas in a Low Mass Star or Brown Dwarf which is displaced upwards. As the pressure of the gas parcel will be higher than its surroundings it will expand and cool adiabatically. If the change in temperature is small enough that the parcel is still hotter (and hence less dense) than its surroundings it will continue to

rise. This can be summed up by,

$$\left(\frac{dT}{dz}\right)_{ad} < \left(\frac{dT}{dz}\right)_{\text{sur}} \tag{3.3}$$

ie that the adiabatic change in temperature with respect to height is less than that of the surroundings. Now assuming that the pressure gradient is the same for both cases,

$$\left(\frac{dP}{dz}\right)_{ad} = \left(\frac{dP}{dz}\right)_{\text{sur}} \tag{3.4}$$

Hence,

$$\left(\frac{dT}{dP}\right)_{ad} < \left(\frac{dT}{dP}\right)_{\text{sur}} \tag{3.5}$$

If the surroundings are in radiative equilibrium we get,

$$\nabla_{\text{ad}} < \nabla_{\text{rad}} \tag{3.6}$$

So the Schwarzchild Criterion for Convection is that the adiabatic gradient must be less than the radiative gradient.

The Adiabatic gradient is related to the polytropic index of the equation of state for the gas and hence to the state (molecular, partial ionized, fully ionized etc.) . The Radiative gradient is related to the Opacity, Luminosity, Pressure and temperature of the surroundings by,

$$\nabla_{rad} \propto \frac{L\kappa P}{T^4} \tag{3.7}$$

The bottom of the convective zone (ie the point where the adiabatic and radiative gradients are equal) varies changes with the mass of the star. This is obvious as the Luminosity, Pressure and temperature depend on the mass. Chabrier & Baraffe (1997) have shown that for Low Mass Stars the radiative zone disappears and the convective zone fills the whole envelope. The mass at which this happens is clearly metalicity dependant as Opacity varies with metalicity. For solar metalicity the full convection limit is $0.35M_{\odot}$.

3.2.3 Core Degeneracy

Low Mass Stars and Brown Dwarfs produce much less energy (or none at all) from hydrogen burning than higher mass stars. Hence they cannot simply rely on gas and radiation pressure for support. Degenerate electron pressure plays a role.

Stevenson (1991) outlines a simple model for degeneracy in a Low Mass Star or Brown Dwarf. In it the pressure is assumed to be a summation of the degenerate Fermi pressure ($P_{\rm F}$), the thermal pressure due to nuclei ($P_{\rm th,ion}$) and the thermal pressure due to electrons ($P_{\rm th,el}$). If the polytropic index $n = 1.5$ and the degeneracy is assumed to be non-relativistic then,

$$\begin{aligned} P_F &\propto \left(\frac{\rho}{\mu_e}\right)^{\frac{5}{3}} \\ P_{th,ion} &= \frac{\mu_e \psi}{\overline{A}} P_F \\ P_{th,e} &= \frac{\mu_e^{\frac{2}{3}} \psi^2}{1+\psi} P_F \end{aligned} \tag{3.8}$$

where μ_e is the mean molecular weight, $\overline{A}$ is the mean atomic mass and ψ is the degeneracy parameter such that,

$$\psi \propto T \left(\frac{\mu_e}{\rho}\right)^{\frac{2}{3}} \tag{3.9}$$

The higher the degeneracy, the lower the value of ψ. Stevenson (1991) derives the expression below for for the central temperature,

$$T_{\rm c} = 5 \times 10^8 K \left(\frac{M}{M_\odot}\right)^{\frac{4}{3}} \mu_e^{\frac{-2}{3}} \frac{\psi}{1 + \psi + \frac{\psi^2}{1+\psi}} \tag{3.10}$$

The maximum temperature can be found by differentiating T_c and setting the gradient to zero. This yields the following polynomial,

$$1 + \psi - 4\psi^2 - 2\psi^3 = 0 \tag{3.11}$$

There is a solution for this at $\psi = 0.55$, inserting $\mu_{\rm e} = 1.15$ gives a maximum cental temperature of,

$$T_{\rm cmax} = 8.1 \times 10^7 \left(\frac{M}{M_\odot}\right)^{\frac{4}{3}} \tag{3.12}$$

So the mass required to support core Hydrogen burning ($T_{\rm c} > 3 \times 10^6$ K) is $0.084{\rm M}_\odot$, not too far off the correct figure of $0.08{\rm M}_\odot$.

3.3 The Atmospheres of Low Mass Stars and Brown Dwarfs

The atmosphere of a Low Mass Star or Brown Dwarf plays an important role in it's observational properties. In the M and L spectral classes dust is suspended in the

photosphere (Chabrier et al., 2000) this leads to red optical and infrared colours. In the T spectral class the dust sinks below the photosphere. This reduces the reddening by the dust and also removes some Oxygen from the photosphere (Lodders & Fegley, 2002) aiding the takeover of methane as the dominant form of Carbon over CO. Hence effective modelling of dust clouds is required.

Studies of dust clouds adopt the following formalism. The number of moles of a substance per mole of atmosphere is known as the mixing ratio. The mixing ratios for vapour and condensate are $q_{\rm v}$ and $q_{\rm c}$ respectively with the total mixing ratio being $q_{\rm t} = q_{\rm v} + q_{\rm c}$. In the clouds $q_{\rm v} = q_{\rm s}$ (the saturation mixing ration for that particular altitude), any vapour greater than $q_{\rm v}$ will quickly condense and increase $q_{\rm c}$. The model presented by Lewis (1969) states that only vapour can move upwards, ie,

$$q_{\rm t}(z) = q_{\rm v}(z - \Delta z) \tag{3.13}$$

Higher up in the atmosphere the saturation mixing ratio will be lower so some of this vapour will condense. The next level up will then have the same total mixing ratio as the vapour mixing ratio for this level. This process leads to a gradual reduction in the total mixing ratio with height. This will work for purely radiative atmosphere but does not take turbulence into account.

A solution to this problem is produced in Ackerman & Marley (2001). Here the atmosphere is well mixed by turbulence so with no sedimentation the total mixing ratio will be constant at each level in the atmosphere. However if sedimentation is introduced, the raining out of sediment will reduce $q_{\rm c}$ and hence $q_{\rm t}$. This is summed up in equation form by,

$$-K\frac{dq_{\rm t}}{dz} - f_{\rm rain} w_* q_{\rm c} = 0 \tag{3.14}$$

where K is the eddy diffusion constant, w_* is convective velocity scale and $f_{\rm rain}$ is the ratio of sedimentation velocity to w_*. Clearly when $f_{\rm rain} = 0$ we have a case where dust is suspended in the photosphere, and when we have high values of $f_{\rm rain}$, $q_{\rm t}$ reduces rapidly with height and hence the upper atmosphere will be largely dust-free. However this does not explain why some objects (M and L dwarfs) appear to have low values of $f_{\rm rain}$ while others (T dwarfs) appear to have high values of $f_{\rm rain}$. One potential solution to this is provided by considering the physics of dust formation.

The uniform cloud model produced by Tsuji (2005) (and references therein) provides a solution. Here the Gibbs free energy is found as a function of n, the number of atoms in the grain. The Gibbs free energy has some maximum value at $n = n_*$. As Gibbs free energy cannot increase for any chemical process, any dust grain larger than n_* can increase in size, while any dust grain smaller than n_* cannot. In this model dust is constantly being created and destroyed, however if a dust grain is larger than n_* it will increase in size and will eventually rain out by sedimentation once it grows greater than some critical radius $r_{\rm cr}$. It is found that,

$$n_* \propto T^{-3} \tag{3.15}$$

Hence $r_{\rm cr}$ will be reached at some critical temperature $T_{\rm cr}$. Dust forms only when the temperature is less than a condensation temperature $T_{\rm cond}$ and it will undergo a runaway increase in its size and rain out once it is cooler than $T_{\rm cr}$. So dust can only exist in the range $T_{\rm cr} < T < T_{\rm cond}$. Hence for hotter objects the photosphere will be hotter than $T_{\rm cr}$ so dust will be suspended. However the photospheres of cooler objects will be cooler than $T_{\rm crit}$ and so will not contain any dust. The cloud top too will lie deeper in the atmosphere where $T = T_{\rm crit}$

In the model presented by Burgasser et al. (2002), the transition from L type to T type is not caused by dust being removed uniformly from the atmosphere. Here the dust clouds gradually break up revealing warmer, dust-free regions below. They show that a simple interpolation between a model with dust clouds and one with no dust clouds reveals that changing the cloud coverage in such a way can successfully describe the L/T transition.

3.4 Models of Low Mass Stars and Brown Dwarfs

The modelling of Brown Dwarfs and Low Mass Stars can be split into two parts: that of internal physics and that of the atmosphere. The internal physics is fairly well understood. Saumon et al. (1995)'s equation of state is combined with the work of Kumar (1963) and Stevenson (1991) as the input physics for the models of Chabrier & Baraffe (1997) and Burrows et al. (1997).

In contrast the atmospheric physics used differs greatly between model sets. The

perfect example of this are the two model sets produced by the Lyon group. The first (DUSTY, see Chabrier et al. 2000) has dust suspended in the photosphere (ie. a low value of f_{rain}). This models the redder M and L regime well but breaks down at the L/T boundary where the infrared colours continue to redden instead of making the blueward turn due to methane absorption. Similarly the COND models (Baraffe et al., 2003) where dust has settled below the photosphere (ie a high value of $f_{\rm rain}$) fit the T regime very well but are less accurate in the M and L regimes.

Hence while the internal physics of low mass stars and brown dwarfs are well understood, the nature of the atmospheric physics (especially those contributing to the transition between the L and T spectral types) remains a challenge for those trying to model such objects.

Chapter 4

The Southern Infrared Proper Motion Survey

There are two principal methods for discovering low mass stars and brown dwarfs in the field: proper motion surveys and infrared surveys. Cool dwarfs are intrinsically faint and hence only those close by will be detectable. Proper motion surveys are biased towards objects with high intrinsic space velocities and to those nearby. Therefore a proper motion survey will filter out more distant background stars which are not moving. Until now proper motion surveys have only been done in the optical region. Infrared surveys on the other hand examine the portion of the spectrum where cool dwarfs are brightest. Hence they are a useful tool for discovering such objects. However purely photometric surveys of this type suffer from contamination due to distant red giant stars which have similar colours to cool dwarfs.

The Southern Infrared Proper Motion Survey (SIPS) combines both of these techniques to produce a proper motion selected sample in the infrared. The two epochs used are SuperCOSMOS scans of UKST I_N [1] plates (Hambly et al., 2001b) and J, H and K_s data from the Two Micron All Sky Survey (2MASS; Skrutskie et al. 2006).

[1] All the I magnitudes referred to from UKST data are I_N. In some circumstances when comparing to other studies or models I_C may be used. Bessell (1986) shows that these two filters can be compared directly with little error.

4.1 High Proper Motion Searches

Early proper motion surveys relied on blink comparators and photographic plates of relatively small fields. It was not until the advent of the Schmidt Telescope that truly widefield proper motion surveys became possible. Luyten's Half Arcsecond Catalogue (hereafter LHS) (Luyten, 1979) ties up this earlier work done at the Meridian Observatory, Union Observatory and Luyten's own work on the Bruce Proper Motion Catalogue. It also contains a wealth of new discoveries made by Luyten himself using Palomar Schmidt plates. In total there are 3587 stars with $\mu \geq 0.5$"/yr. Luyten also lists 60,000 high proper motion stars in his New Luyten Two-Tenths catalogue (NLTT; Luyten 1980) which have proper motions greater than 0.2"/yr. Both surveys are incomplete at declinations south of $-33°$ and exclude fields in the galactic plane. Modern high proper motion searches seek to complete Luyten's work in the southern sky and to identify objects Luyten missed. Some of these use manual blinking techniques such as the Calan-ESO proper motion catalogue (Ruiz et al., 2001) and the study of Wroblewski & Costa (2001). Recent computational methods include those of Pokorny et al. (2003) and Scholz et al. (2002). Pokorny lists 6206 stars with $\mu \geq 0.18$"/yr found using SuperCOSMOS scans of 131 Schmidt fields. Scholz found 15 stars with high proper motions from APM scans of UKST plates. Eight of these have distances less than 25 pc. Lepine & Shara (2002) have used POSS plates to search in the northern hemisphere. This has been done with the SUPERBLINK algorithm, in which plates from two different epochs (POSS I and POSS II) are aligned and the later, better POSS II plates degraded to make them of comparable quality to the POSS I plates. The two images are then subtracted making the moving, high proper motion objects obvious.

4.1.1 Common Proper Motion Searches

Modern star formation models indicate that many known stellar systems may have unknown wide, low mass companions. As these are gravitationally bound to their systems they will move through space with the same space velocity and hence have a common proper motion. One such object is the nearest star to the Sun, Proxima Centauri which is a wide companion to α Centauri. It was first identified as a nearby star by Innes et al. (1915) because of its common proper motion with α Cent. Recent discoveries

using such methods are those of ϵ Indi B a/b (Scholz et al. 2003 and McCaughrean et al. 2004) and an active M8.5 dwarf companion to the DA - M4 binary LHS 4039 / LHS 4040 (Scholz et al., 2004).

4.2 Infrared Surveys

The first major modern infrared surveys came with the Deep Near Infrared Survey (DENIS; Epchtein et al. 1994) and the Two Micron All Sky Survey (2MASS; Kleinmann et al. 1994). DENIS covers the southern sky in I, J and K_s down to limits of $I = 18.5$, $J = 16.5$ and $K_s = 14.0$ while 2MASS is an all sky survey in J, H and K_s down to limits of $J = 15.8$, $H = 15.1$ and $K_s = 14.3$. Both have been useful for discovering ultra–cool dwarfs with DENIS finding several late M and L dwarfs and 2MASS finding countless L dwarfs and a large sample of T dwarfs. In addition several tens of L and T dwarfs (Chiu et al., 2006) have been found using the primarily optical Sloan Digital Sky Survey (SDSS, Adelman-McCarthy & et al. 2006).

Many infrared surveys for low mass objects such as Cruz et al. (2003) and Burgasser et al. (2004b) utilise mostly photometric selections. They initially identify objects in the near infrared based on their colours in this region of the spectrum. These are then filtered on the basis of redness/absence in optical passbands. Objects which pass the selection criteria are then followed up spectroscopically. While the absence of an object in optical passbands may be due to a high proper motion and proper motion is sometimes referred to after the initial selection, no such infrared survey can be considered a true infrared proper motion survey.

4.3 The SIPS survey

The SIPS survey was carried out in two stages, the first focussed on high proper motion objects (μ¿0.5"/yr) and the second examining a lower proper motion sample (0.1"/yr¡μ¡0.5"/yr). The selection of candidates used a suite of C programs (utilising the Slalib library Wallace 2003) to mine the 2MASS and SuperCOSMOS data files. Candidate objects are intially selected on their 2MASS photometry and image parameters (see Section 4.3.1). I plate partners for these are then sought. If an object is found

to have an I plate counterpart within 1 arcsecond it is discounted as being stationary. The I plate partners for the moving candidates are then identified and if their I photometry suggests they are the same object and they pass a series of image quality tests they are passed to the eyeballing stage. Here each candidate is examined to ensure no spurious detections make the final sample. The candidate selection process is described in more detail below.

4.3.1 Initial Candidate Selection

Firstly candidate 2MASS images had to be selected. To ensure that these objects were not too close to the photometric limit of the 2MASS survey, the objects had to be brighter than $J = 16$. Elliptical objects may have inaccurate photometry and astrometry, hence selected objects had to have an axial ratio less than 1.4 (this figure was chosen after studying the ellipticities of objects in the 2MASS survey). Crowded regions near the galactic plane will produce many spurious detections of high proper motion objects. In order to reduce this crowding any object with $|b| < 15°$ was excluded. The 2MASS Point Source Catalogue includes a parameter indicating the proximity of the nearest source; the Executive Summary for the catalogue states that any object closer than 6" to its nearest neighbouring source must be treated with caution. Hence such objects were excluded. Objects categorised by the 2MASS survey as being associated with extended sources or minor planets were also removed.

Objects which met these criteria were then subjected to a series of colour cuts.

In order to make the process as efficient as possible, only objects whose photometry suggested that they were M, L and T dwarfs were selected. In order to do this, regions on a colour-colour diagram were marked out as likely to contain objects of a particular spectral type. Figure 4.1(a) shows these regions and Figure 4.1(b) shows the colours of objects taken from various surveys. The regions were chosen to approximately match the cooling track of a Brown Dwarfs taken from the Baraffe et al. (2003) models. Several objects lie outside these boxes due to photometric scatter. Note that because there is an overlap between the mid M and mid T spectral classes on a colour-colour diagram any object that falls in this region is treated as if it could be either spectral type. Several early M dwarfs fall outside the bounds of the M dwarf region. When the full

survey is produced this will have to be included in completeness estimates. Many T dwarfs fall outside the T dwarf region, this scatter is due to photometric errors. As an I plate limit has been set along with an $I - J$ cut only the brightest T dwarfs will be identified. Dimmer objects have higher photometric errors and hence higher scatter. As these objects are already excluded due to other photometric cuts it does not matter if they fall outside the T dwarf region on the colour colour diagram. Once objects have passed the colour cuts and been categorised it is then necessary to find if they are in fact moving with significant proper motions. Figure 4.2 shows the relative positional errors between SuperCOSMOS and 2MASS data. These were calculated by finding the positional shift of a set of 2MASS objects and calculating the mean error using a method of median absolute deviation. On the basis of these results it was decided to set one arcsecond (roughly 4-5 σ) as the lower "movement cut". This ensures that only objects which appear to have moved from one epoch to the other are included in the sample. Any 2MASS object found to have an I plate counterpart within one arcsecond was discounted as not having a significant enough proper motion. In the initial SIPS–I sample (objects with proper motions greater than 0.5"/yr) the positions used were simply those taken from the survey. However when the proper motion limit was pushed down to 0.1"/yr for the SIPS–II sample a relative astrometric mapping procedure was carried out to reduce the errors in the proper motions. This was done by Nigel Hambly using techniques outlined in Hambly et al. (2001a). This cut has implications for proper motion completeness which will have to be taken into account. Also to remove spurious detections due to bright stellar halos, any 2MASS object within 10" of an I plate image flagged as being close to a bright star was removed. Images blended on the I plates can cause positional offsets, hence any 2MASS object within 10" of a bright ($I < 14$) highly elliptical object or 6" of one deblended by SuperCOSMOS software was removed. This was done to remove objects which would have been removed earlier but were misclassified by the SuperCOSMOS survey. The 10" figure came from my experience of working with SuperCOSMOS data.

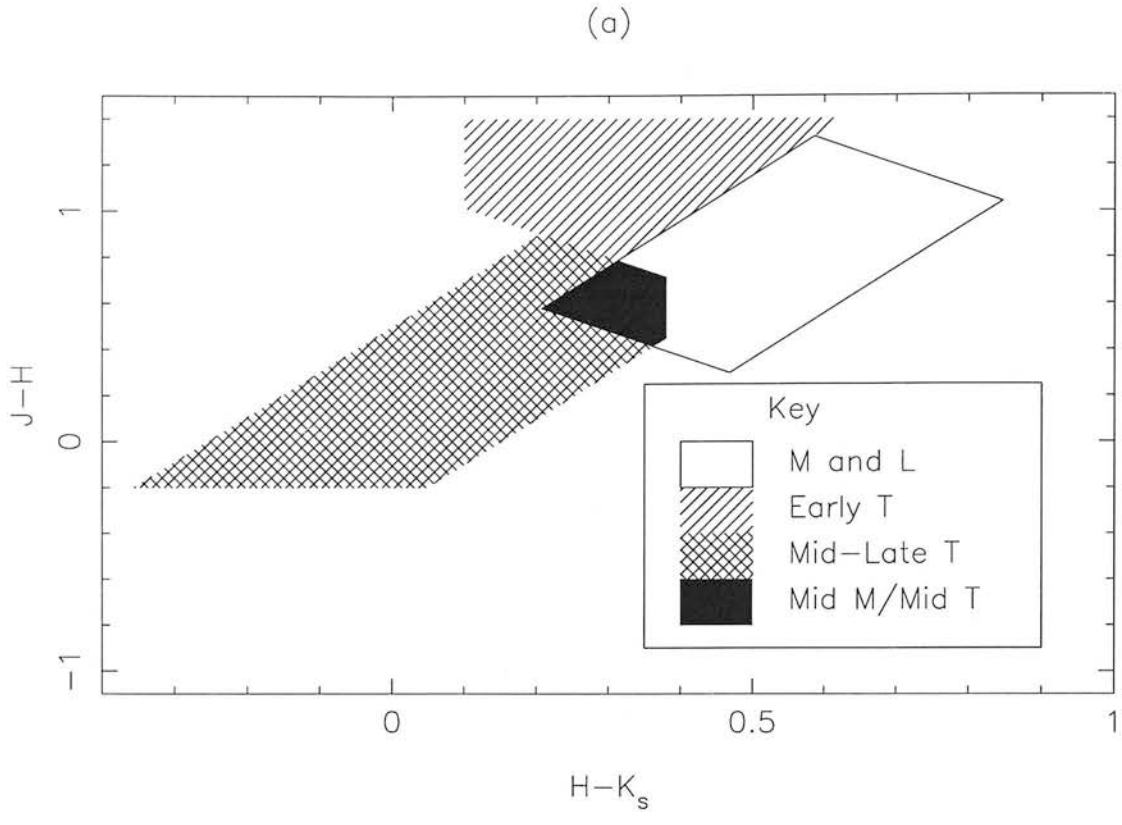

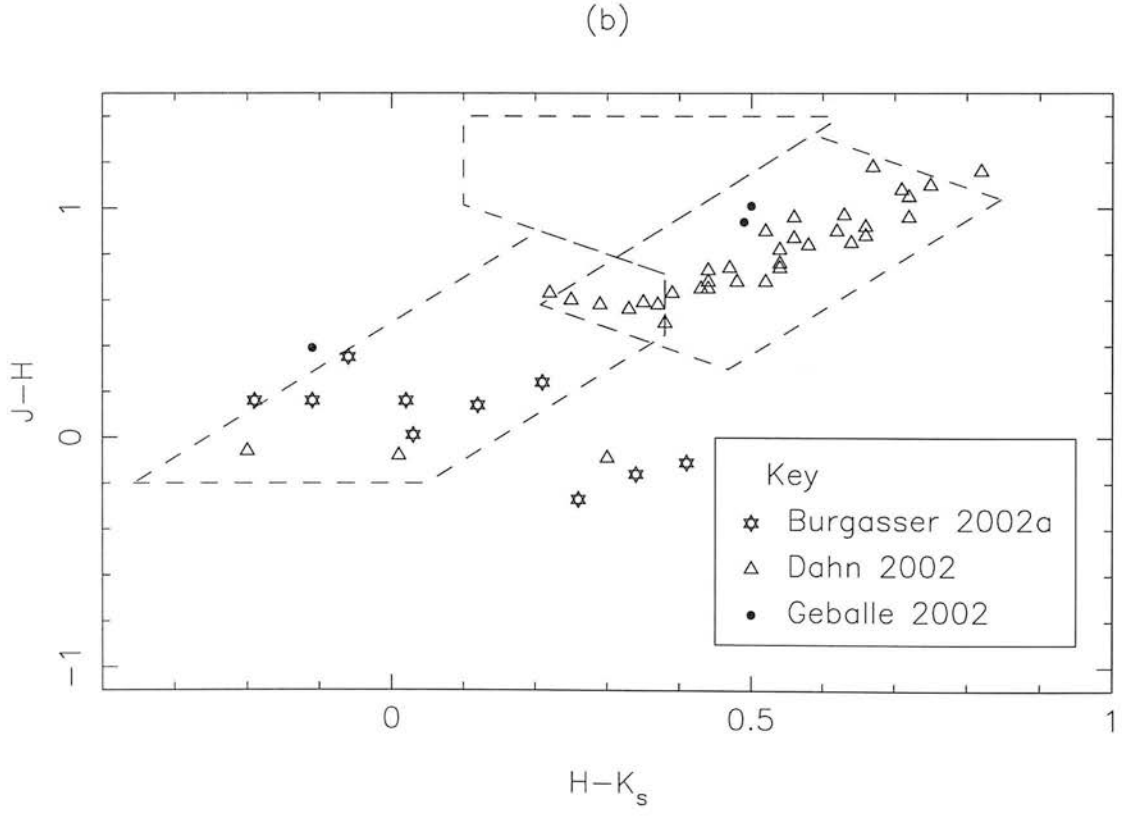

Figure 4.1: The regions in the colour-colour diagram within which objects were deemed to be M, L or T dwarfs.

4.3.2 Initial Astrometric Selection

Once it is established that objects have appeared to move their I plate counterparts need to be identified. In order to do this a maximum proper motion of $\mu_{\max} = 10"/\text{yr}$ was set meaning only I plate objects within a maximum radius $r_{\max} = \mu_{\max}\Delta t$ of the 2MASS object would be paired, where Δt is the time elapsed between the two observations. This maximum proper motion was chosen to be roughly equal to that of Barnard's star, the star with the highest known proper motion, this allows us to identify very high proper motion stars without being swamped by spurious pairings. Once an I plate object was identified as within $r_{\max}$ of the target it had to pass a series of tests to prove it was indeed a plausible counterpart to the 2MASS object.

Firstly the I plate object had to have astrometry suggesting it was a high proper motion star. These data come from the calculated astrometric solutions in the SuperCOSMOS sky survey (Hambly et al. 2001). Any I plate object with an astrometric solution that places it at the same position (within the proper motion errors quoted in the astrometric solution) as the 2MASS object at the epoch of the 2MASS observation will be included as a possible counterpart. Many objects will either be so red that they will only appear on the I plates. Also objects moving with high proper motions will have moved too far to be paired in other bands so will be recorded as only being on the I plates. Hence any object appearing only on the I plates (ie. not on the UKST B_J or R) was included as a possible counterpart. Finally some I plate objects will be incorrectly paired with unrelated objects on the UKST B_J or R [2] plates and hence will have an inaccurate astrometric solution. Such objects will have a high value of χ^2_ν (χ^2 per degree of freedom calculated by the survey software, N.C. et al. 2001), hence any object with $\chi^2_\nu > 2.0$ was included as a possible counterpart.

The I plate images also had to pass tests to indicate that they were good stellar images. Objects deblended by the SuperCOSMOS software were excluded as it is difficult to gather accurate astrometric information from them. Images with axial ratios higher than 1.7 were also excluded as they may have poor astrometry or may be blended objects which have not been separated by the software. I plate counterpart

[2]The UKST R is R_{59F}, where comparisons are required with data or models using the R_c transformations from Bessell (1986) are used.

objects also had to be stellar in nature and not be in close proximity to bright stars.

Candidates for I plate counterpart images also had to pass a series of photometric tests. Firstly to ensure that the I plate counterparts were red enough to be true Low Mass Stars or Brown Dwarfs any object which had a UKST R plate magnitude had to pass the cut $(R - I) > 2$. As noted in Section 2.1, 2MASS objects were classified as being, M and L dwarfs, early T dwarfs, mid-late T Dwarfs or as lying in the overlap region on the colour-colour diagram between M dwarfs and mid-T Dwarfs. Objects classified as M and L dwarfs had to fulfill the condition $1.0 < I - J < 4.8$. Objects classified as early T Dwarfs or mid-late T dwarfs had to be within the range $4.0 < I - J < 5.5$. Any object falling in the overlap region between M dwarfs and mid-T dwarfs could be of either type so had to conform to the conservative cut of $1.0 < I - J < 5.5$.

In order to ensure that the I plate objects selected were true counterparts and not unrelated objects two additional processes were carried out. Firstly it was checked using a computer routine that the I plate object was not associated with (within one arcsecond of) another 2MASS object. Secondly inspection by eye of the images ensured that only true high proper motion objects were selected.

4.3.3 Determination of Proper Motions

Objects in this survey are initially selected using proper motions calculated by finding the distance an object had moved between the two epochs and dividing by the time elapsed. Any object with such a calculated proper motion greater than 0.1"/yr was selected to have its proper motion more accurately calculated. The SuperCOSMOS Sky Survey (SSS) software calculates proper motions using B_J, I and two epoch R measurements for each object in the database. Hence, in theory, astrometric solutions for all the objects should be available. Unfortunately many do not have suitable solutions. Stars with very high proper motions will have large shifts in their positions from plate to plate meaning they will often be too far apart from one epoch to the next for the SSS software to identify them as the same object. Hence such stars will not have calculated proper motions. Some high proper motion objects may be spuriously paired with faint unrelated objects on one or more plates, producing an unreliable astromet-

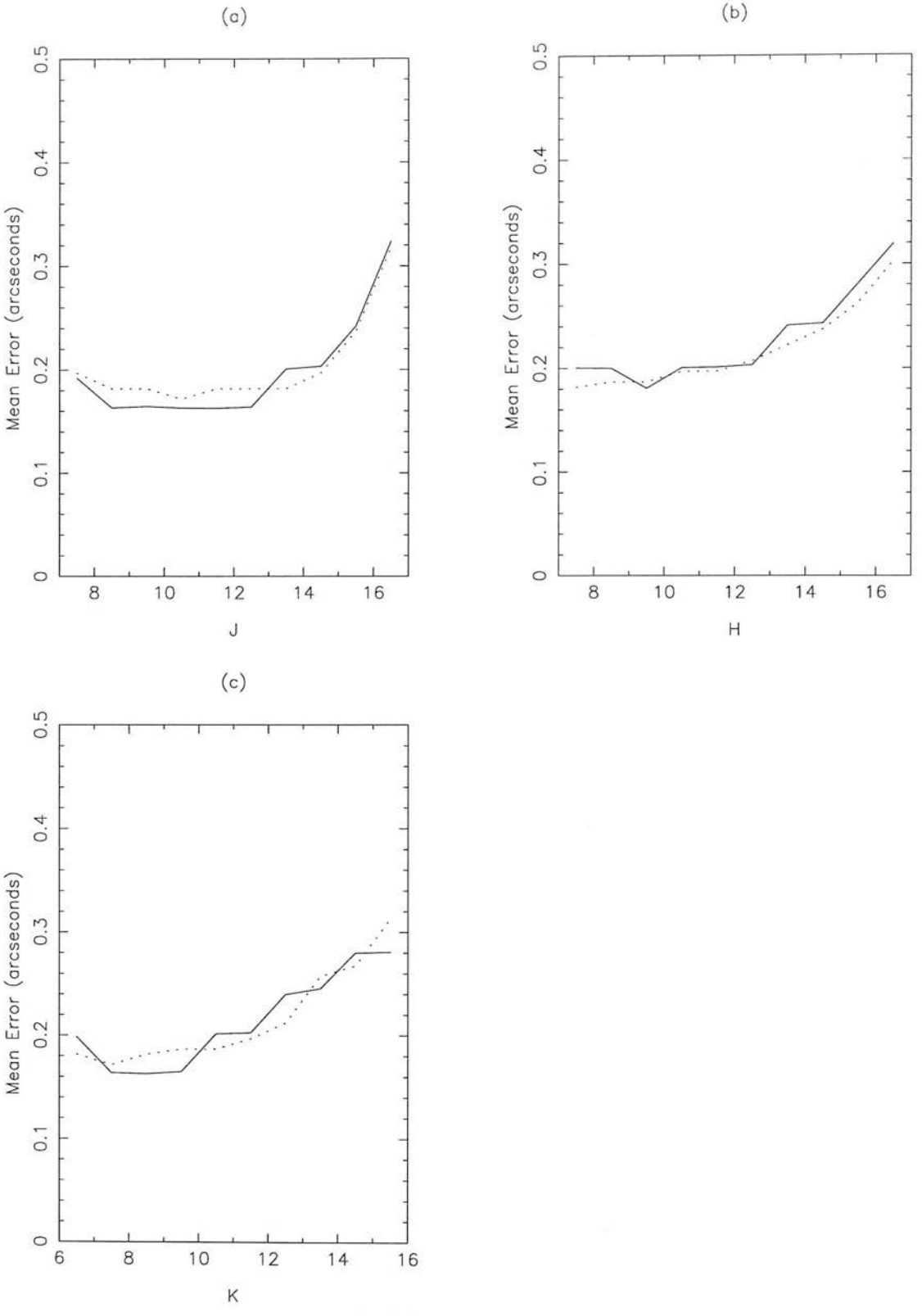

Figure 4.2: The relative positional errors between SuperCOSMOS I and 2MASS before the relative positional mapping. The solid line represents the errors in Right Ascension while the dotted line shows those in Declination. The J, H and K (K_s) magnitudes are from 2MASS.

ric solution. Also the reddest objects may only appear on the I plate and hence will have no calculated astrometric solution. In order to make sure that all objects had a reliable astrometric solution, a procedure to calculate the astrometric solution using only the I plate and 2MASS data has been developed. Firstly a set of reference stars within 30 arcminutes and with I and J magnitudes similar (± 1 magnitude) to the star whose proper motion was being examined was selected. These reference stars are then used to produce a linear fit between the plates, to account for plate to plate scaling and orientation errors. The stars positions are then corrected for plate to plate errors and used to find the proper motion. The plate to plate fit also provides an estimate of the typical error for objects near the target star and this is used to calculate the error in the proper motion. In the case where an object has a calculated astrometric solution, both from the I plate-2MASS fitting procedure and from the SuperCOSMOS software, the most accurate one is quoted. Unfortunately some objects did not have enough reference stars to produce a plate model. These had their proper motions found in the same way to those with enough reference stars with the only difference being the lack of corrections for plate to plate errors. The error estimate for these stars was calculated using the positional errors for objects of an appropriate J magnitude shown in Figure 4.2.

4.4 Survey Results

As stated before the survey was carried out in two segments. The first (SIPS–I; Deacon et al. 2005a) searched for only the highest proper motion stars, those with $\mu > 0.5$"/yr. This produced 144 objects, 70 of them new discoveries. The results of this survey are shown in histogram in Figure 4.4 and in a two colour diagram in Figure 4.3. The SIPS–II survey (Deacon & Hambly, 2007a) searched for a larger sample of objects with proper motions above a tenth of an arcsecond per year. This yielded 6904 objects, histograms of which are plotted in Figure 4.5. As the SIPS–II run used positions after relative astrometric mapping it also detected 63 objects which had proper motions greater than 0.5"/yr and had not been previously found in SIPS–I. Details of all these objects can be found in Appendix A.

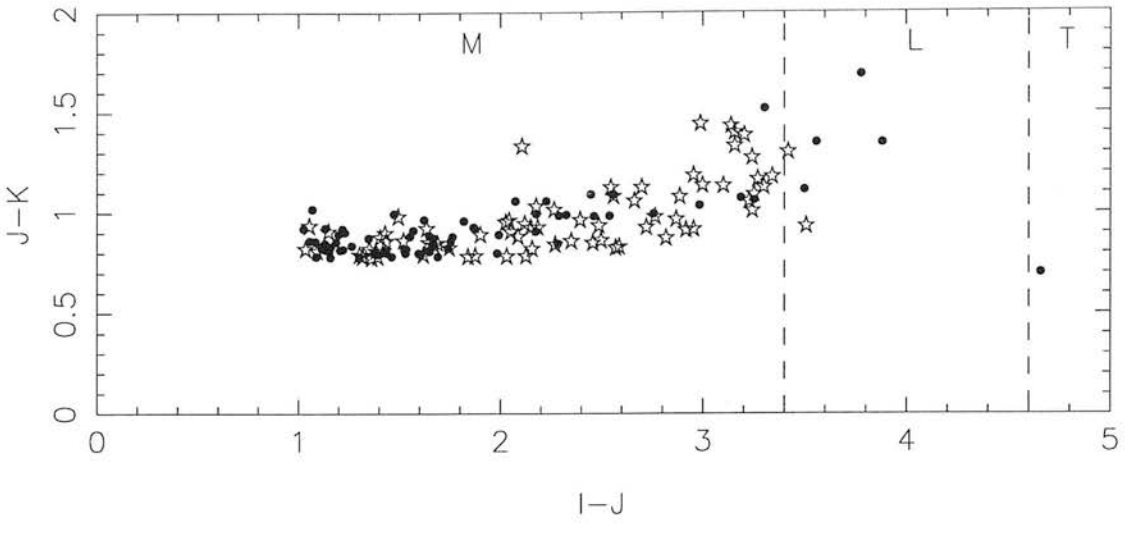

Figure 4.3: A two colour diagram showing objects found in the SIPS–I survey. The black dots are previously known objects and the stars are new discoveries.

4.4.1 Interesting Individual Objects

In order to identify potential L and T dwarfs, every object found with $I - J > 3.5$ was selected. The photometry and proper motions of these objects are shown in Table 4.1. Comparing the $J - K_s$ colours with those for different spectral types in Kirkpatrick et al. (2000) it becomes clear that all the objects except SIPS1625–2508 are early–mid L dwarfs. In fact Fan et al. (2000) spectroscopically identified that SIPS0539–0059 (SDSS 0539–0059) is an L5 dwarf and Kendall et al. (2006) identify SIPS2255–5713 and SIPS0128–5545 as L5.5 and L1 respectively. Additionally Reid et al. (2007) finds that SIPS0719–5051 (2MASS J07193188–5051410) is an L0 dwarf, Martín et al. (1999) identified SIPS0255–4700 as an L6 dwarf and Kendall et al. (2004) finds SIPS1539–0520 to be an L2. SIPS2204–5646 is the binary T dwarf ϵ Indi B Scholz et al. (2003). It appears from the J, H, K_s colours that SIPS1625-2508 is a late M dwarf. The J, H, and K_s photometry of each object was also compared to the values which Kirkpatrick et al. (2000) quote as typical for different spectral types. All objects in the SIPS–II sample (Deacon & Hambly, 2007a) redder in $J-H$, $J-K_S$, $H-K_s$ than Kirkpatrick's values for an M9 dwarf are listed in Table 4.2.

Table 4.1: Objects with $I - J > 3.5$ found in this survey.

Name	μ (arcsecs/yr)	I	J	H	K_s	Previously found in
SIPS2255-5713	0.341	17.85	14.08	13.19	12.58	Kendall et al. (2006)
SIPS2204-5646	4.840	16.567	11.9080	11.306	11.208	Scholz et al. (2003)
SIPS0128-5545	0.293	17.45	13.78	12.92	12.34	Kendall et al. (2006)
SIPS0719-5051	0.141	17.60	14.09	13.28	12.77	Reid et al. (2007)
SIPS0255-4700	1.197	17.025	13.246	12.204	11.558	Martín et al. (1999)
SIPS1155-3727	0.868	16.370	12.811	12.040	11.462	Cruz et al. (2003)
SIPS1625-2508	0.147	17.80	13.75	13.12	12.73	
SIPS1539-0520	0.644	17.805	13.922	13.060	12.575	Kendall et al. (2004)
SIPS0539-0059	0.363	17.84	14.03	13.10	12.53	Fan et al. (2000)

Table 4.2: Objects in SIPSII with photometry suggesting they are L dwarfs. Our photometric spectral classifications are based on the colours in Kirkpatrick et al. (2000).

Name	μ ("/yr)	I	J	H	K_s	Photometric Spectral Class	Previous Spectral Class	Previously found in
SIPS1753-6559	0.393	17.53	14.10	13.11	12.42	L2.5		
SIPS2045-6332	0.223	15.95	12.62	11.81	11.21	L0		
SIPS2255-5713	0.341	17.85	14.08	13.19	12.58	L1.5	L5.5	Kendall et al. (2006)
SIPS0128-5545	0.293	17.45	13.78	12.92	12.34	L1	L1	Kendall et al. (2006)
SIPS1341-3052	0.196	17.96	14.61	13.73	13.08	L2		
SIPS2026-2943	0.417	17.78	14.80	13.95	13.36	L1		
SIPS0316-2848	0.206	17.88	14.58	13.77	13.11	L1.5	L0	Cruz et al. (2003)
SIPS0614-2019	0.308	17.90	14.78	13.90	13.38	L0.5		
SIPS1058-1548	0.249	17.61	14.16	13.23	12.53	L2.5	L3	Delfosse et al. (1997)
							Kirkpatrick et al. (1999)	
SIPS1228-1547	0.415	17.62	14.38	13.35	12.77	L2	L5	Delfosse et al. (1997)
							Kirkpatrick et al. (1999)	
SIPS0847-1532	0.246	16.42	13.51	12.63	12.06	L1	L2	Cruz et al. (2003)
SIPS0408-1450	0.256	17.44	14.22	13.34	12.82	L1	L2	Cruz et al. (2003)
SIPS0058-0651	0.304	17.67	14.31	13.44	12.90	L1	L0	Dahn et al. (2002)
							Cruz et al. (2003)	
SIPS0539-0059	0.363	17.84	14.03	13.10	12.53	L1.5	L5	Fan et al. (2000)

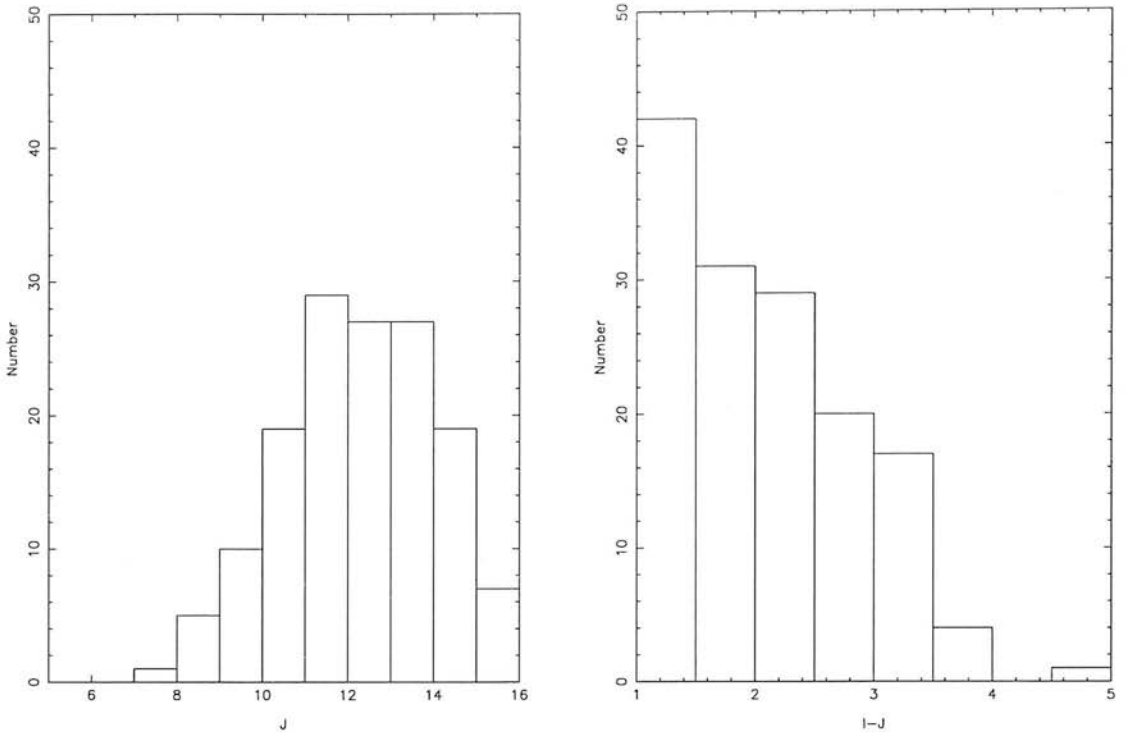

Figure 4.4: Histograms showing the magnitude (J) and colour ($I - J$) of objects found in the SIPS–I survey (those with $\mu > 0.5$"/yr).

4.4.2 Common Proper Motion Binaries

During the visual inspection phase of the data reduction process it became apparent that there were many SIPS objects which shared a common proper motion. However it is often difficult to distinguish objects in the same moving group from gravitationally bound wide binaries. To separate these two classes of objects a histogram of the separations of objects which had proper motions within 2σ of each other was plotted. This is shown in Figure 4.6. The straight line marks the expected distribution of objects in the same moving group randomly placed around the other object. Clearly the vast majority follow this pattern. However the higher than expected number of pairs with separations less than one arcminute indicates that a population of binaries also contributes to this. Hence we choose a maximum separation of three arcminutes for our binary sample. A list of SIPS objects with separations less than this and proper motions within 2σ of each other is shown in Table 4.3. Additionally during the cross-

Table 4.3: SIPS objects which share common proper motions with other SIPS objects. PA = Position Angle. For NLTT objects see Luyten, for LEHPM objects see Pokorny et al. (2003), for WT objects see Wroblewski & Costa (2001) and for [1] see Giclas et al. (1971). Pairs marked with * were identified as binaries by Luyten (1988).

Name	Position	μ ("/yr)	PA (°)	σ_μ ("/yr)	I	J	H	K_s	Other Name
SIPS0650-7041	06 50 59.75 -70 41 37.6	0.253	2	0.025	16.85	14.67	14.00	13.51	
SIPS0651-7041	06 51 02.78 -70 41 38.8	0.253	1	0.013	15.49	13.57	12.97	12.67	
SIPS2241-5915b	22 41 54.36 -59 15 30.8	0.323	94	0.018	16.39	13.66	13.08	12.67	
SIPS2241-5915a	22 41 59.83 -59 15 12.4	0.334	91	0.016	11.25	9.83	9.28	9.01	LEHPM 5030
SIPS0630-5525a	06 30 19.69 -55 25 48.2	0.254	137	0.007	13.71	12.42	11.87	11.59	
SIPS0630-5525b	06 30 23.39 -55 25 34.6	0.267	136	0.014	16.35	14.22	13.68	13.28	
SIPS1917-5238b	19 17 02.31 -52 38 47.0	0.254	181	0.016	11.26	9.94	9.35	9.08	LDS 673b*
SIPS1917-5238a	19 17 05.65 -52 38 49.8	0.258	182	0.014	11.40	10.19	9.64	9.31	LDS 673a*
SIPS0358-5026	03 58 15.41 -50 26 36.6	0.179	34	0.022	16.73	14.69	14.10	13.75	
SIPS0358-5027	03 58 18.69 -50 27 39.8	0.179	31	0.011	14.65	13.24	12.69	12.40	
SIPS0126-5022	01 26 55.26 -50 22 37.9	0.144	109	0.020	17.16	14.61	14.05	13.68	
SIPS0127-5023	01 27 02.59 -50 23 20.2	0.170	112	0.023	17.62	14.81	14.16	13.62	
SIPS1131-4419	11 31 00.17 -44 19 08.9	0.111	269	0.011	12.11	11.03	10.40	10.15	
SIPS1131-4418	11 31 01.35 -44 18 54.4	0.120	267	0.009	14.04	12.69	12.05	11.77	
SIPS0207-4052b	02 07 54.69 -40 52 16.4	0.255	206	0.016	12.45	11.36	10.82	10.55	NLTT7110*
SIPS0207-4052a	02 07 55.77 -40 52 30.9	0.251	209	0.015	12.53	11.49	10.96	10.66	NLTT7107*
SIPS0116-4005b	01 16 13.97 -40 05 02.1	0.170	96	0.011	14.06	12.56	11.98	11.69	
SIPS0116-4005a	01 16 15.44 -40 05 12.1	0.157	95	0.011	16.10	14.36	13.78	13.40	
SIPS2145-3612	21 45 49.39 -36 12 25.9	0.121	151	0.020	13.47	12.42	11.81	11.56	
SIPS2145-3610	21 45 54.45 -36 10 55.8	0.119	153	0.021	15.56	14.26	13.66	13.41	
SIPS0252-3438a	02 52 32.11 -34 38 49.0	0.308	86	0.011	14.04	12.53	11.93	11.63	LEHPM 2856*
SIPS0252-3438b	02 52 33.26 -34 38 54.3	0.303	86	0.011	13.69	12.25	11.68	11.38	LEHPM 2857*
SIPS0118-2730	01 18 10.69 -27 30 39.0	0.117	90	0.011	15.86	13.90	13.27	12.95	
SIPS0118-2729	01 18 06.58 -27 29 03.3	0.115	85	0.014	13.94	12.45	11.90	11.61	
SIPS0215-2440	02 15 13.69 -24 40 06.2	0.177	89	0.010	14.89	13.23	12.61	12.36	LDS 3363b*
SIPS0215-2439	02 15 15.02 -24 39 43.6	0.181	90	0.010	14.14	12.54	11.97	11.66	LDS 3363a*
SIPS1018-2028a	10 18 12.27 -20 28 22.1	0.397	285	0.010	12.21	10.59	10.01	9.71	NLTT23954*
SIPS1018-2028b	10 18 14.01 -20 28 41.9	0.407	286	0.013	10.28	9.00	8.42	8.15	NLTT23956*
SIPS0427-1548	04 27 20.96 -15 48 33.2	0.170	111	0.021	17.19	14.48	13.71	13.28	
SIPS0427-1547	04 27 22.20 -15 47 59.0	0.160	112	0.009	13.48	12.07	11.48	11.17	
SIPS0229-1540	02 29 44.57 -15 40 34.6	0.156	122	0.030	15.86	13.86	13.29	12.98	
SIPS0229-1541	02 29 46.98 -15 41 47.6	0.145	127	0.011	16.11	14.32	13.72	13.35	
SIPS0441-1356	04 41 58.63 -13 56 05.4	0.292	86	0.028	12.63	11.43	10.87	10.60	NLTT 13776
SIPS0442-1356	04 42 00.44 -13 56 23.7	0.278	77	0.034	15.21	12.98	12.36	11.97	
SIPS0116-1318a	01 16 48.12 -13 18 19.4	0.130	103	0.021	15.19	14.16	13.57	13.32	
SIPS0116-1318b	01 16 49.11 -13 18 55.0	0.133	105	0.021	16.42	14.93	14.41	14.07	
SIPS1402-0312	14 02 22.81 -03 12 16.9	0.401	176	0.020	12.55	11.52	10.99	10.68	NLTT 36053*
SIPS1402-0311	14 02 24.01 -03 11 55.5	0.393	175	0.021	12.20	11.08	10.57	10.28	G 64-36[1]*
SIPS0820-0231	08 20 12.08 -02 31 09.2	0.202	166	0.031	13.24	12.13	11.60	11.29	LDS 3786a*
SIPS0820-0230	08 20 12.74 -02 30 59.5	0.170	174	0.034	13.65	12.33	11.79	11.45	LDS 3786b*
SIPS0005-0139	00 05 36.22 -01 39 39.7	0.331	67	0.015	14.30	12.88	12.35	12.06	NLTT 175*
SIPS0005-0139	00 05 36.73 -01 39 57.2	0.336	66	0.015	13.00	11.86	11.31	11.07	NLTT 176*
SIPS2315-0045a	23 15 43.90 -00 45 00.8	0.124	84	0.009	14.34	12.46	11.88	11.58	LDS 6019a*
SIPS2315-0044b	23 15 46.52 -00 44 06.5	0.130	84	0.009	14.69	12.81	12.20	11.92	LDS 6019b*

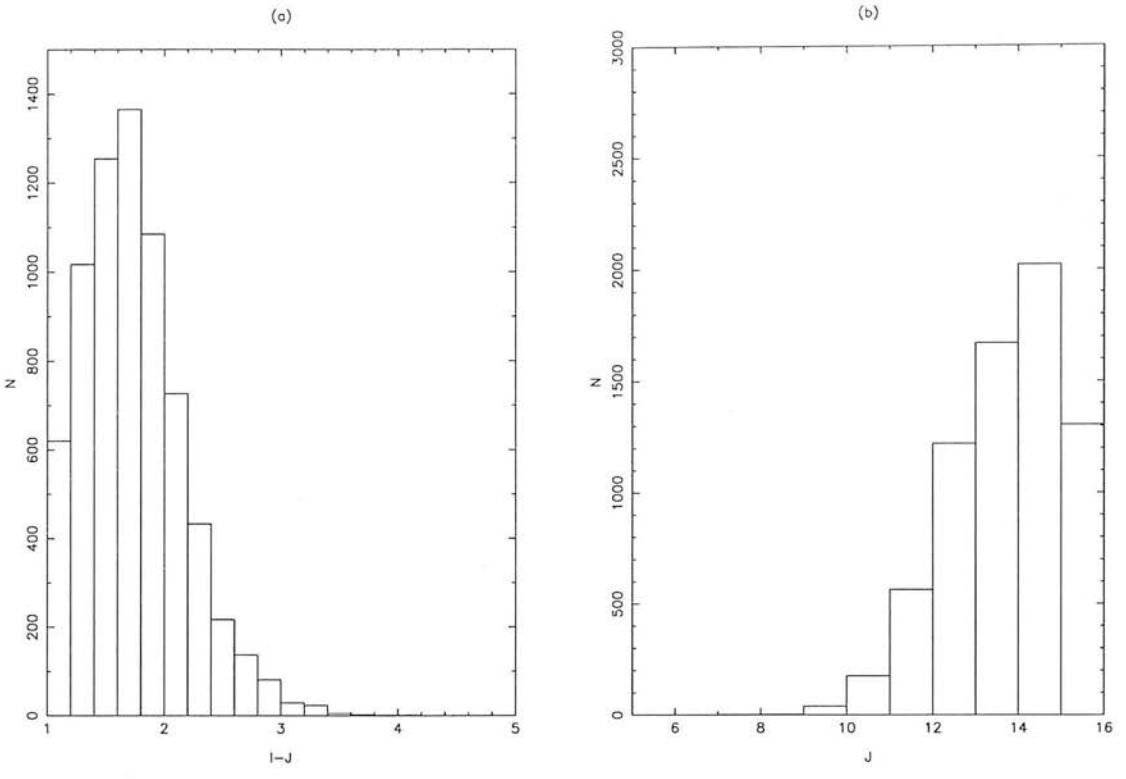

Figure 4.5: Histograms showing the magnitude (J) and colour ($I - J$) of the objects found in the SIPS–II survey (those with $\mu < 0.5$). The binning here is in smaller bins than in Figure 4.4 to allow more detailed comparison with the results of the simulations outlined in Chapter 6.

referencing process, several objects which, while clearly not the target SIPS object, had a similar proper motion to it were found. These were further investigated and any companion found to have a SuperCOSMOS proper motion differing by less than 2σ from the SIPS object is listed in Table 4.4. Note that due to the manual nature of this selection mechanism this list should not be regarded as complete.

SIPS1910−4132

When the candidate image for SIPS1910–4232 was inspected it was found that there were two objects moving with a similar proper motion. Astrometric solutions for these companion objects were found by the I plate-2MASS method as described in Section 3 and are shown in Table 4.5 along with the objects' photometry. It is clear that the

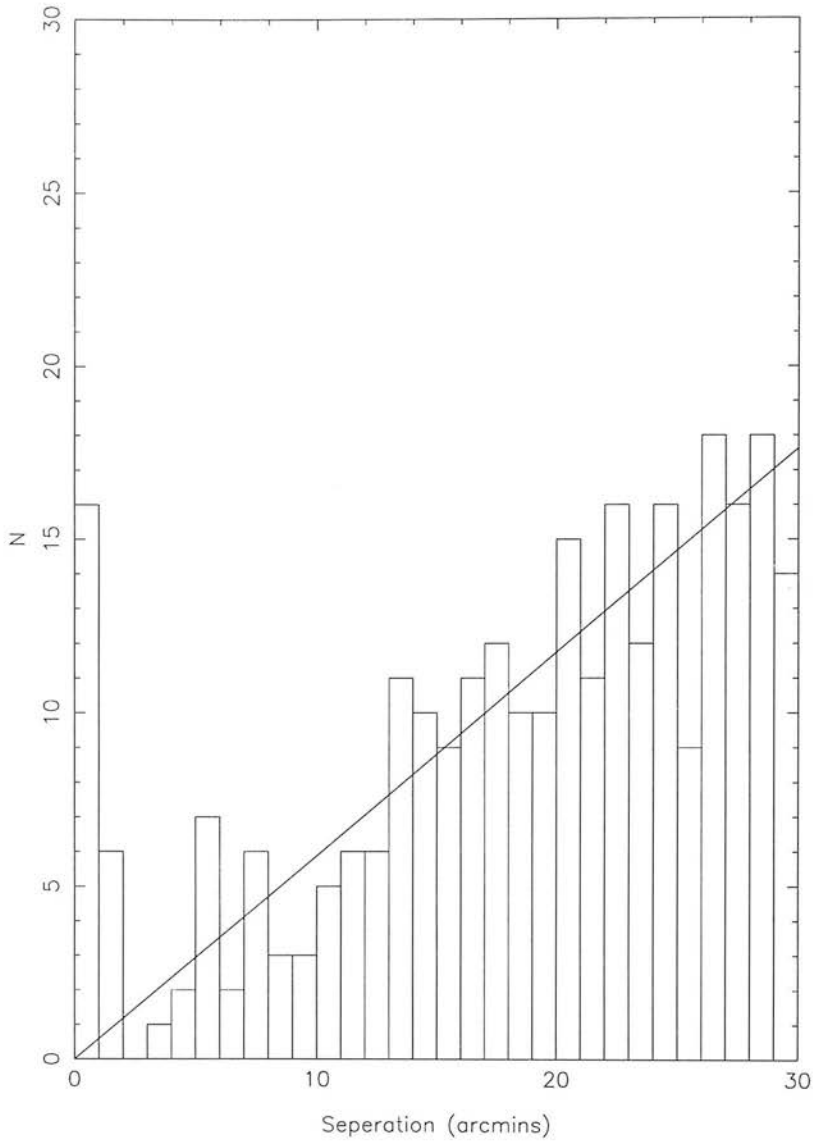

Figure 4.6: A histogram showing the seperations of objects with common proper motions in the SIPS survey. The line shows the expected distribution of randomly distributed objects (ie. those in the same moving group), $dn \propto rdr$

Table 4.4: SIPS objects which share common proper motions with objects found in other studies which are not themselves SIPS objects. PA = Position Angle. For LEHPM objects see Pokorny et al. (2003), for NLTT objects see Luyten (1980), [1] see Lasker et al. (1990), [2] see Gizis et al. (2000) and [3] see Schonfeld (1886). LDS objects and those marked with * were found by Luyten (1988).

SIPS0551-8116	05 51 54.60 -81 16 09.6	0.233	20	0.009	
NLTT 15903	05 52 38.16 -81 16 03.0	0.223	18	0.016	
SIPS2126-7337	21 26 20.62 -73 37 10.1	0.176	83	0.010	
GSC 09334-00112[1]	21 26 30.94 -73 38 23.2	0.184	85	0.016	
SIPS1954-6117	19 54 51.61 -61 17 05.5	0.214	163	0.033	
NLTT 48361	19 54 49.14 -61 19 19.1	0.190	177	-	
SIPS0447-5823	04 47 11.69 -58 23 21.0	0.279	30.263	0.029	
LEHPM 3838	04 47 13.38 -58 23 20.6	0.265	31.4	0.080	WT 155
SIPS1858-4513	18 58 21.39 -45 13 33.8	0.231	124	0.014	
NLTT 47218	18 58 16.68 -45 14 12.6	0.254	120	0.028	
SIPS0333-4324	03 33 18.57 -43 24 56.9	0.316	59	0.025	
NLTT 11245	03 33 18.03 -43 25 12.0	0.281	58	0.018	
SIPS0123-3507	01 23 24.56 -35 07 18.4	0.213	220	0.013	LEHPM 1491
NLTT 4642	01 23 29.93 -35 08 27.7	0.223	220	0.014	LEHPM 1492
SIPS0116-3342	01 16 31.19 -33 42 51.3	0.189	42	0.017	LDS 3257b*
NLTT 4263	01 16 32 78 -33 42 54.8	0.185	44	0.014	*
SIPS0933-2752	09 33 37.63 -27 52 47.4	0.328	297	0.022	
NLTT 22073	09 33 36.22 -27 52 25.0	0.311	289	0.017	
SIPS1917-2748	19 17 18.10 -27 48 54.0	0.209	133	0.028	LDS 4807b*
NLTT 47615	19 17 22.63 -27 47 32.26	0.195	141	0.008	*
SIPS0132-2744	01 32 35.91 -27 44 37.1	0.195	128	0.013	NLTT 5135*
NLTT 5136	01 32 37.48 -27 44 25.4	0.191	129	0.016	*
SIPS0028-2651	00 28 10.24 -26 51 24.7	0.189	208	0.015	NLTT 1492*
NLTT 1491	00 28 08.06 -26 52 25.8	0.198	207	0.021	*
SIPS2147-2644	21 47 44.64 -26 44 05.4	0.235	215	0.022	2MASSW J2147446-264406[2]
NLTT 52094	21 47 47.00 -26 42 52.7	0.252	211	0.012	
SIPS0227-2630	02 27 25.50 -26 30 07.8	0.165	56	0.012	NLTT 8057*
NLTT 8059	02 27 24.37 -26 29 42.1	0.159	60	0.022	*
SIPS1135-2017	11 35 05.43 -20 17 26.3	0.245	279	0.017	NLTT 27883*
NLTT 27884	11 35 05.03 -20 16 57.6	0.231	281	0.024	*
SIPS0133-1948	01 33 08.77 -19 48 34.3	0.307	65	0.021	NLTT 5169*
NLTT 5163	01 33 05.55 -19 50 22.7	0.322	67	0.022	*
SIPS1301-1848	13 01 51.64 -18 48 40.5	0.335	286	0.016	NLTT 32629*
NLTT 32636	13 01 42.64 -18 47 23.2	0.321	287	0.021	*
SIPS0532-1605	05 32 33.82 -16 05 53.2	0.272	186	0.023	
NLTT 15268	05 32 42.06 -16 06 00.3	0.289	189	0.025	
SIPS0536-1302	05 36 07.79 -13 02 09.4	0.199	162	0.013	NLTT 15357*
NLTT 15358	05 36 08.58 -13 02 40.1	0.202	174	0.025	*
SIPS2016-1100	20 16 49.26 -11 00 13.7	0.349	206	0.019	NLTT 48967*
NLTT 48973	20 16 55.72 -10 58 54.6	0.318	206	-	*
SIPS0321-0807	03 21 46.26 -08 07 13.7	0.118	72	0.014	
BD-08 638[3]	03 21 48.90 -08 06 10.58	0.127	76	0.019	
SIPS1402-0447	14 02 14.40 -04 47 53.2	0.231	254	0.018	NLTT 36042*
NLTT 36043	14 02 14.90 -04 48 09.0	0.214	250	0.021	*
SIPS0023-0342	00 23 30.92 -03 42 20.4	0.189	52.79	0.028	NLTT 1210*
NLTT 1213/1214	00 23 32.29 -03 42 28.4	0.232	55	-	*

three objects share a common proper motion and hence are likely to be a triple system. They all appear to be mid-late M dwarfs.

Table 4.5: The astrometric and photometric data for the apparent triple system SIPS1910–4132

Name	Position (J2000)	Epoch	μ_{tot}	PA	σ_μ	I	J	H	K_S
SIPS1910−4133A	19 10 34.50 -41 33 32.5	1983.346	0.742	174.4	0.017	11.008	9.851	9.245	9.032
SIPS1910−4133B	19 10 45.87 -41 33 28.9	1983.346	0.748	173.0	0.021	11.738	10.61	10.002	9.739
SIPS1910−4132C	19 10 33.49 -41 32 38.8	1983.346	0.738	174.7	0.016	12.557	11.147	10.552	10.249

SIPS0052−6201

The astrometric solution for this object suggests that it has a common proper motion with LHS 128. LHS 128 is a K5 dwarf with a parallax of 52 mas Perryman et al. (1997). If the two objects are part of the same system this yields a separation perpendicular to the line of sight of roughly 50,000 AU. It is also possible that the two objects are not part of a binary system but are simply members of the same moving group.

4.4.3 Completeness

As outlined already in this chapter and in Deacon et al. (2005a), there are many different sources of incompleteness.

As the final aim of this survey is to produce an estimate for the local space density, mass function and birthrate of late M, L and T Dwarfs the area covered by the survey needs to be analysed. Objects near the Galactic Plane have already been excluded. The other main problem related to crowding is that of the proximity flag given in the 2MASS Point Source Catalogue. As advised by the 2MASS Executive Summary all objects within 6 arcseconds of their nearest neighbour have been excluded; this will present completeness problems in crowded regions. In order to produce an estimate as to the magnitude of these completeness problems a series of simulations which allow the probability of an object having a proximity flag greater than 6 arcseconds for a given sky surface density of 2MASS images to be calculated were carried out. To do this a number of images were randomly placed in a one arcminute square box. If any of these fell with 6 arcseconds of the centre the test was deemed to have failed. However if no image fell with 6 arcseconds of the centre the test was deemed to have

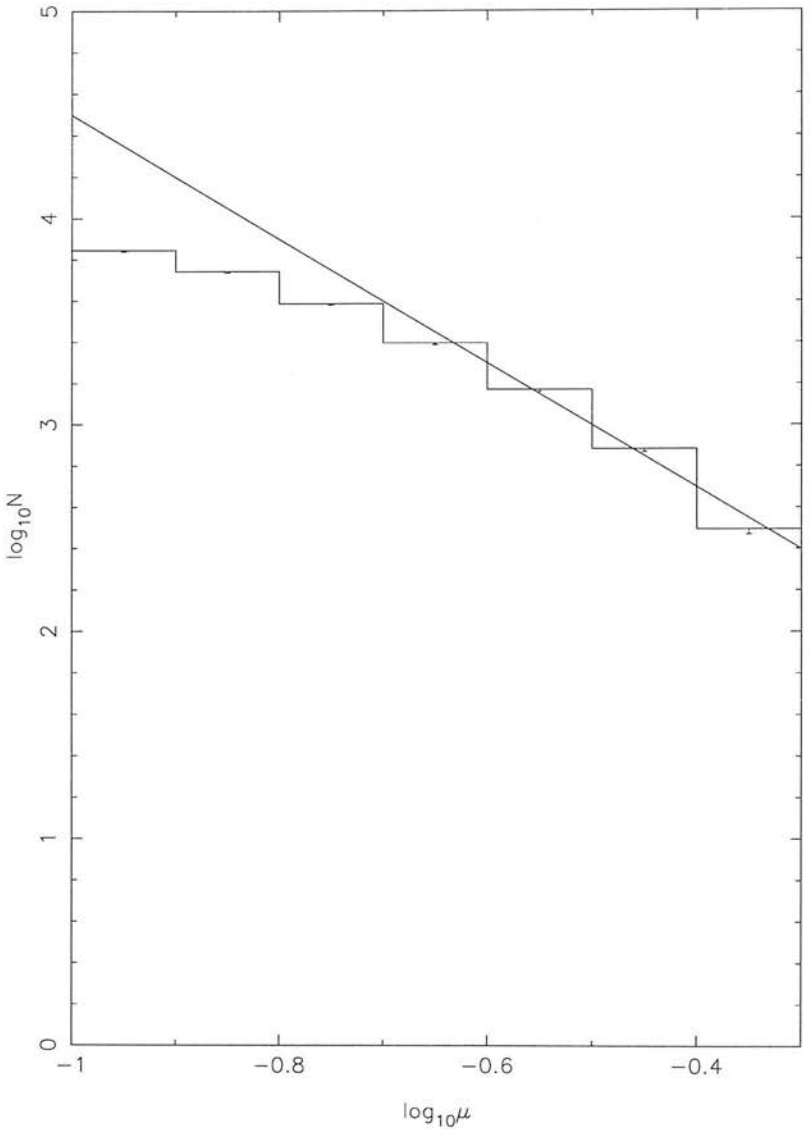

Figure 4.7: The cumulative number of objects with proper motions greater than the minimum limit of each bin. The solid line shows the $N \propto \mu^{-3}$ trend which would be expected for a totally complete sample. The proper motion (μ) is in arcseconds/year.

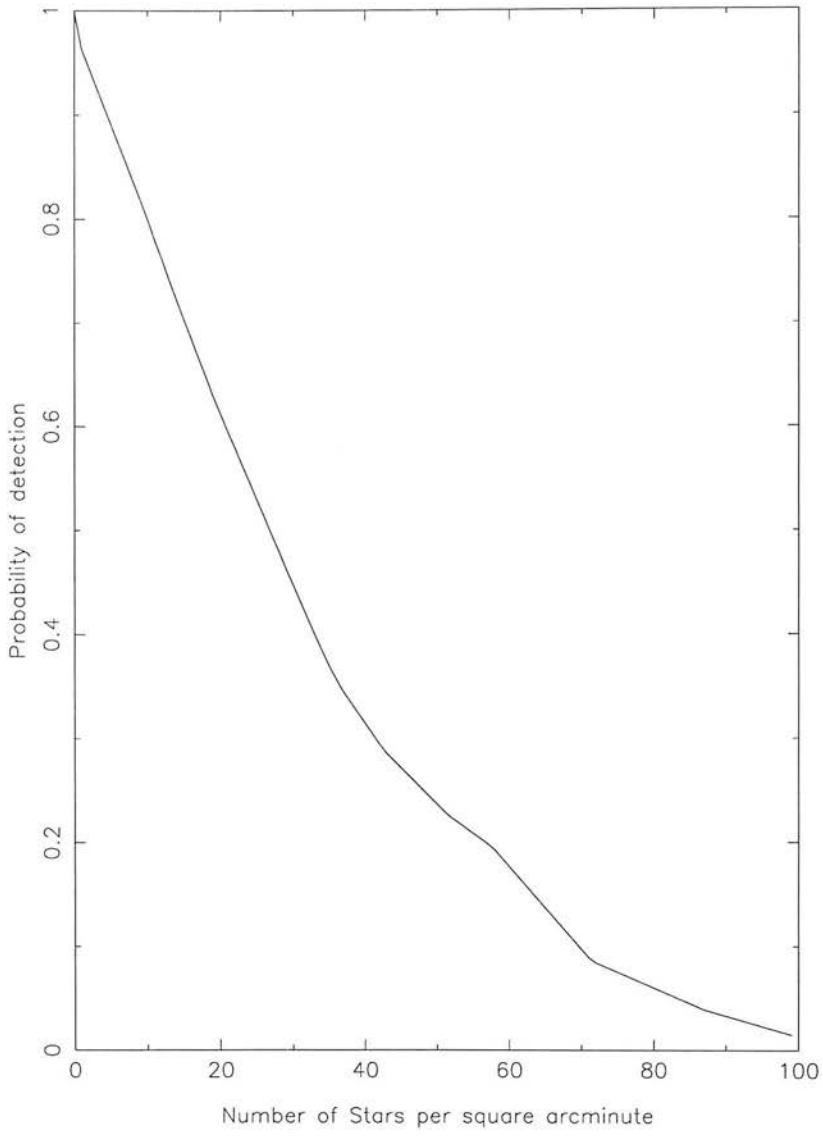

Figure 4.8: The probability of detection plotted against the number of 2MASS images per square arc minute.

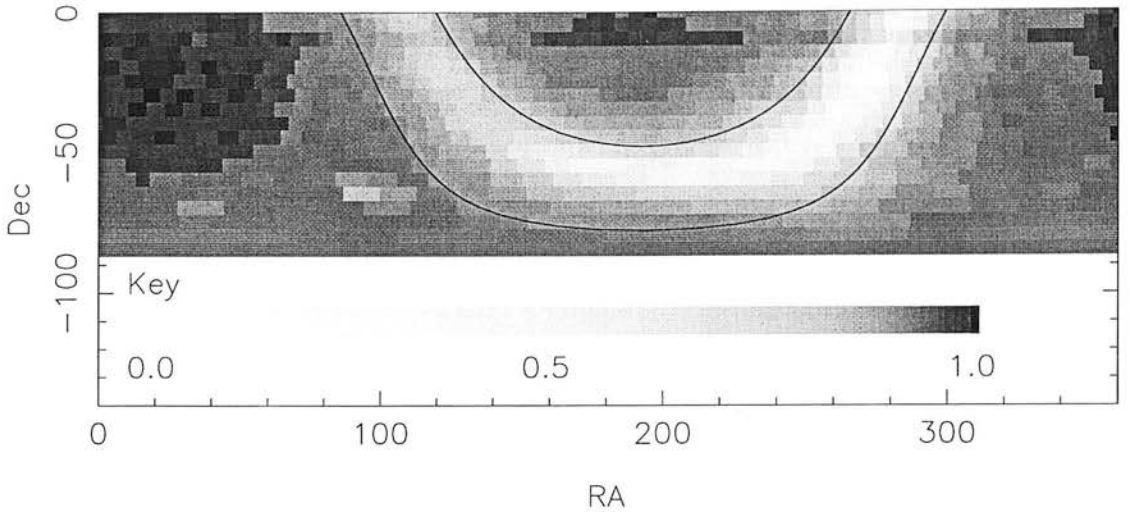

Figure 4.9: The areal completeness of the survey. The scale shows the probability that an area is free from both crowding and bright stars. The solid lines marked represent the galactic latitude cut of $|b| > 15°$.

succeeded. The probability of detection is thus the number of successful tests divided by the total number of tests. Simulations were carried out for different numbers of stars per square arc minute ranging from 1 to 100. The results of these simulations are shown in Figure 4.8. In order to calculate the probability of objects being identified in particular regions of the sky, the number of 2MASS images per square arcminute and hence the probability of detection were calculated for each UKST field.

In addition there will be areal completeness problems caused by areas of UKST plates which are near to bright stars. Luckily the size of these areas is calculated in the post processing of each SuperCOSMOS scan. Hence this probability of detection is simply multiplied by that for the 2MASS images to yield an estimate of the areal completeness for each field. Figure 4.9 shows these data as a grey-scale plot. It is clear that the galactic plane is crowded and hence unsuitable for inclusion in this survey.

There will also be incompleteness caused by both the limiting magnitudes of the survey and the short epoch separation on some plates. To illustrate this a histogram of the cumulative number of objects with proper motions greater than the minimum proper motion in each bin is plotted in Figure 4.7. If the survey was totally complete it would be expected that the number of objects in each bin would scale as μ^{-3} (see the

solid line). However it is clear that the incompleteness is significant below 0.25"/yr. Additionally the incompleteness in the SIPS I sample can also be estimated. To do this the number of objects which would be expected to be recovered from Luyten (1979) (ie. those with the correct colours, brightnesses etc.) was found. These are shown (as a function of Galactic latitude, proper motion, $I - -J$ colour and J magnitude) in Figure 4.10. It is clear that only roughly a quarter of these objects are recovered, the largest deficit coming with the low proper motion objects. This is to be expected as some of the plate epoch differences will be too small to detect low proper motion objects. Astrometric errors will also exclude objects from the SIPS I high proper motion sample. In order to gain information on the mass function and birthrate of cool dwarfs all the sources of incompleteness mentioned in this chapter must be taken into account. Chapter 6 deals with the simulations which use both the crowding incompleteness calculated here and the other selection effect to produce simulated samples. These are then used to constrain underlying distributions.

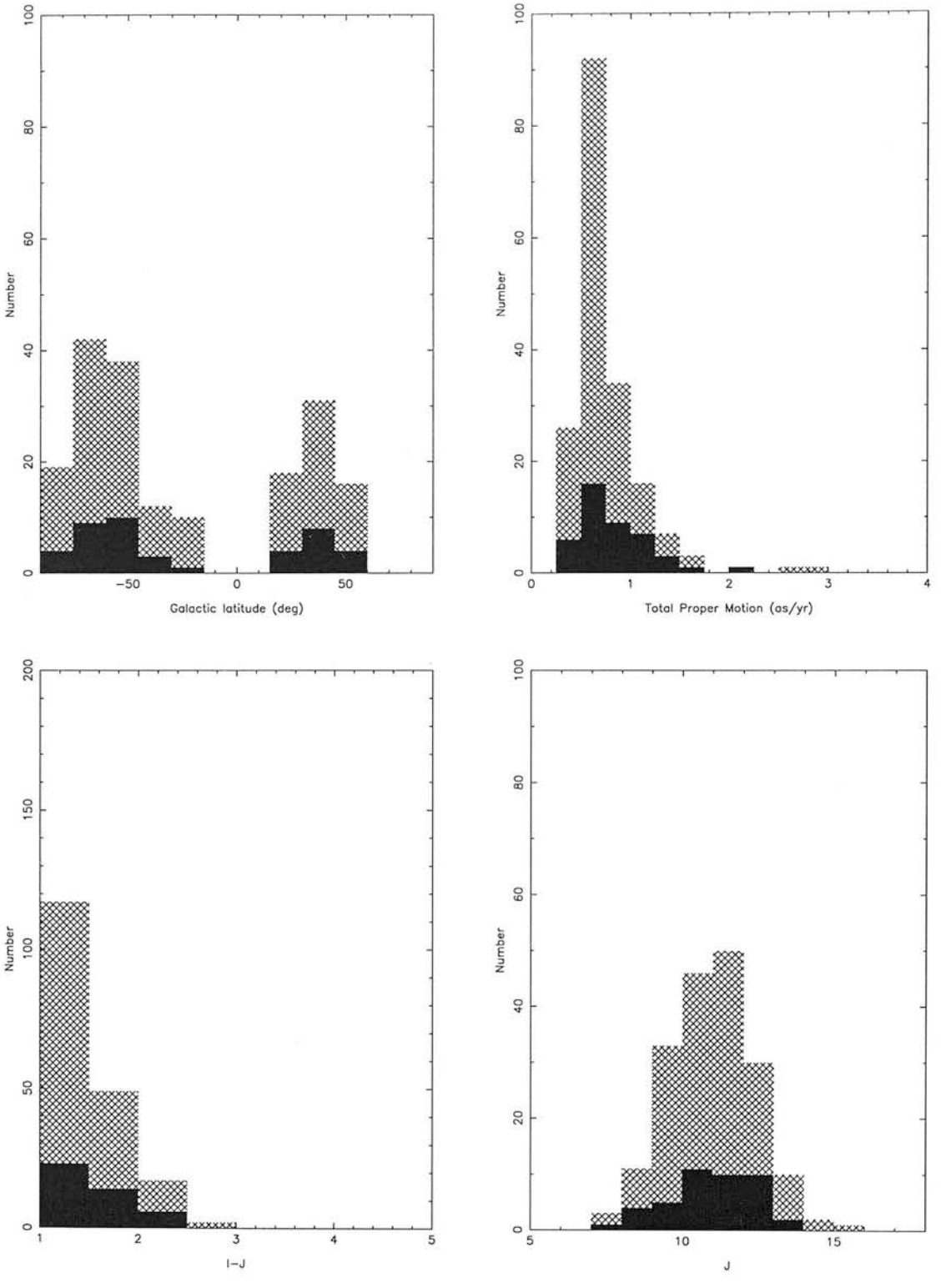

Figure 4.10: The number of Luyten objects that could possibly be detected (grey) and those that were (solid).

Chapter 5

Follow-up Observations of Individual Objects

The technique developed in Deacon & Hambly (2001) allows the measurement of trigonometric parallaxes of nearby relatively dim R≈16 objects. Here follow up measurements for two nearby stars are presented. One of these (SCR1845–6357) was found by Hambly et al. (2004) while the other (SIPS1259–4336) is the nearest object found in the Southern Infrared Proper Motion Survey. The result for SCR1845-6357 appears in Deacon et al. (2005b) while SIPS 1259–4336 appears in Deacon et al. (2005a). An infrared spectrum was also obtained for SIPS1259–4336 allowing a spectral classification. While these objects are identified in the Southern Infrared Proper Motion Survey these results will not be used to constrain the Initial Mass Function or Stellar Birthrate.

5.1 SCR1845–6357

The SuperCOSMOS–RECONS proper motion survey Hambly et al. (2004) identified five objects with proper motions greater than one arc second per year and with $\delta < 60°$. The nearest of these SCR1845–6357, (hereafter the target) was shown subsequently to have a photometric parallax of 4.6 ± 0.3 pc by Henry et al. (2004). Photometric data for the target are reproduced in Table 5.1. These show that the object is very red; Henry et al. (2004) classified the target as an M8.5 dwarf.

Table 5.1: Photometric data on SCR1845–6357. JHK magnitudes are taken from the Two Micron All Sky Survey, V, R and I measurements are from Henry et al. (2004). Note that the B_J measurement comes from a plate where the target image is deblended and hence may not be as accurate as the other measurements.

B_J	R_{59}	I_N	J	H	K_s	V	R	I
19.05	16.29	12.54	9.54	8.97	8.51	17.40	15.00	12.47

5.1.1 Observational Data and Reduction

Fortunately there is a wealth of astrometric data available for this object, partly because it lies in the overlap region between the standard Schmidt photographic survey fields, and partly because non–survey programmes have fortuitously observed the field containing the target frequently and over a long time baseline. The target was identified on two United Kingdom Schmidt Telescope (UKST) R survey plates and one European Southern Observatory (ESO) survey R plate. These had already been scanned as part of the SuperCOSMOS Sky Survey (Hambly et al. (2001b) and references therein). In addition six UKST non-survey R photographs from the UKST Plate Library were selected for their image quality and useful parallax factors, and were scanned especially for this study using SuperCOSMOS. Hence a total of nine Schmidt photographs were used, details of these are shown in Table 5.2. These also provide a nine year baseline, ideal for measuring an accurate proper motion.

Each plate was scanned individually on SuperCOSMOS and processed using standard methods (Hambly et al. (2001b) and references therein). Global astrometric plate solutions result in systematic errors of order ~ 0.2 arcsec in absolute positions. Hence it is necessary to correct for these; a local linear plate model with respect to the array of mean positions from all measures was employed for this purpose. A sample of circular, single, stellar images which are not affected by proximity to bright stars was selected as local astrometric reference stars. These reference stars were used to fit linear models for each of the plates with respect to the array of mean reference star positions. The residual errors from the reference stars after these models are applied give an indication

as to the astrometric quality of each plate; as a result of this test, one of the non–survey plates was excluded from the rest of the study owing to poor astrometric quality.

It is also important that the maximum distance of reference stars from the target is carefully chosen. Too small a distance and the number of reference stars will be too few, too large and non–linear plate effects may leave systematic errors in the linear fit (indicated by an increase in the RMS error). In order to choose the maximum reference star distance correctly several different selections were made and the average RMS errors (the mean of all the errors from all the plates) from the local linear plate fit were noted along with the number of reference stars. The results are shown in Table 5.3. We chose the maximum extent available (20 arcminutes) from the area in common between both plates as there is no indication of an increase in systematic errors up to this value.

5.1.2 Results

Once the process described in Section 5.1.1 was carried out, plate–to–plate systematic errors were eliminated, the relative astrometric quality of each plate with respect to the mean positional measures was determined and it was possible to apply a full weighted astrometric fit to the target and reference stars. Equations 5.1 and 5.2 show the astrometric models for Right Ascension and Declination respectively (where f_α and f_δ are the parallax factors in Right Ascension and Declination):

$$\alpha = \alpha_o + \mu_\alpha t + \pi f_\alpha; \tag{5.1}$$

$$\delta = \delta_o + \mu_\delta t + \pi f_\delta. \tag{5.2}$$

The error–weighted design matrix formed from these equations was solved via Singular Value Decomposition to yield a least–squares fit; numerical routines from the SLALIB positional astronomy library (Wallace (2003)) were employed. The results for the target (along with χ^2_ν, ie. χ^2 normalised per degree of freedom) are shown in Table 5.4. The total proper motion is 2.64 ± 0.0082 arcseconds/year with a position angle of 74.9 degrees. These compare with the values of 2.56 ± 0.013 arcseconds/year and 74.8 degrees quoted in Hambly et al. (2004). The proper motion measurements differ but this may be due to systematic errors in either measurement or because Hambly et al. (2004)

Table 5.2: Schmidt photographs used in the study of SCR1845–6357; relative astrometric quality is indicated (see text). One plate was excluded due to poor astrometric quality.

Plate No.	Date (ddmmyy)	LST	Zenith Angle	Emulsion	Filter	Exp. (min)	σ_x (mas)	σ_y (mas)	Material
				Plates Used					
OR15689	12/08/93	1746	34.0°	IIIaF	OG590	55	40	42	Original survey plate
OR16753	28/08/95	1850	32.7°	IIIaF	OG590	80	46	44	Original survey plate
ESOR6887	30/04/87	1713	37.7°	IIIaF	RG630	120	46	64	Glass copy of ESO survey plate
OR17012	24/03/96	1648	37.5°	4415	OG590	15	48	49	Original non–survey film
OR17038	15/04/96	1757	33.6°	4415	OG590	15	53	56	Original non–survey film
OR17256	15/09/96	1838	32.7°	4415	OG590	15	55	64	Original non–survey film
OR13751	20/06/90	1843	32.7°	IIIaF	OG590	60	41	42	Original non–survey plate
OR14370	16/06/91	1831	32.8°	IIIaF	OG590	55	40	39	Original non–survey plate
				Plate Not Used					
R 5991	16/05/80	2032	36.7°	IIIaF	RG630	150	107	92	Original non–survey plate

Table 5.3: Selecting the optimum maximum distance of reference stars from SCR1845–6357. Note the number of reference stars does not increase as the square of the maximum radius due to plate boundary cutoffs.

Maximum distance from target (Arcminutes)	Average RMS error (mas)	Number of reference stars
20	56	108
18	56	108
16	56	98
14	58	77
12	59	56
10	58	41

did not include a parallax in their astrometric solution. Figure 5.1 shows the deviation in position of the target from its proper motion. Figure 5.2 shows the parallax ellipse traced out by the target.

As a test of the astrometry, each reference star was also run through the same astrometric model fitting procedure and the proper motions and parallaxes of the reference stars were found. These are plotted in Figure 5.3 along with the target. It is clear that the target is well separated from the mass of reference stars. In general the reference stars have proper motions and parallaxes consistent with zero (and a mean value of $\chi^2_\nu \sim 1.35$ indicating good model fits) and hence are good reference stars. To further investigate the reference star distances, and for the purposes of correcting the measured (ie. relative) parallax to an absolute parallax, the mean B_J–R and R for the reference stars were found. The mean B_J–R calculation was then used to find that the mean spectral type (assuming they are dwarfs) for the reference stars is G5. From this the mean expected absolute R magnitude can be deduced which combined with the mean R magnitude yields the mean expected distance of the reference stars. The mean expected trigonometric parallax of the reference stars was thus found to be $\pi = 0.7$ mas. This is clearly insignificant compared to the formal error on the parallax for the target,

Table 5.4: The full astrometric solution for SCR1845–6357.

Parameter	Fitted Value	Error	Units
RA on 01/01/2000	$18^h45^m05^s.2008$	0.0407 as	—
Dec on 01/01/2000	$-63°57'47".355$	0.0435 as	—
μ_α	2.5495	0.0055	as/yr
μ_δ	0.6874	0.0061	as/yr
π	282.33	22.58	mas
χ^2_ν	1.26		

so no correction from relative to absolute parallax was made. To further test that the method used was sound, 100 sets of simulated data were created. Each had the same astrometric parameters as the target and each data point was given a random Gaussian error calculated from the RMS error estimates of the particular plate. These were then run through the astrometric solution fitting program. No significant offsets were found and the error on the parallax calculated from the scatter of the simulated data solutions was in good agreement to that predicted by the astrometric solution. Finally, differential colour refraction (DCR) effects between the reference stars and the target were examined. Nigel Hambly found these to be negligible compared to the random errors on each point. For details on his calculation see Deacon et al. (2005b).

5.1.3 Discussion

The calculated trigonometric parallax for the target gives a distance of 3.5 ± 0.3 pc. Consulting the RECONS list of nearby stars (Henry, T.J., 2006) we find that this makes SCR1845–6357 the 16th nearest stellar system to the Sun. The upper and lower one sigma error boundaries would make it the 23rd and 10th nearest stellar system respectively. The RECONS photometric parallax is 4.6 ± 0.3 pc Henry et al. (2004) but the new trigonometric parallax puts this object 2.8σ nearer than was first estimated. The RECONS trigonometric parallax was found by Henry et al. (2006) to be 259.45 ± 1.11 milliarcseconds.

Recently Biller et al. (2006) have found a companion to SCR 1845-6357 1.170±0.003"

(4.5AU) away from the primary. It is estimated to have a spectral type of T5.5±1. The bound nature of this system was confirmed by Montagnier et al. (2006).

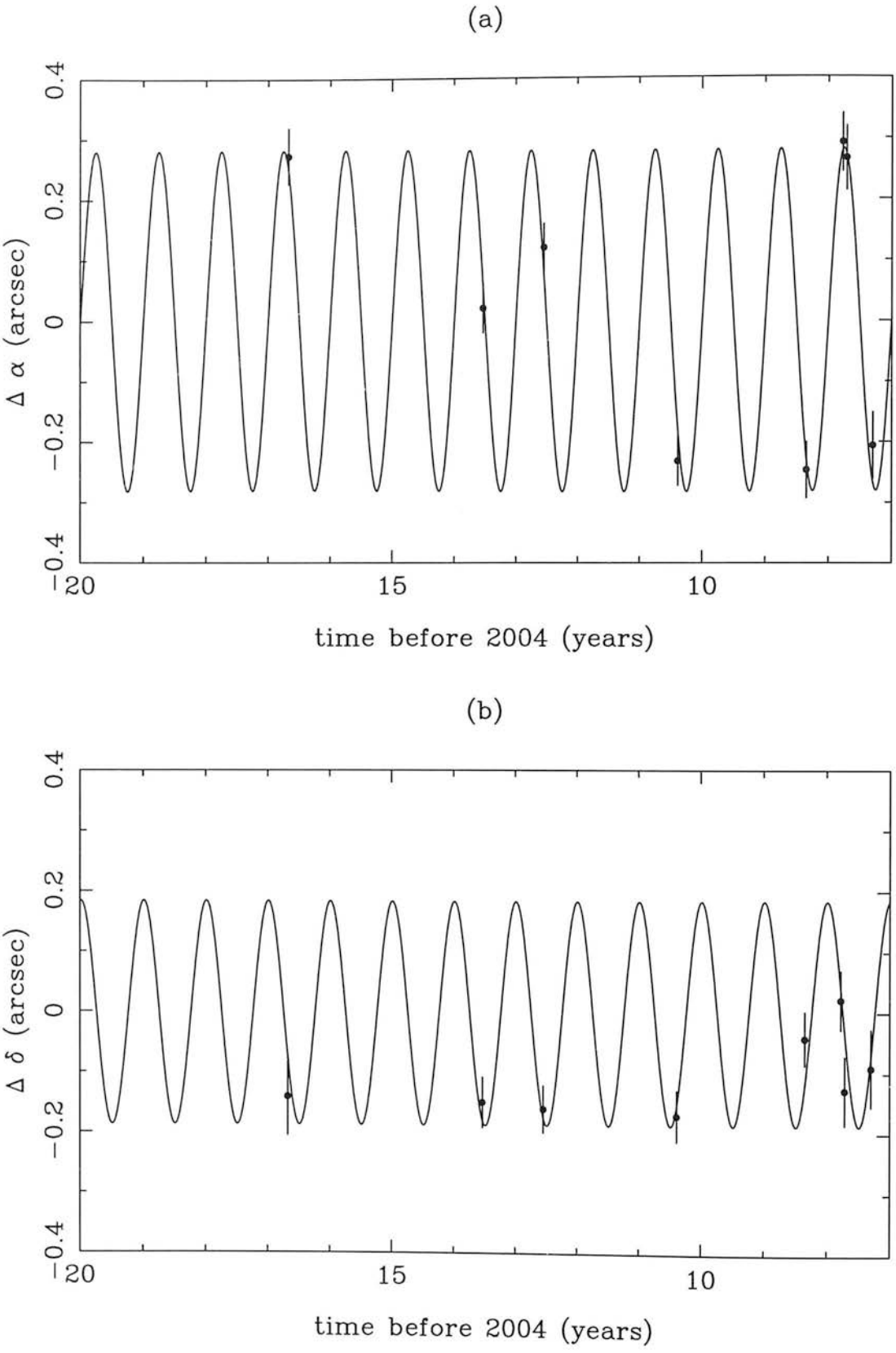

Figure 5.1: The parallax motion of SCR1845–6357 in Right Ascension and Declination vs. time.

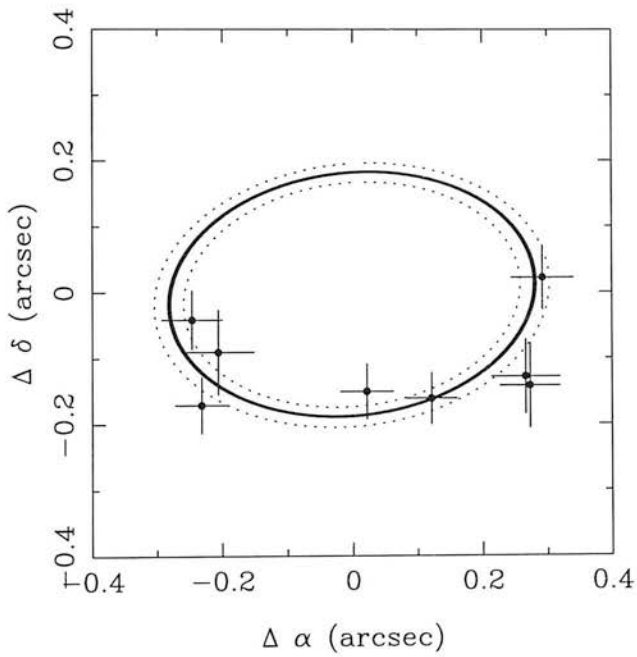

Figure 5.2: The parallax ellipse for the fitted value (solid line) found for SCR1845–6357 along with those for one sigma errors (dotted lines) plotted against the data.

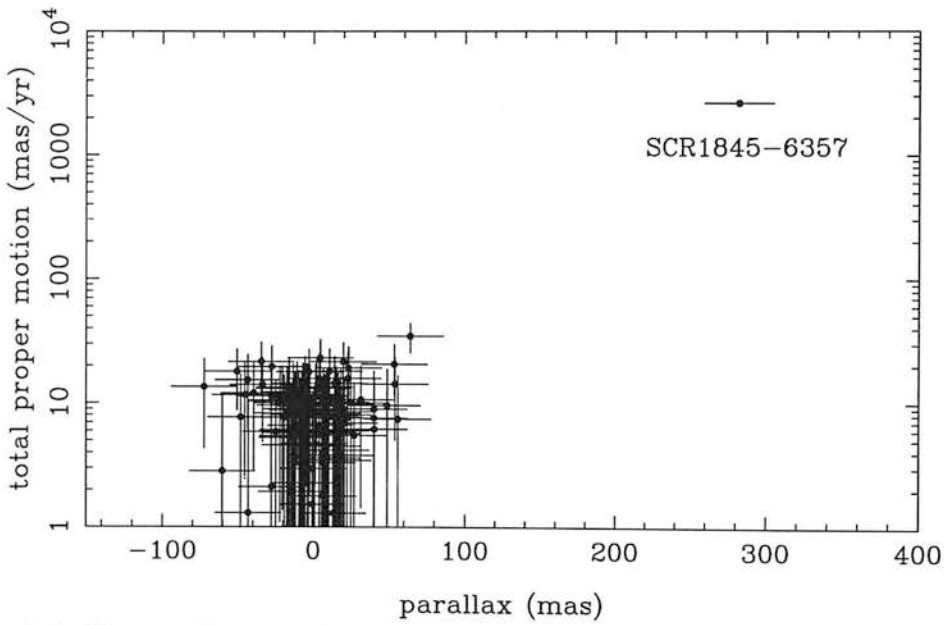

Figure 5.3: The parallaxes and proper motions for the reference stars and SCR1845–6357. It is clear that SCR1845–6357 is well separated from the mass of reference stars.

5.2 SIPS1259–4336

5.2.1 Introduction & Observational Data

SIPS1259–4336 was the most interesting of the objects newly identified in the Southern Infrared Proper Motion Survey. The photometric data shown in Table 5.5 shows that the object is very red, with similar infrared colours to SCR1845–6357, indicating that it is an M8.5 dwarf. Luckily there were several non-survey plates available for this object in the UKST plate library. Four of these were selected for their good parallax factors and were scanned on SuperCOSMOS and used along with the existing UKST R and ESO R plates. Details of the plates used are shown in Table 5.6.

Table 5.5: Photometric data on SIPS1259–4336. JHK magnitudes are taken from the Two Micron All Sky Survey. Note that the B_J measurement comes from a plate where the target image is deblended and hence may not be as accurate as the other measurements.

B_J	R_{59}	I_N	J	H	K_s
19.17	16.72	12.81	10.53	9.95	9.52

5.2.2 Results

The data from these plates were reduced using the same method as SCR1845-6357. A total of 148 reference stars were used to produce the plate to plate models. Once these had been applied to correct for plate to plate errors the astrometric solution could be found. This is shown in Table 5.7. The deviation from the proper motion is shown in Figure 5.4 with the parallax ellipse traced out by the object shown in Figure 5.5. To check for any systematic errors the reference stars were run through the fitting procedure. Their proper motions and parallaxes are shown in Figure 5.6 along with those for SIPS1259–4336. It is clear that there is no significant offset in the parallax and that SIPS1259–4336 is well separated from the mass of reference stars. The mean χ^2_ν for the reference stars was found to be 0.97 indicating good model fits.

Table 5.6: Schmidt photographs used in the study of SIPS1259–4336; relative astrometric quality is indicated (see text). One plate was excluded due to poor astrometric quality.

Plate No.	Date (ddmmyy)	LST	Zenith Angle	Emulsion	Filter	Exp. (min)	σ_x (mas)	σ_y (mas)	Material
				Plates Used					
R 5108	25/06/79	1254	12.5°	IIIaF	RG 630	800	64	65	Original non-survey plate
ESOR4809	19/5/82	1200	18.6°	IIIaF	RG630	120	63	49	Copy of ESO survey plate
OR14770	12/02/92	1245	12.6°	IIIaF	OG 590	600	41	49	Original survey plate
OR16928	26/01/96	1142	19.6°	4415	OG 590	150	68	67	Original non-survey film
OR17069	26/04/96	1322	13.1°	IIIaF	OG 590	100	56	55	Original non-survey plate
OR17997	28/04/98	1314	12.7°	IIIaF	OG 590	600	77	65	Original non-survey plate

5.2.3 Spectral Data

Spectroscopic data for this object were obtained from IRIS2 at the Anglo-Australian Telescope. These data were bias, sky and dark subtracted, flat fielded and wavelength calibrated using IRAF packages .The spectrum in the J band is shown in Figure 5.7. Using the equivalent width of the potassium doublet as a diagnostic Gorlova et al. (2003) we find that it is likely to be an M8 dwarf.

5.2.4 Discussion

The calculated parallax of SIPS1259–4336 of 276.2 ± 40.6 milliarcseconds relates to a distance of 3.62 ± 0.54 parsecs. However recent measurements put SIPS1259–4336 substantially further away, around 7–8 pc (John Subasavage, private communication). When looking again at the data it is clear that with so few data points one slight movement in one could drastically alter the final parallax. The method used here has produced distance estimates for both SCR1845–6357 (Deacon et al., 2005b) and

DENIS1048–3956 (Deacon & Hambly, 2001) which have been agreement with subsequent, more accurate studies. Hence it is probable that the poor parallax measurement for SIPS1259–4336 has been caused by a lack of good data, rather than the method.

Table 5.7: The full astrometric solution for SIPS1259–4336.

Parameter	Fitted Value	Error	Units
RA on 01/01/2000	$12^{h}59^{m}04^{s}.7604$	0.0473 as	—
Dec on 01/01/2000	$-43°36'24''.213$	0.0474 as	—
μ_α	1.1050	0.0044	as/yr
μ_δ	-0.2623	0.0035	as/yr
π	276.2	40.6	mas
χ^2_ν	0.65		

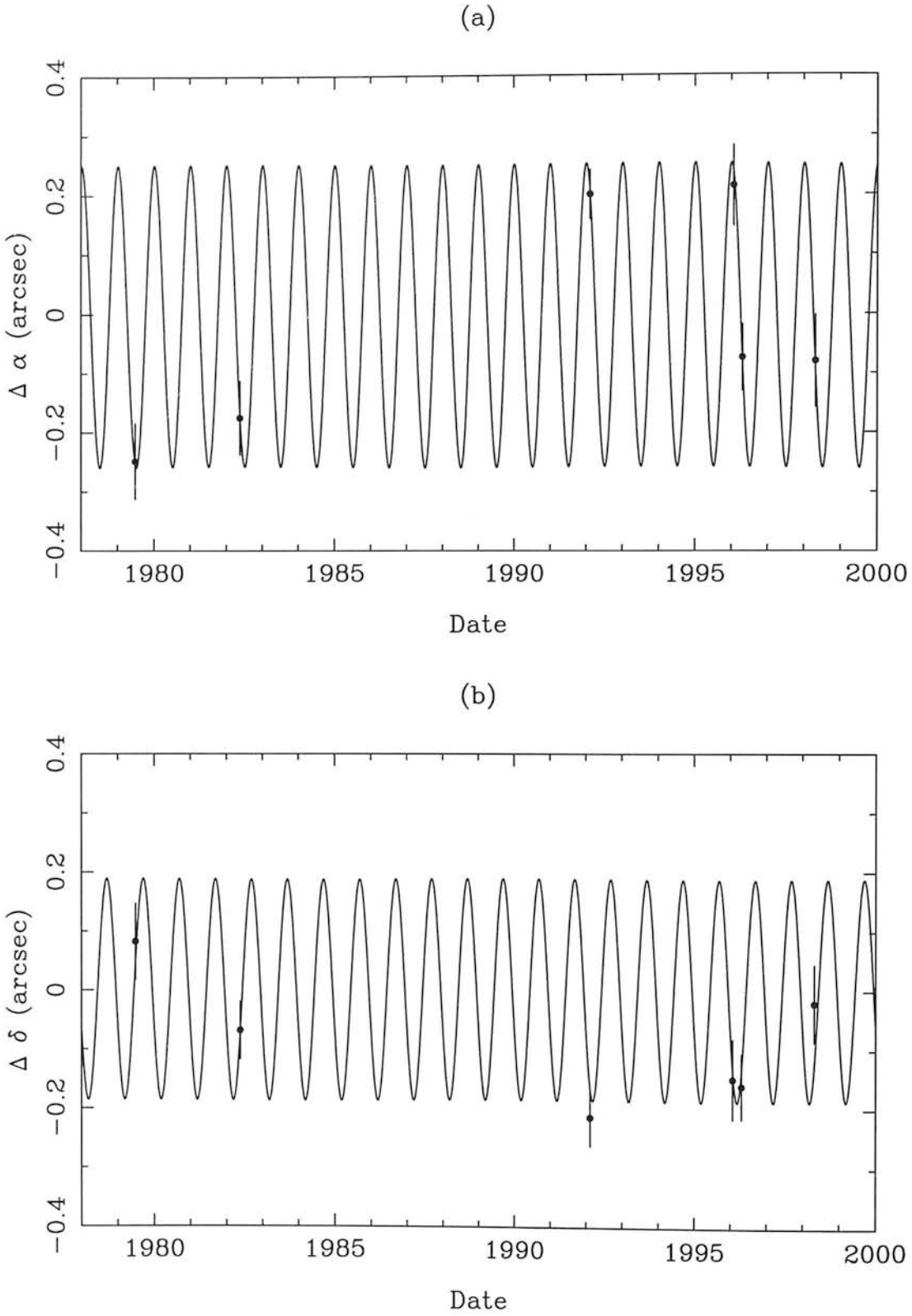

Figure 5.4: The parallax motion in of SIPS1259–4336 Right Ascension and Declination vs. time.

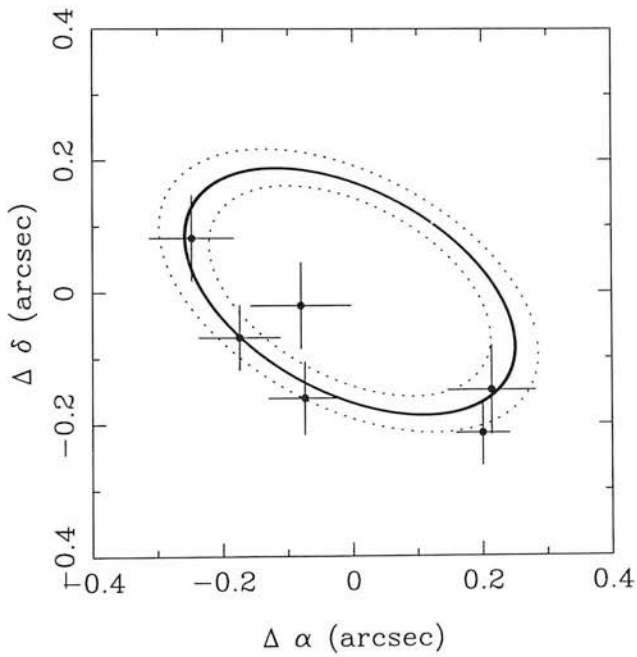

Figure 5.5: The parallax ellipse for the fitted value (solid line) for SIPS1259–4336 along with those for one sigma errors (dotted lines) plotted against the data.

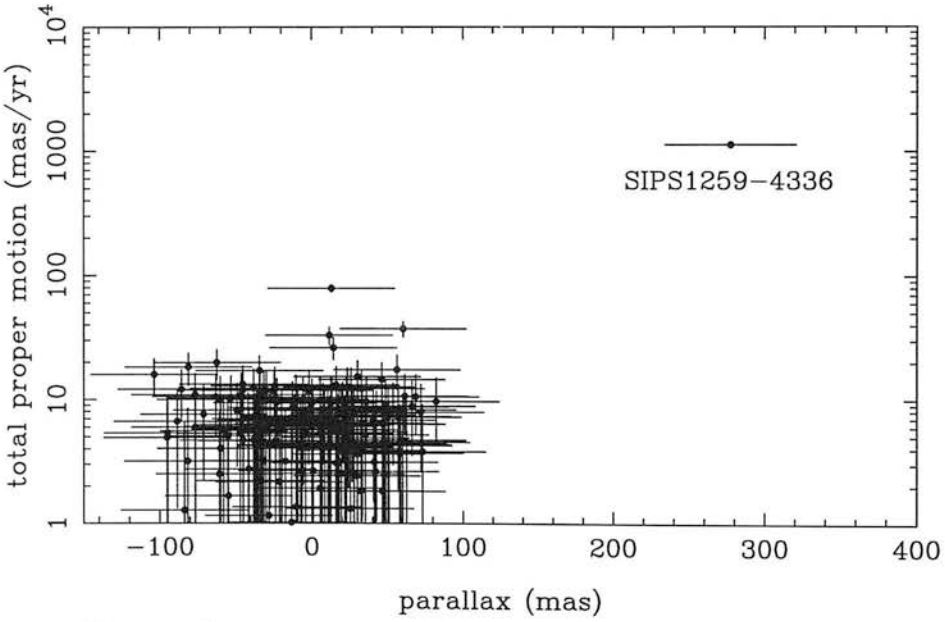

Figure 5.6: The parallaxes and proper motions for the reference stars and SIPS1259-4336. It is clear that SIPS1259–4336 is well separated from the mass of reference stars.

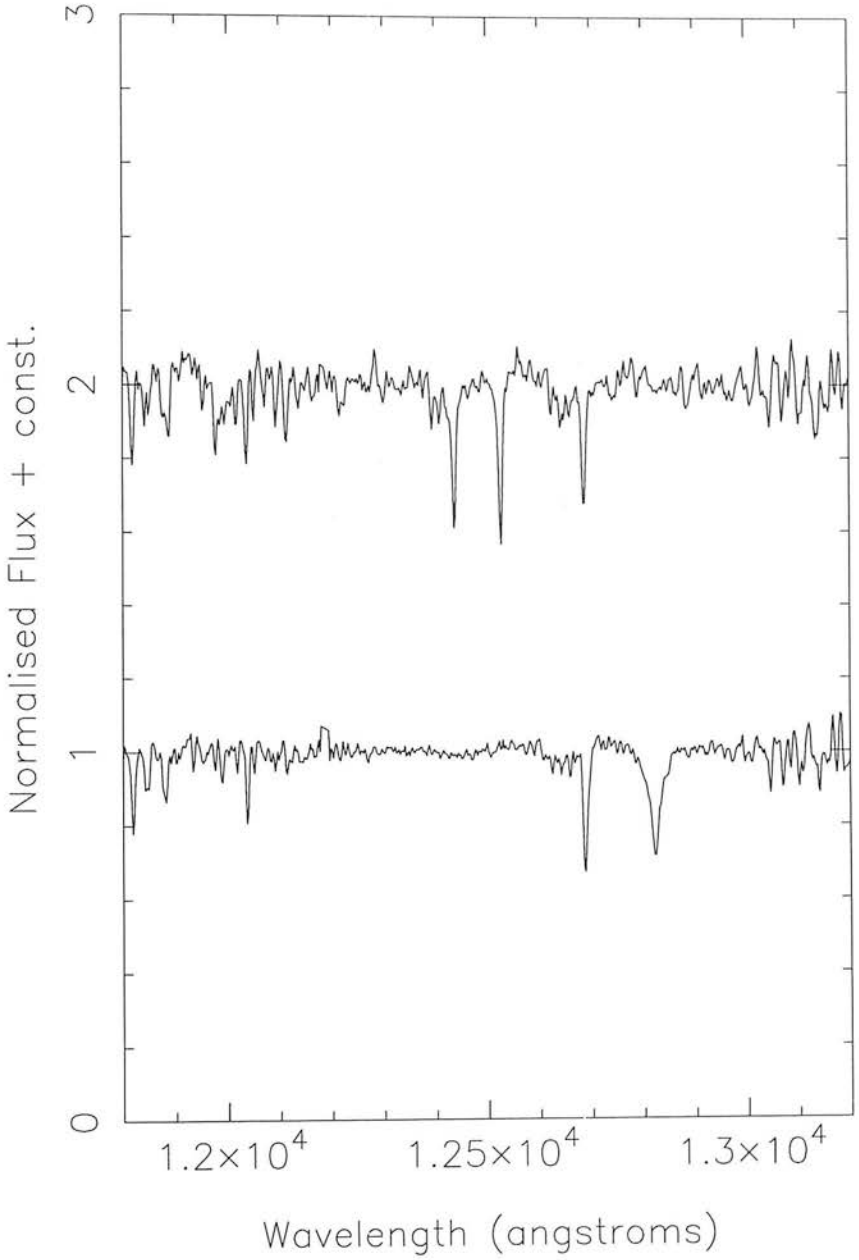

Figure 5.7: The normalised spectra for SIPS1259–4336 (top) and the standard (bottom). The potassium doublet at 1.25 microns can clearly be seen.

Chapter 6

Simulations of the Field Luminosity Function

The ultimate aim of studies of the luminosity function is not only to constrain its form, but to provide information on the underlying distributions which cause it to take that form. In Chapter 2 it has been shown that the form of the luminosity function depends both on the initial mass function and the birthrate. Detailed simulations of the cool dwarf population can lead from these underlying distributions to simulated luminosity functions. These can then be compared to the observed luminosity function to gain information on the validity of the underlying distribution.

Here results for the SIPS survey, the survey of Cruz et al. (2003) and the upcoming UKIRT Infrared Deep Sky Survey (UKIDSS; Lawerence et al. 2006) are simulated. These are used to constrain underlying distributions or demonstrate the constraints that could be set once the survey is completed.

The basic simulation method employed here is similar to that used by Burgasser (2004). Individual objects are given ages drawn from a birthrate and masses drawn from a mass function. They are then given photometric (absolute magnitudes in each passband) and astrometric (space velocities, space positions) properties. Details of this are outlined in Sections 6.1 and 6.2 respectively. These are converted into the observables useful in a survey: sky position, proper motion, apparent magnitudes in each passband. These observables have a modelled error added to them. Finally they are passed to the survey selection mechanism. The selection mechanism picks out

objects which fall into the area of sky the survey covers, fall into the correct colour space, are brighter than the survey's limiting magnitude and which have proper motions that fall into the region the survey is examining. Thus only objects which would be selected by the real survey contribute to the simulated sample. The simulated sample can then be plotted as a function of colour, proper motion or any observable that needs to be demonstrated.

The definitions of the forms of the birthrate and mass function used in these simulations can be found in Chapter 2. These are the log–normal mass function (see Equation 2.5), the power law mass function (Equation 2.4), the constant birthrate and the exponential birthrate (Equation 2.29). The objects have ages up to 10Gyrs, similar to the age of the Galactic disk found by Knox et al. (1999) and masses ranging from the upper limit of the models used ($0.5M_{\odot}$ for the simulations of the SIPS survey and $0.1M_{\odot}$ for the UKIDSS/Cruz simulations) to lower limits either defined by the lower limits of the models used ($0.003M_{\odot}$ for the UKIDSS/Cruz simulations) or set higher to increase the efficiency of the simulations ($0.003M_{\odot}$ for SIPS).

Where the number of objects potentially detected by a survey is desired, the simulations are anchored at 0.0055 objects per cubic parsec in the mass interval $0.1-0.09M_{\odot}$. This is the same normalisation as Burgasser (2004) uses and is calculated from the results of Chabrier (2001) and Reid et al. (2002).

6.1 Astrometric Simulation

In order to effectively model the positions and proper motions of the synthetic stellar population, their cartesian positions and space velocities must first be considered. Heliocentric Galactic cartesian coordinates out to some maximum distance are generated. The maximum distance is always greater than the furthest object that could be detected by the survey. In the coordinate system x and y lie in the Galactic plane while z is perpendicular to the plane. These have velocities U, V and W associated with them. The x and y positions are randomly generated from a flat distribution while the z position is generated from an exponential distribution with scale height z_0. It is well established that the older populations have larger scale heights, hence this age dependency must incorporated into the model. It is also clear that due to disk heating

a population's velocity dispersion increases with age, and this is taken into account by making the scale height age dependent. Hence, the space positions and velocities are generated based on the age of the object. This is demonstrated in Figures 6.1, 6.2 and 6.3. Figure 6.1 shows a simulated stellar population with a constant birthrate and ages ranging from 5-10 Gyr. Conversely Figure 6.2 shows a simulated stellar population with a constant birthrate and ages ranging from 0-5 Gyr. The effect of the evolution of the scale height can be seen in the bottom right panel (which shows the distance from the Galactic Plane) of both with the younger population having a distribution more strongly peaked around zero (i.e. close to the Galactic Plane). The other three panels indicated that the velocity dispersions are all much higher for the older population. Finally Figure 6.3 shows the effect of combining these two different populations.

From these the sky positions, distance and proper motions are calculated. Any object whose angular position falls within the survey area passes the positional survey selection mechanism.

6.2 Photometric Simulation

In this section, evolutionary models from Baraffe et al. (2003) and Baraffe et al. (1998) are utilised to provide look-up tables of quantities such as $T_{\rm eff}$ and absolute magnitudes in a given passband, versus mass and age. Data from Baraffe et al. (1998) are used only for objects more massive than $0.1 M_{\odot}$ and solely in the simulations of my own infrared proper motion survey. While it is true that using one set of (dust settled) models across the L–T divide may produce errors in the effective temperatures of objects (as the temperature scale for L dwarfs may be affected by dust opacity), Burgasser (2004) notes that such an error introduced by this method is less than 10%.

In order to properly model the results of the infrared surveys an empirical effective temperature versus bolometric correction relation must be utilised. This allows the simulations to be grounded not only on theoretical models, but on real data. The results of three surveys will be simulated; my own infrared proper motion survey (Deacon & Hambly, 2004), the survey of Cruz et al. (2003) for L dwarfs using 2MASS and the UK Infrared Deep Sky Surveys (Lawerence et al., 2006). The photometric simulations for the UKIDSS survey were carried out first. Hewett et al. (2006) calculated the colours in

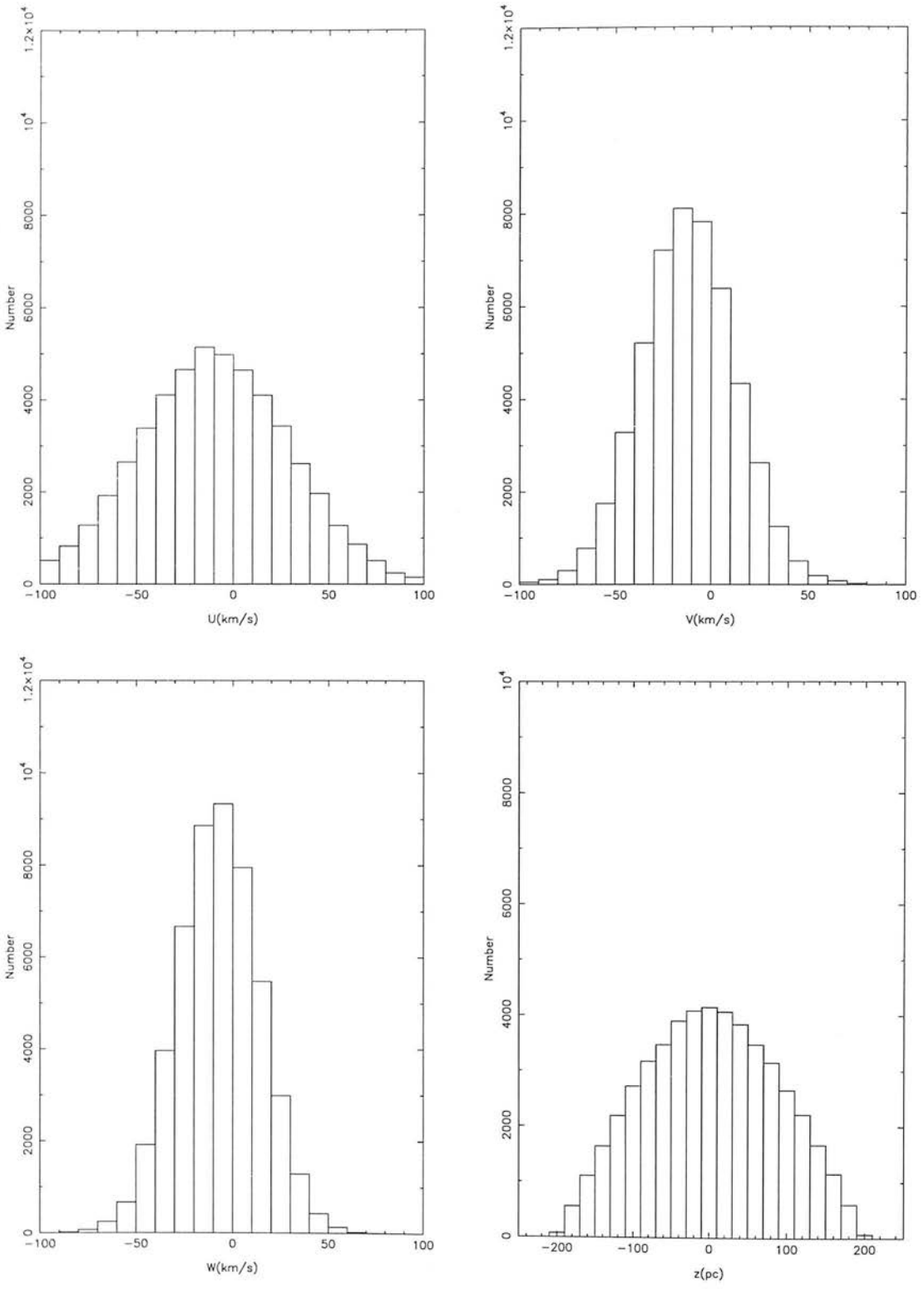

Figure 6.1: The simulated space velocities and position perpendicular to the Galactic Disk for 50,000 objects with ages ranging from 5-10 Gyr.

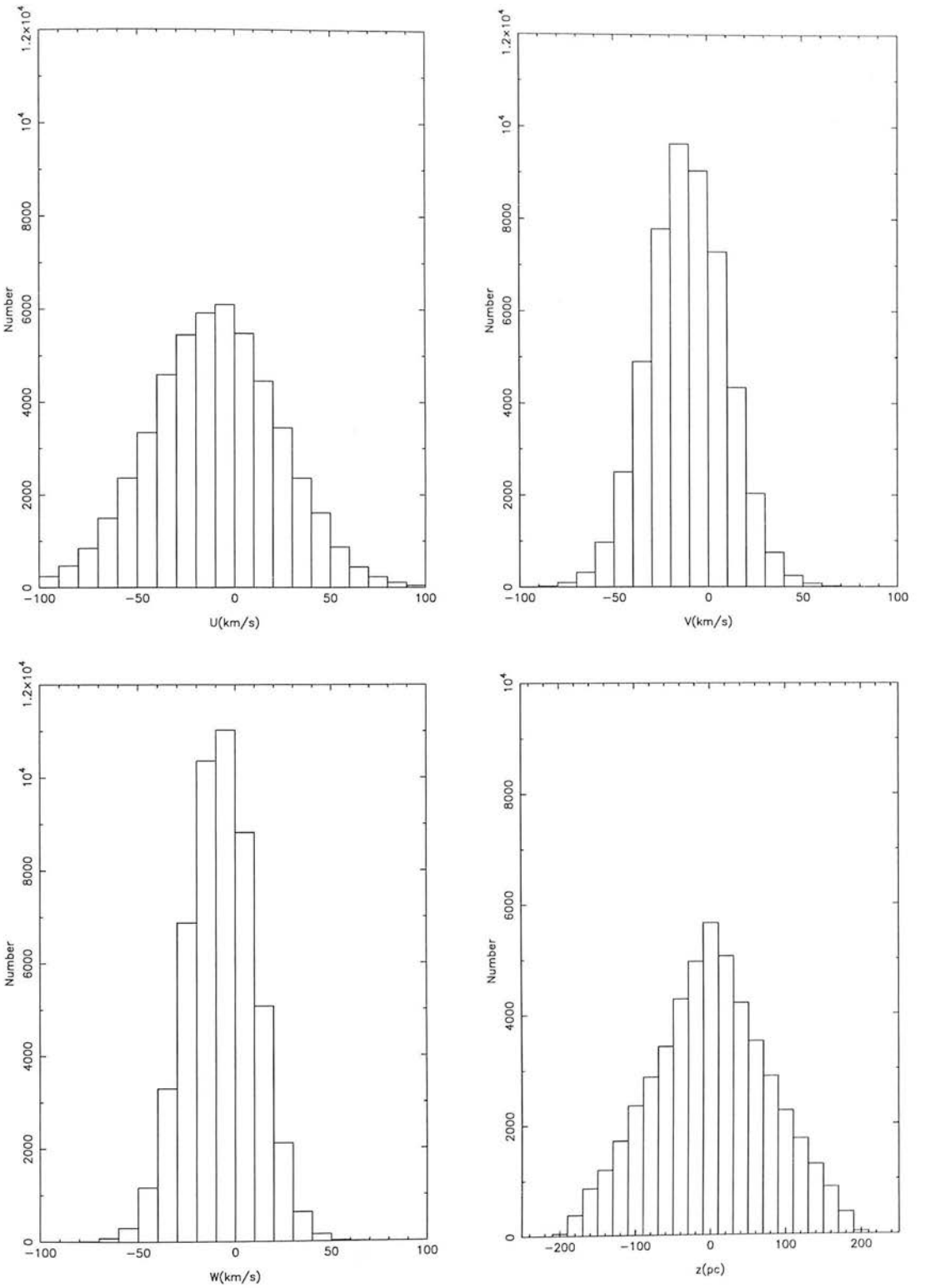

Figure 6.2: The simulated space velocities and position perpendicular to the Galactic Disk for 50,000 objects with ages ranging from 0-5 Gyr.

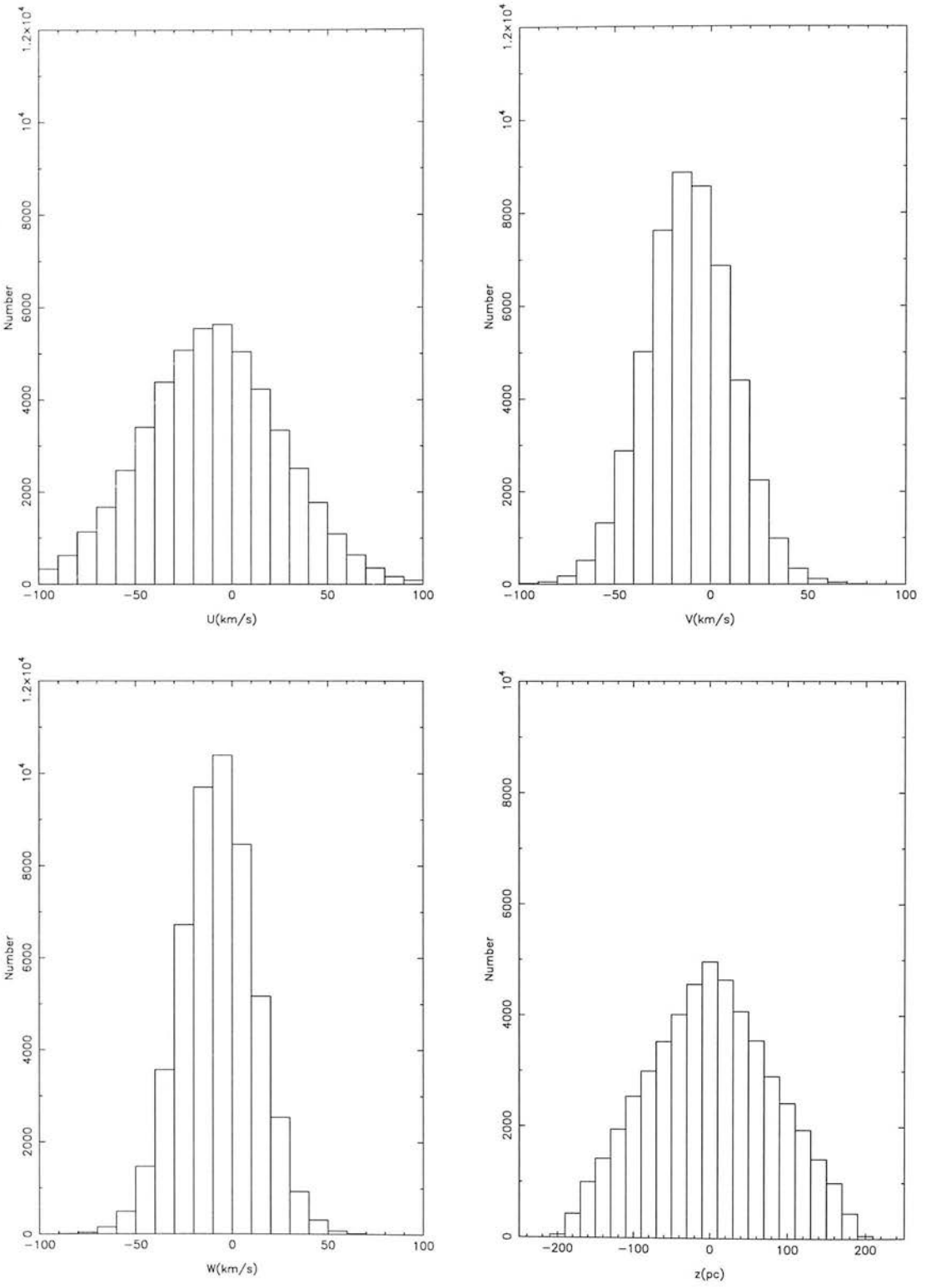

Figure 6.3: The simulated space velocities and position perpendicular to the Galactic Disk for 50,000 objects with ages ranging from 0-10 Gyr.

both the MKO (Simons & Tokunaga 2002 and Tokunaga et al. 2002) used by UKIDSS of a series of ultra–cool objects from their spectra. These were combined with absolute J magnitudes (converted into the MKO system) along with absolute and effective temperatures from Vrba et al. (2004) and bolometric magnitudes from Golimowski et al. (2004). Two separate polynomials in each passband were then calculated, one for the T regime and one for the M & L regime. These are shown in Figure 6.4 along with the data points. The purpose of the two separate polynomials is to model the photometric discontinuity across the L–T boundary. When it came to simulating the Cruz et al. (2003) luminosity function a simple conversion was made to 2MASS (Skrutskie et al., 2006) passbands using relations given in Hewett et al. (2006). The results of both of these sets of simulations were published in Deacon & Hambly (2006). During the refereeing process for this paper it was noted by the referee (Sandy Leggett) that it would be more sensible to use both the effective temperatures and absolute bolometric magnitudes from Golimowski et al. (2004). Hence these have been used for the simulation of SIPS. Four early M dwarfs from Berriman & Reid (1987) were added to the objects in Golimowski et al. (2004)'s sample. Both papers contained measures of each object's distance as well as absolute bolometric magnitudes and temperatures. The magnitudes of the objects in each passband came from a variety of sources. The I data for the M dwarfs came from the SuperCOSMOS Sky Survey (Hambly et al., 2001a). For the L and T dwarfs the I magnitude came from Dahn et al. (2002) [1]. However the lack of I data for T dwarfs mean that they cannot be included in these simulations (the I data is essential for calculating simulated $I-J$ histograms). All the remaining objects in this sample had their J, H and K_s magnitudes extracted from the 2MASS survey (Skrutskie et al., 2006). The observed magnitudes were then converted to absolute magnitudes and used to find bolometric corrections. For the SIPS simulations the R magnitudes were taken directly from the Baraffe et al. (1998) models.

Each object is given an age and a mass from the birthrate and mass function. The object's effective temperature and a bolometric magnitude are then found from the evolutionary models. The temperature is then used to calculate the bolometric corrections (and hence infrared magnitudes) for each simulated object. In the simulations for

[1] It is assumed that the I_c magnitudes of Dahn et al. (2002) will be similar to their I_N magnitudes. This assumption is supported by filter profiles and colour transformations given in Bessell (1986)

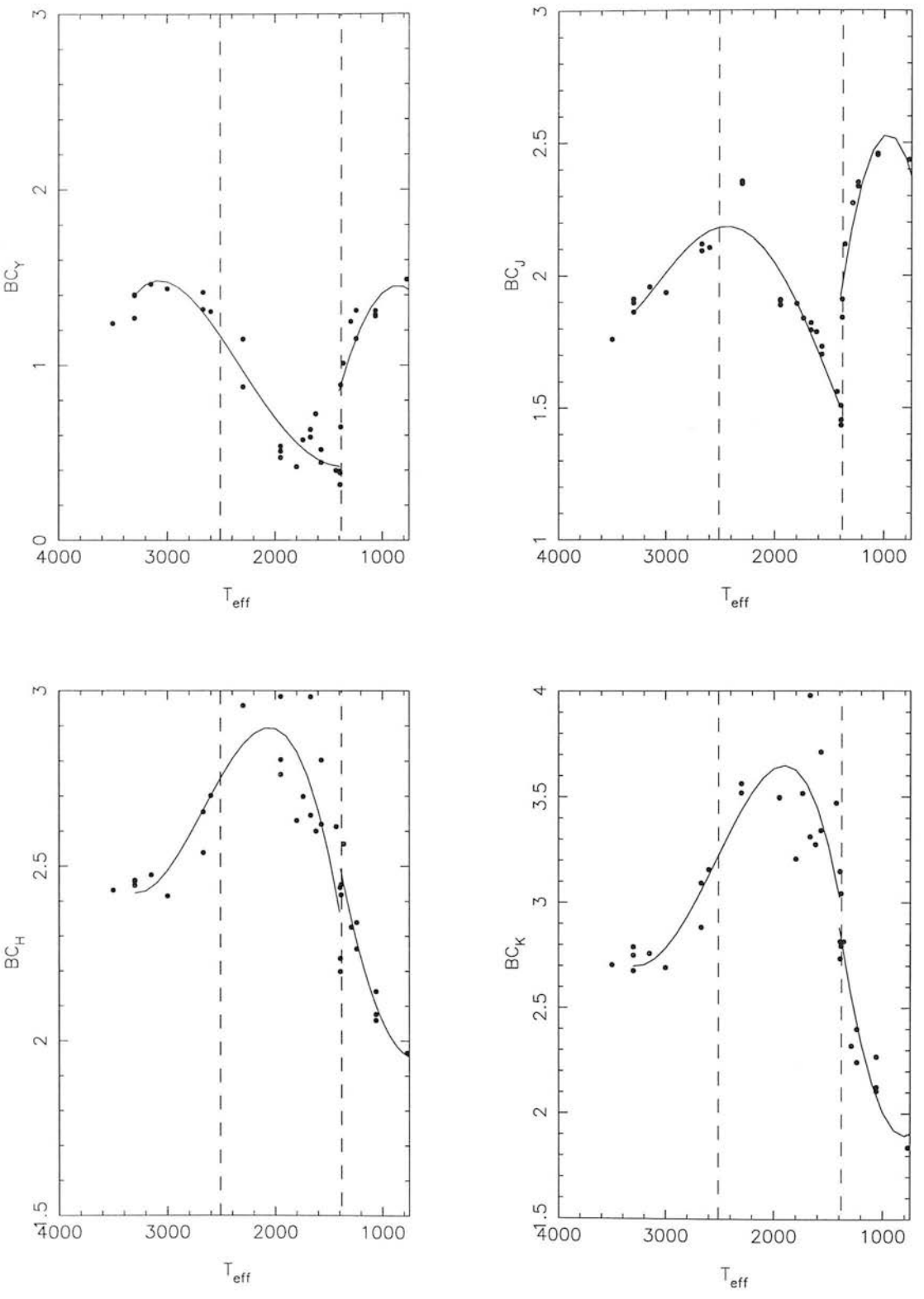

Figure 6.4: The polynomial fits for bolometric correction - effective temperature relations. Each passband modelled is shown in a separate panel (including the Y band Hewett et al. 2006). Note that the vertical dotted lines mark out the boundaries between the spectral types with T lying below 1400K, L in the region from 1400-2500K and M warmer than 2500K. These temperature boundaries come from Vrba et al. (2004)

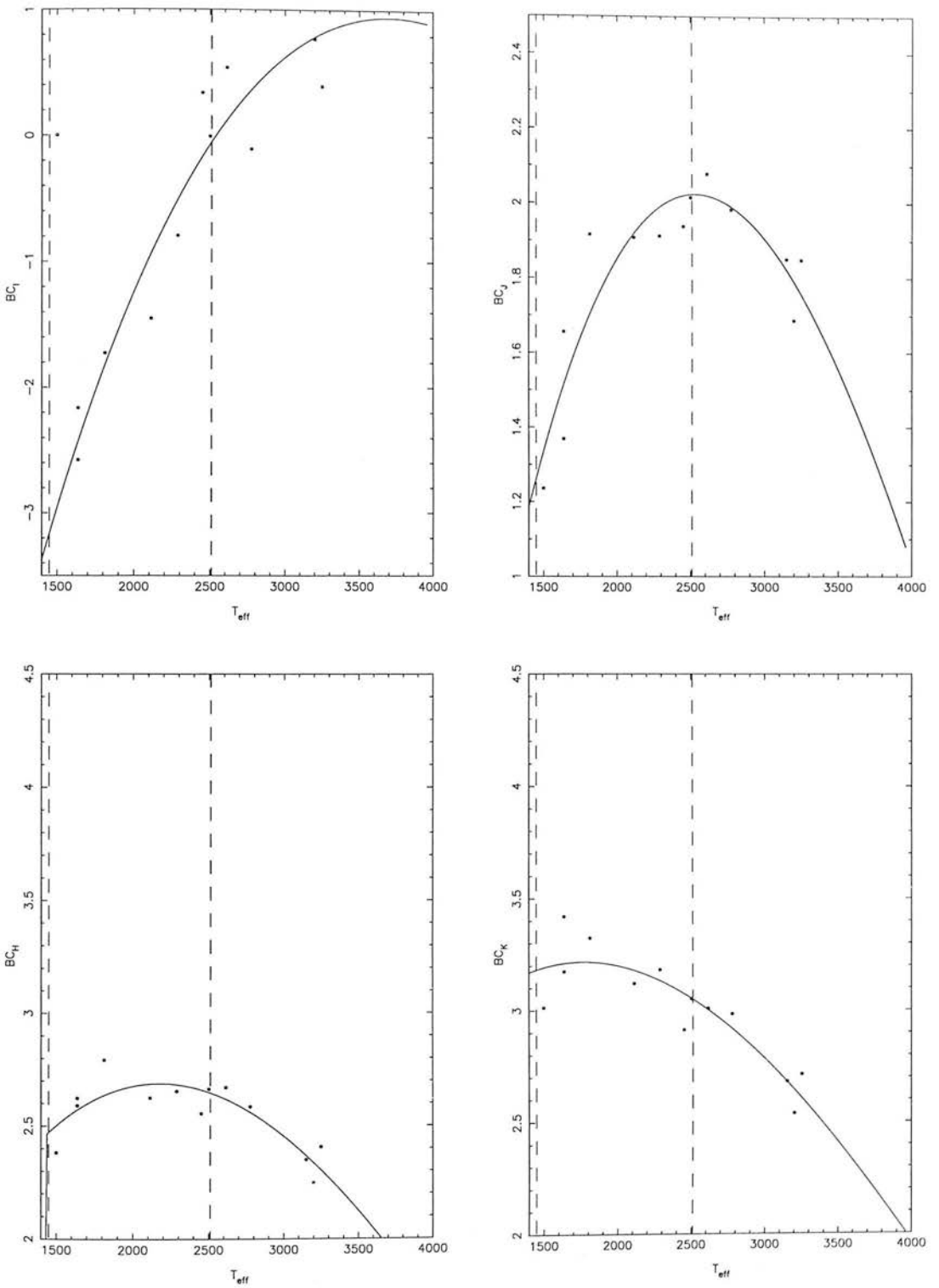

Figure 6.5: The polynomial fits for bolometric correction - effective temperature relations. Each passband modelled is shown in a separate panel. Note that the vertical dotted lines mark out the boundaries between the spectral types with T lying below 1400K, L in the region from 1400-2500K and M warmer than 2500K. These temperature boundaries come from Vrba et al. (2004)

the UKIDSS surveys objects cooler than $T_{\rm eff} = 770$ K have no observational data on which to base bolometric corrections so the magnitudes predicted by the models must be used.

6.3 Effective Temperature Distributions

The forms of the underlying mass function and birthrate will obviously affect a luminosity function and hence the results of a survey. This is demonstrated in Figures 6.6 and 6.7, showing the L, T and Y regions. These show the effect altering the mass function and birthrate will have on the effective temperature distribution (and hence the luminosity function and survey results). In Figure 6.6 the more negative the value of the exponent α, the fewer low mass objects, and hence fewer cool objects. The log–normal mass function and the flat mass function produce broadly similar results. The main effect of altering the birthrate (as demonstrated in Figure 6.7) is to change the depth of the trough around 1700K. The higher the birthrate in the past, i.e. lower positive values of the scale–time τ, the deeper the trough. The shapes of the effective temperature distributions are similar to those found by Burgasser (2004). Note that Allen et al. (2003) find a more complicated series of peaks and troughs. This is because their simulations are for young, single–age clusters where the luminosity evolution pause caused by Deuterium burning will significantly affect the distribution.

6.4 Constraining Underlying Distributions

In the previous section it has been shown that underlying distributions affect the effective temperature distribution for Low Mass Stars and Brown Dwarfs (and hence the results of surveys looking for them). Clearly, the reverse is also true, and the results of surveys can be used to constrain the underlying birthrate and IMF. For example, suppose that the IMF (in the range $0.1 - 0.003 M_{\odot}$) and birthrate have the following functional forms:

$$\begin{aligned} b(t) &\propto e^{-\beta t}, \\ \xi &\propto m^{-\alpha}, \end{aligned} \tag{6.1}$$

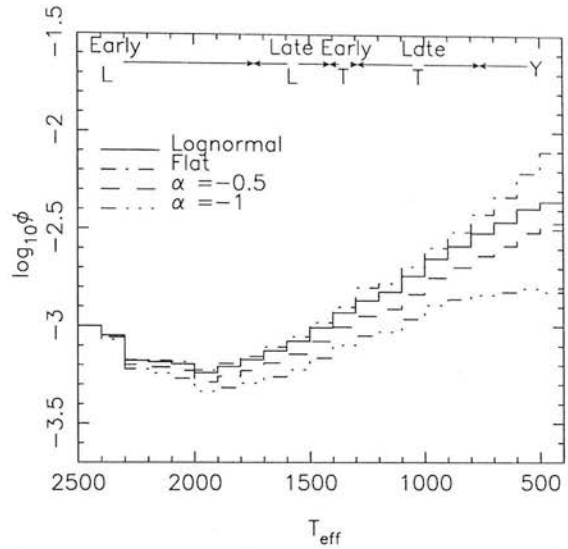

Figure 6.6: The alteration to the effective temperature distribution caused by different underlying IMFs. In this case a constant birthrate is used and the simulations are all normalised to the same point in the hottest bin. Note that the main effect is the height of the second peak. The temperature regions corresponding to each spectral type are taken from Vrba et al. (2004).

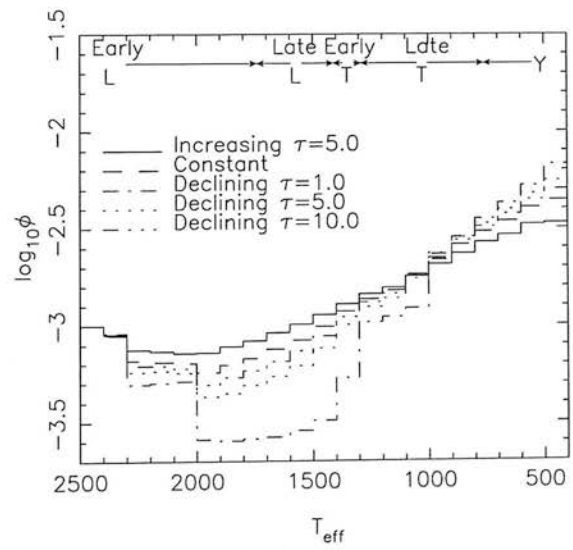

Figure 6.7: The alteration to the effective temperature distribution caused by different underlying birthrates. In this case a log–normal IMF is used and again the simulations are all normalised to the same point in the hottest bin. Note that the main effect is the depth of the trough. Again the temperature regions corresponding to each spectral type are taken from Vrba et al. (2004).

where a positive value of β implies a declining birthrate. A grid of colour distributions with values of α and β can now be simulated. Then the observed colour distribution can be compared to this grid. A multiplication factor γ is then used to vary the total number of objects for each colour distribution. The values of χ^2 for a range of values of γ are calculated for each value of α and β. Hence a value of χ^2 is found for each value of γ and for each colour histogram (and hence for each value of α and β). This distribution is then marginalised over γ such that

$$p(\alpha, \beta) = \frac{\int e^{-\chi^2/2} d\gamma}{\int\int\int e^{-\chi^2/2} d\gamma d\alpha d\beta}. \tag{6.2}$$

This procedure produces a probability distribution over α and β. Marginalising this further will produce distributions solely over α or β.

In some cases the initial grid will be too coarse to produce meaningful measures of the underlying parameters. Once the area of maximum probability in this initial coarse grid is identified a second, finer grid centred around this region is simulated. This has ten times the resolution in α and five times the resolution in β. In order to glean information on the errors on each parameter the probability distribution is marginalised over α to produce a distribution in β and vice-versa. The mean value of each parameter along with their standard deviations can then be calculated.

6.5 Results of Simulations

6.5.1 SIPS constraints

The results of the SIPS survey in the range $0.1 < \mu < 0.5$ were simulated as outlined earlier. The simulation grid had a range in α of $-2.0 < \alpha < 2.0$ and in β of $-0.2 < \beta < 0.2$. In addition to the standard survey selection parameters the incompleteness caused by background crowding calculated in Section 4.4.3 was also included. The constraints set are shown in Table 6.1. The fitting procedure allows information on the number density to be extracted from the multiplication parameter γ. The probability surface for these results can be found in Figure 6.8 and the probability distribution over each individual parameter is shown in Figure 6.9. Clearly from these results the constraint set on α must be regarded as sensible as the probability is constrained to a region of the surface. Conversely the fit in β has a wide spread of probability, nowhere

Table 6.1: The calculated values for α, β and the number density of objects in the mass range $0.09M_{\odot} < m < 0.1M_{\odot}$.

Parameter	Value
α	0.66 ± 0.21
β	-0.01 ± 0.10
Number Density	0.0053 ± 0.0002

near a gaussian distribution. Hence this constraint must be treated with caution. The calculated value of β does seem to agree with the conclusions of Burgasser (2004) that a declining birthrate with a scale time of 5Gyrs (β=0.2) is not supported by observations. In the case of the number density in the range $0.09M_{\odot} < m < 0.1M_{\odot}$ the probability distribution is a near perfect gaussian. The value of 0.0053 ± 0.0002 is also in good agreement with the value of 0.0055 ± 0.0018 found by Burgasser (2004) from the work of Chabrier (2001) and Reid et al. (2002). The error on this value appears small but it should be noted that the model does not include more complicated parameters such as binarity. Note that due to the relatively noisy appearance of the probability surface (Figure 6.8) it was decided not produce a finer simulation grid.

Figure 6.10 provides a visual representation of the best fit simulation and the true survey results. It is clear that while the model is not perfect it is a reasonable fit to the data. The reduced χ^2 (χ^2_ν) comparing this model with the data has a value of 1.4. This is just outside the one σ error bound on χ^2_ν.

Potential errors from photometric offsets

Figure 6.5 shows the bolometric correction - effective temperature fits in different pass-bands. The I band fit is obviously much poorer than the others as it is based on photographic plate data which has larger errors than data from the 2MASS survey. As the measured parameters are based on simulated $(I - J)$ distributions any offset from the fit in the I band will cause an offset in the parameters. To quantify this error a series of simulations were produced with offsets in I ranging from -0.1 to 0.1. These were then compared to the grid with no I offset and probability distributions produced for each offset value. As all values of the offset are not equally likely each probability

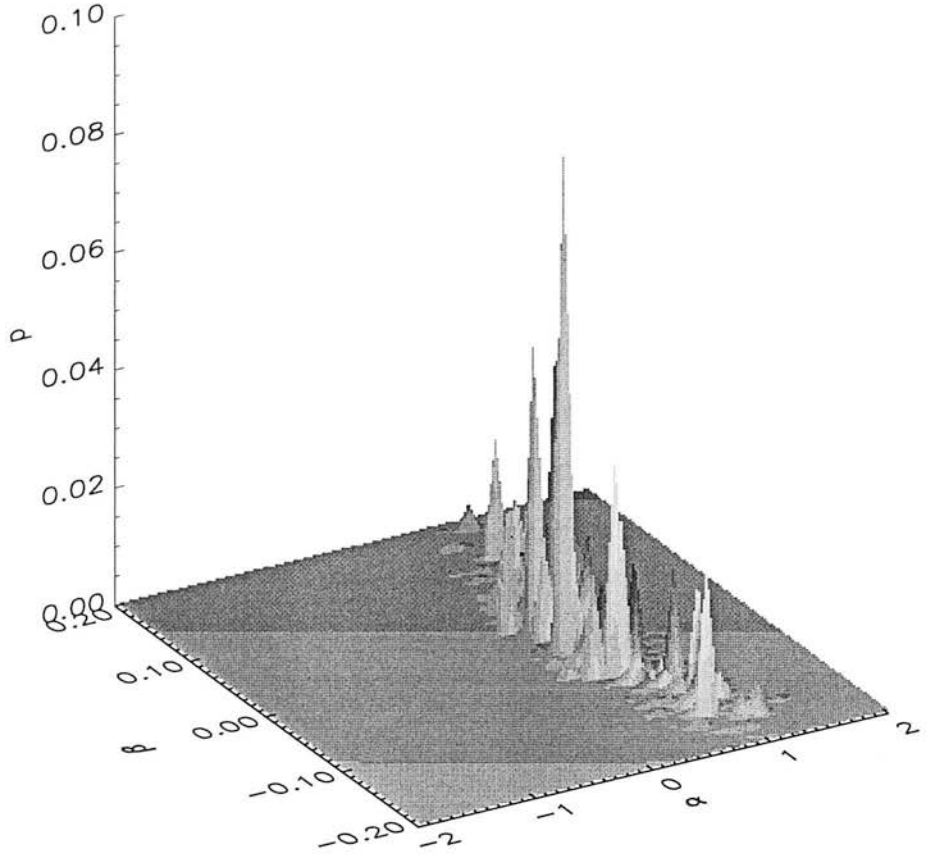

Figure 6.8: The probability surface produced by comparing the SIPS data with a grid of simulations. Note the apparent good constraint on α and the relatively loose constraint on β.

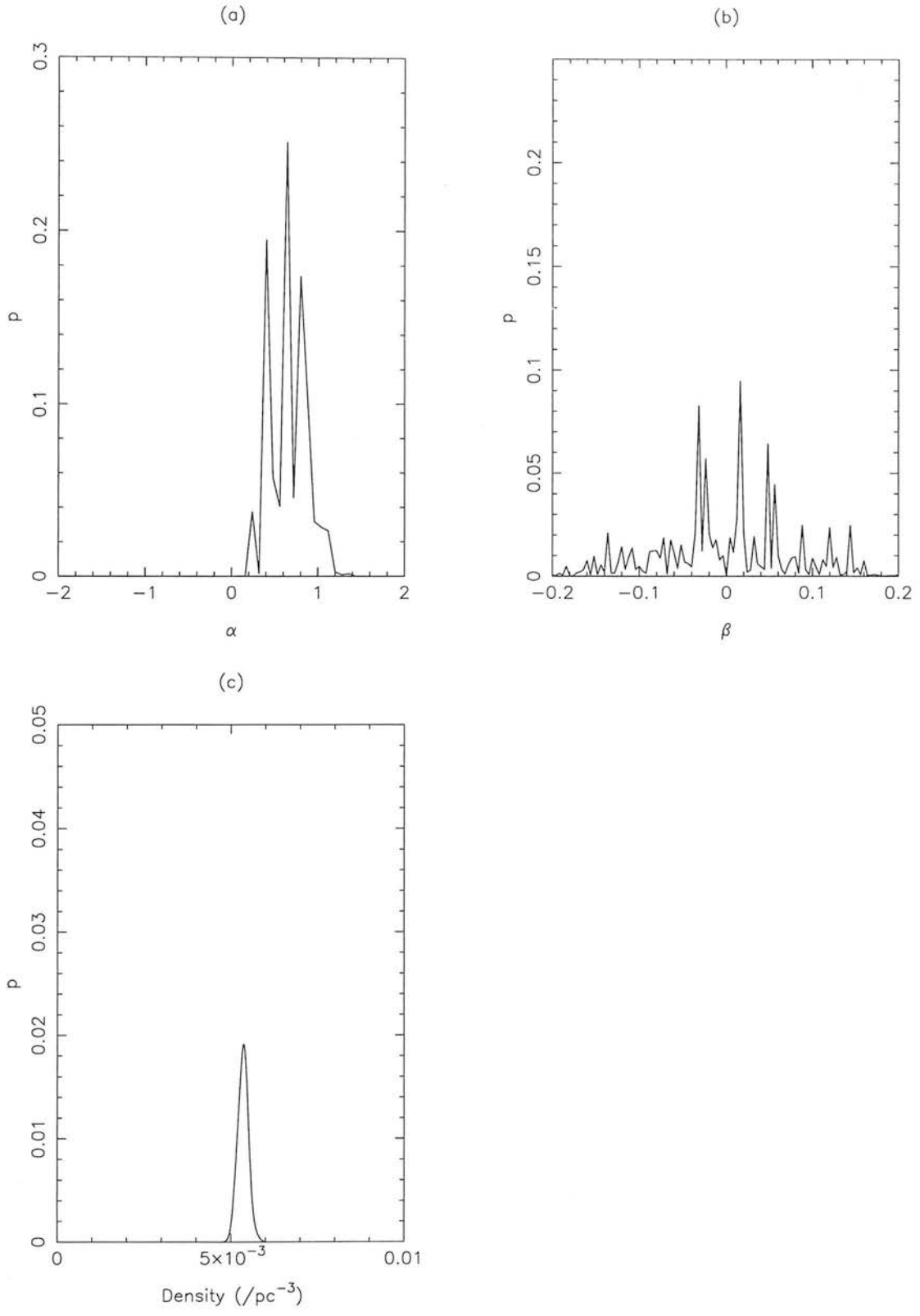

Figure 6.9: (a) The constraint that can be set on the mass function parameter α. Note the roughly gaussian shape. (b) The constraints that can be set on the birthrate parameter β. The virtually random positions of the peaks shows this is largely just noise and cannot be considered a solid constraint. (c) The constraint that can be set on the number density of objects with masses in the range $0.09M_{\odot} < m < 0.1M_{\odot}$. Note the roughly Gaussian shape.

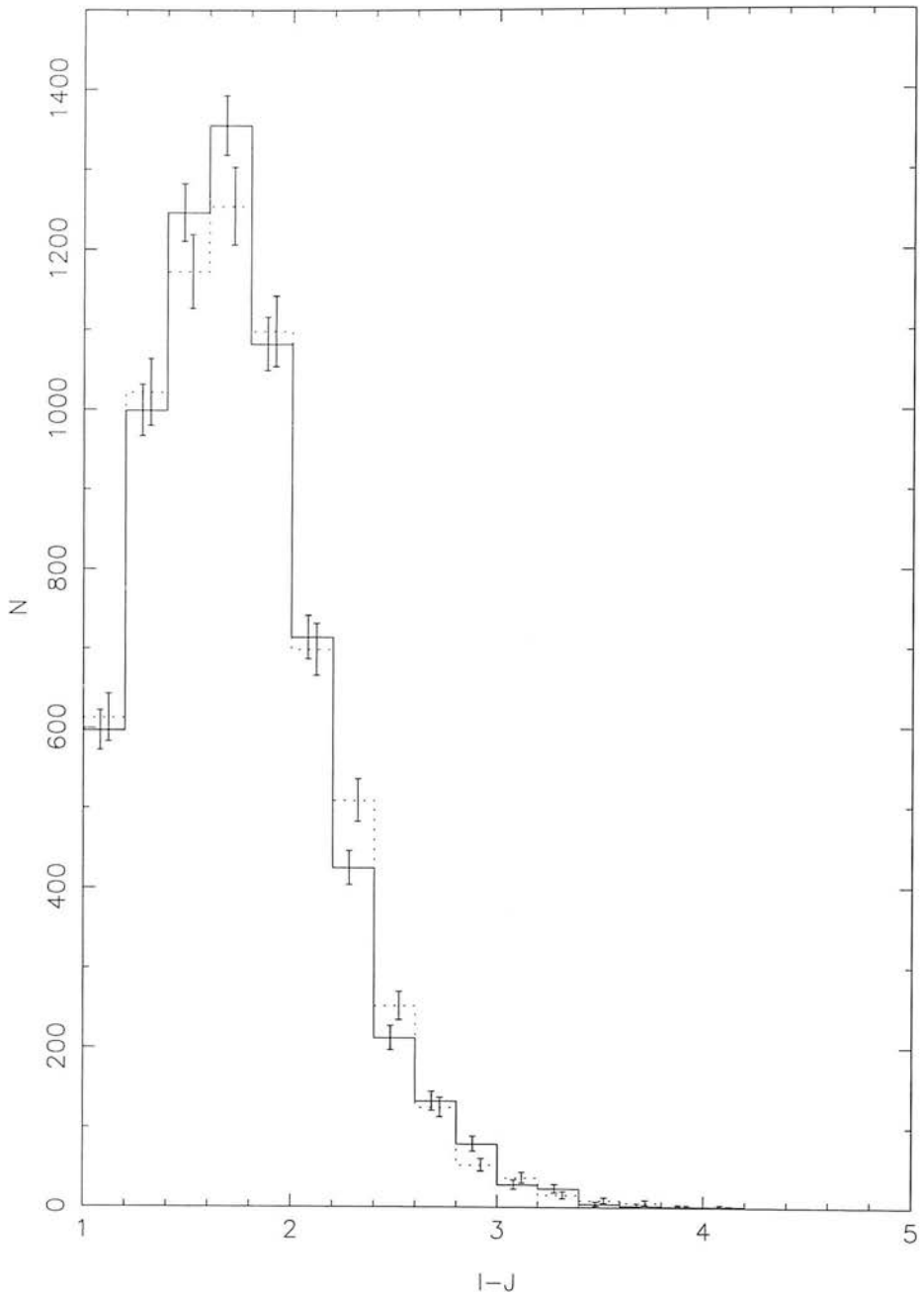

Figure 6.10: Comparing the observed SIPS $I - J$ distribution (solid line) with the simulated distribution for the best fit parameters (dotted line).

distribution was multiplied by the probability of the offset value. A simple gaussian with a standard deviation of 0.13 [2] (the error calculated from the covariance matrix of the fit) was used to model the probability of each offset. Finally the probability distributions were combined and marginalised over the I offset to yield values for the parameters and their errors. The parameter errors for a simulation with no I offset were also found. These were then subtracted (in quadrature) from the total error to unveil the error caused solely by an offset in the photometry. The errors in β and the number density were found to be much smaller than the errors quoted for these parameters. However the error on the value of α caused solely by this offset is 0.39, almost twice the previously calculated formal error. Hence this must be added to the previous error of 0.21, making the value of α 0.66 ± 0.44.

Comparison of the value of α with other results

Before the value of α can be compared to other results the range over which this value can be considered applicable must be decided. As there are so few objects redder than $(I--J)$=3 (see Section 4.4.1) it cannot be claimed that the survey significantly samples objects which the Baraffe models have as being redder than this. Hence a lower mass limit of $0.075M_{\odot}$, the mass of an (I–J)=3 object at an age of 7Gyr. There are two colour cuts which could define the upper boundary, the cut in $R-I$ and the cut in $I-J$. As the $R-I$ cut does not apply to all objects (only those which are paired by the SuperCOSMOS software) and it depends on two photographic datasets it cannot be considered a hard cut-off point. The $I-J$ cut on the other hand does apply to all objects and only depends on one set of photographic plate photometry, hence it can be considered a more obvious cut-off point. Objects with $(I-J) > 1.0$ tend to have masses below $0.2M_{\odot}$, hence this is set as the upper bound for which the calculated value of α can be considered valid.

The value of the parameter α can be easily compared to other studies using an α plot. Figure 6.11 shows such a diagram. Clearly the value calculated here fits into the general trend of results including the lognormal fit of Chabrier (2003a). It is also less

[2]The range simulated over is smaller than the value of σ, this may appear strange. However when the magnitude of the offset was more than 0.1 the values of the χ^2 statistic became so high it was clear that the model was not a useful fit to the data.

than one σ away from the result with the most comparable mass range, that of Kroupa (2001).

6.5.2 Constraints from the Cruz et al. (2003) Luminosity Function

In order to compare the constraints set by the SIPS survey with those set by others it was decided to simulate the J band luminosity function of Cruz et al. (2003), covering the L dwarf regime. A grid was simulated in the same manner as for the SIPS surveys with the appropriate cuts and limiting magnitudes quoted in Cruz et al. (2003). The bin centred on $M_J = 10.75$ as, although the maximum mass in this set of simulations of $0.1M_{\odot}$ equates to a stable main sequence absolute J magnitude of 10.2 (Baraffe et al., 2003), the scatter into this bin from brighter bins caused by photometric errors would not be modelled correctly. The two faintest bins were also excluded from the probability analysis as they are described as being incomplete (however they were simulated to correctly model scatter). Finally after going through the probability analysis, a secondary peak which appeared at the edge of the grid was excluded as it was at a very high value of α excluded by other studies. The resulting probability surface is shown in Figure 6.12. The measured values of the parameters were; $\alpha = 0.95 \pm 1.17$ (implying a Mass Function rising at lower masses) and $\beta = -0.134 \pm 0.173$. The question remains over what range of masses is this result valid. If we take $0.1M_{\odot}$ as a maximum mass then the minimum mass will by given by the mass of an object with $M_J = 14.0$ at an age of 10 Gyr, the maximum calculated in the Baraffe et al. (2003) models – this is found to be $\mathrm{m} = 0.072\mathrm{M}_{\odot}$. Hence the value of α covers the range $0.072M_{\odot} < \mathrm{m} < 0.1\mathrm{M}_{\odot}$. This result (albeit with a large error) is consistent with both Kroupa (2001), who measured a value in the range $0.08M_{\odot} < \mathrm{m} < 0.5\mathrm{M}_{\odot}$ of $\alpha = 0.3 \pm 0.5$, and with the Chabrier (2001) log–normal IMF peaking at $0.75M_{\odot}$. It differs by just over 1σ from the Allen et al. (2005) value of -0.7 ± 0.6. The value of β is consistent with a constant birthrate.

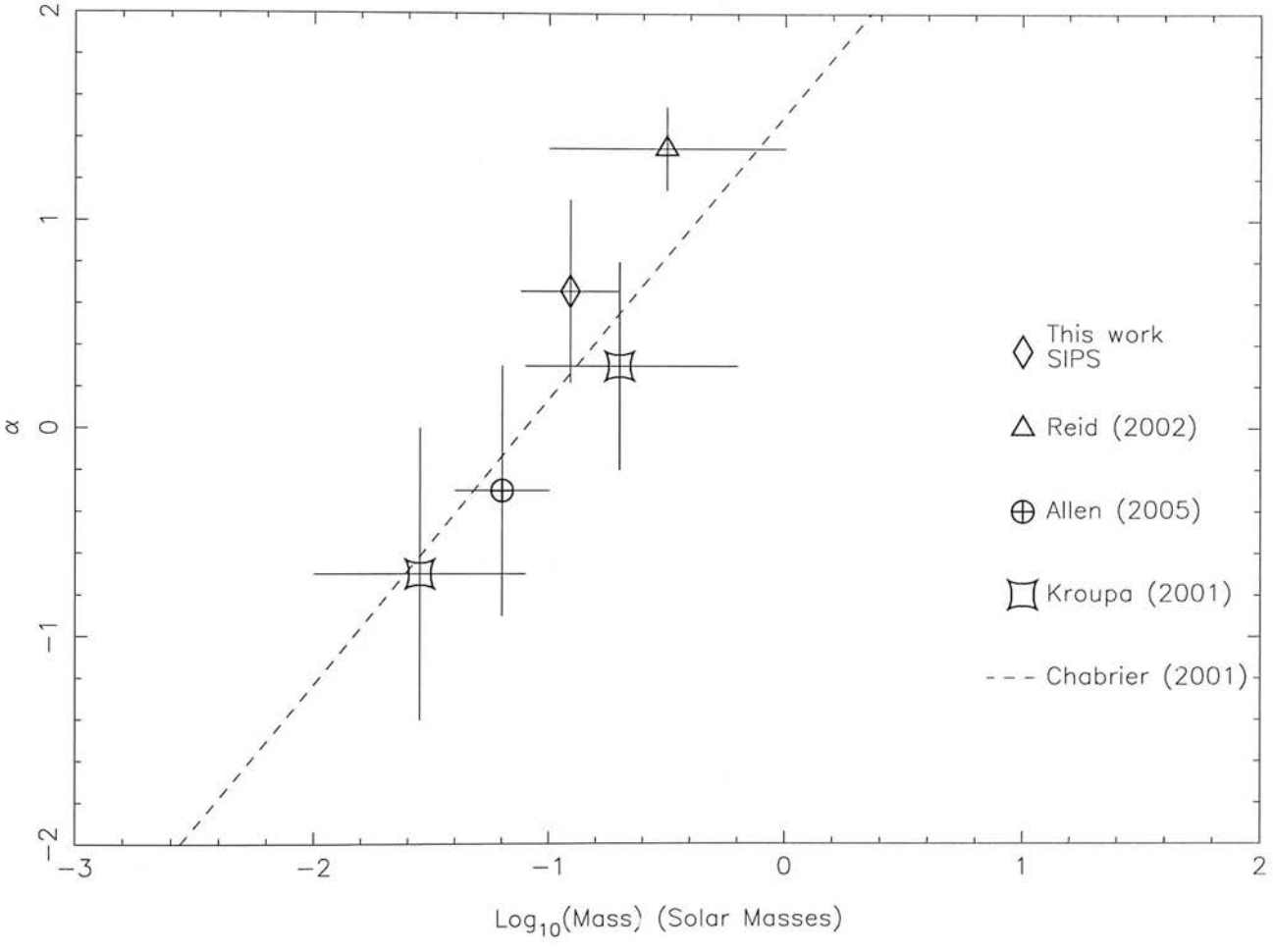

Figure 6.11: A plot showing the results of different studies of the mass function along with the result from SIPS. The values of α are shown along with their errors. The error bars in the x-axis represent a range in mass rather than an error. Only studies of the mass function in the field are shown here.

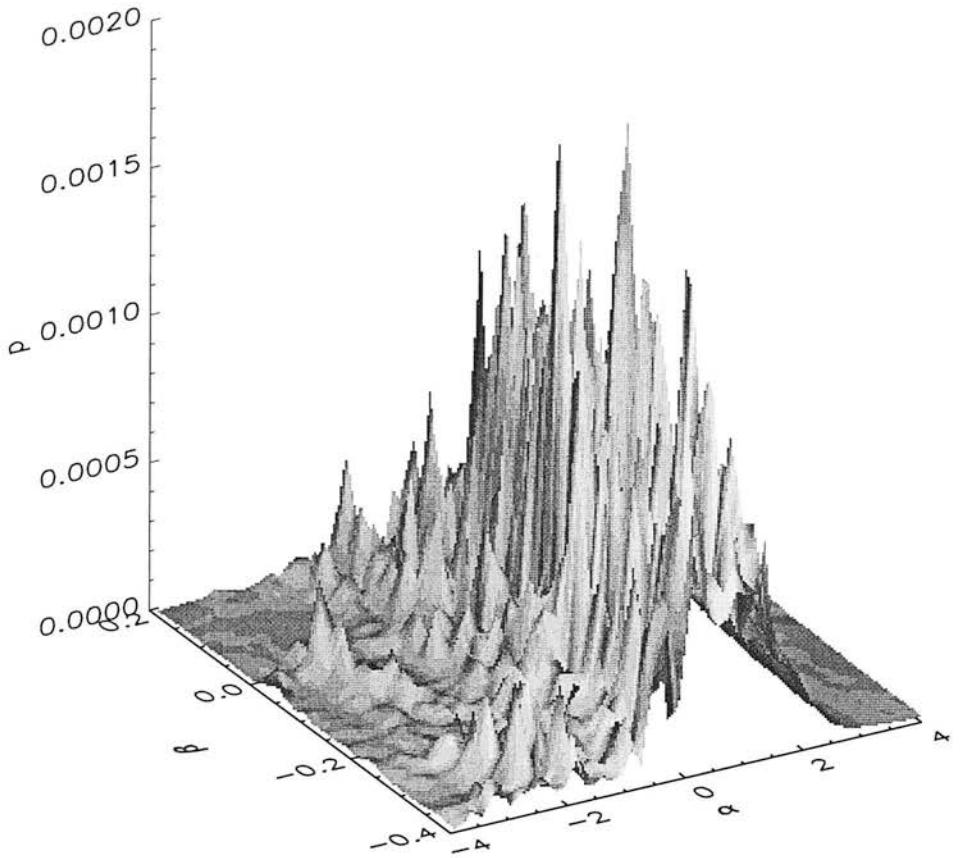

Figure 6.12: The probability surface found from the Luminosity Function of Cruz et al. (2003).

6.6 Future Surveys

6.6.1 The UKIRT Infrared Deep Sky Survey

Section 4.2 outlines the strides forward in the study of cool dwarfs which have been made possible by already completed infrared surveys. The next generation of infrared surveys will be undertaken with large format imagers such as WFCAM (Henry et al., 2003) and WIRCAM (Puget, 2004). WFCAM is a wide–field quasi Schmidt camera mounted at the Cassegrain focus of the UK Infrared Telescope (UKIRT). A quadruple detector array provides (with mosaiced observations) a field of view of 0.77 sq. degrees. The UKIRT Infrared Deep Sky Survey (UKIDSS; Lawerence et al. 2006) is employing WFCAM for a series of Galactic and extragalactic surveys, and two of these surveys are ideal for the detection of ultra–cool dwarfs in the field. The Large Area Survey (LAS) is a wide–field, high latitude survey in Y (Hewett et al., 2006) and JHK in the MKO system (Tokunaga et al. 2002; Simons & Tokunaga 2002); the Ultra Deep Survey (UDS) is a deep, narrow–field survey in JHK. The initial two year program for the LAS will be 2000 square degrees to a depth of $J = 19.7$. The seven year plan will include a second J band epoch to allow proper motion measurements and will cover 4000 square degrees to a depth of $J = 20$. The UDS will cover 0.77 sq. degrees in both the two and seven year plans. In the two year plan only J and K will be observed to a depth of $J = 24.0$, while the full seven year plan also includes H and will go one magnitude fainter in J. The number of objects of different effective temperatures and colours found in these surveys can provide information on the IMF (e.g. Pinfield et al. 2006) and birthrate.

Simulated results of the UKIDSS LAS survey

The LAS is designed to search for ultra–cool dwarfs, high redshift quasars and cool subdwarfs. It uses J, H and K in addition to the Y filter (Hewett et al., 2006). The Y filter lies in between the I and J bands, is centred around one micron and is slightly redder than the Z filter. It is specifically designed for the study of ultra–cool dwarfs and quasars. It will provide a band to allow M, L, T and Y dwarfs to be distinguished both from each other and from hotter main sequence stars. Additionally

SDSS (Adelman-McCarthy & et al., 2006) photometry can be used to remove quasars from the sample (Hewett et al., 2006). The final survey will cover an area around the northern Galactic pole as well as a small strip in the south Galactic cap. Both areas are scanned by the Sloan Digital Sky Survey (SDSS, Adelman-McCarthy & et al. 2006) allowing additional optical photometry to be utilised. The full seven year survey will go to depths of $Y = 20.5$, $J = 20.0$, $H = 18.8$ and $K = 18.4$ (detection in K was not required in the survey selection mechanism as many cooler objects have their luminosity severely reduced in this band due to methane and water absorption) with an additional second scan in J to allow proper motion measurements.

Simulations of the full seven year LAS area were carried out as described earlier in this chapter. Figure 4.7 shows the simulated proper motion histograms for objects of different spectral types. Notice that later spectral types' histograms peak at higher proper motions. This is simply a selection effect as cooler objects will only be observable nearby, where they will typically have large proper motions[3].

The expected numbers of detected objects of different spectral types are shown in Table 6.2. Figure 6.14 shows the effect on the $(J-H)_{MKO}$ colour[4] histogram of altering the IMF. The sharp drop at $(J-H)_{MKO} = 0.4$ is due to objects bluer than this divide being mid T dwarfs and objects redder than this being (on the whole) the much more easily detectable early L dwarfs. It is clear that for more steeply declining IMFs fewer T dwarfs are observed. Note that the log–normal and flat ($\alpha = 0$) IMFs produce very similar results. The effects of different birthrates are shown in Figure 6.15. Here, birthrates which produced more objects earlier in the Galaxy's history have fewer T dwarfs due to the cooling of brown dwarfs with time. The higher numbers of early L dwarfs in simulations with birthrates which were higher in the past is due to our normalisation and the way we have modelled scale height evolution. As the age of a population increases it becomes more spread out and hence the density in the Galactic plane drops. Since we are normalising in the local region (the Galactic plane) the number of objects here is kept constant. Hence as the population spreads the total number of objects increases. So if a particular class of object has enough mass for

[3]Here (as in all the LAS simulations) detection is only required in Y, J and H.

[4]The $J-H$ colour is used as a detection in K was not required and the predicted $Y-J$ magnitudes for T dwarfs are all very similar.

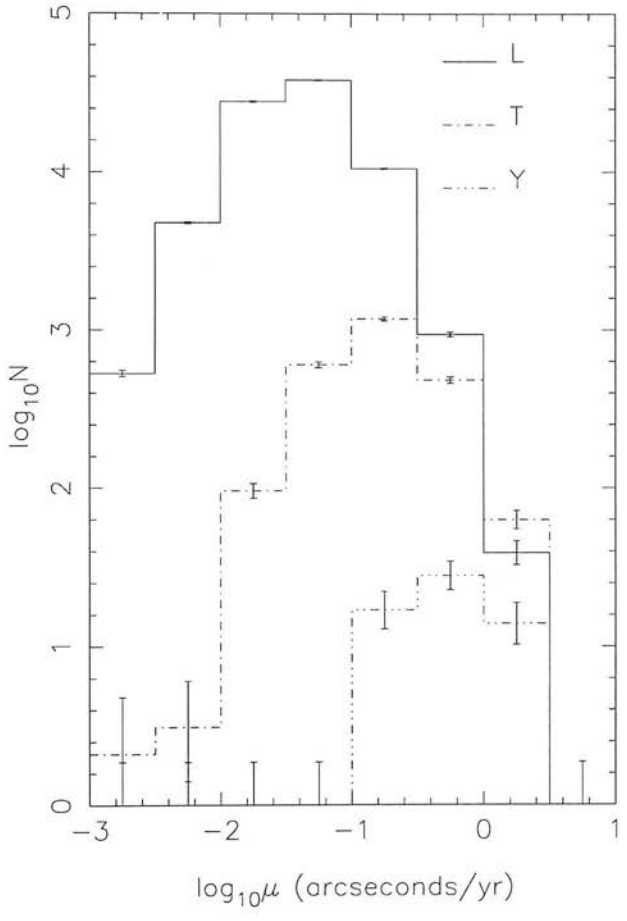

Figure 6.13: Proper motion histograms for objects of different spectral types in the seven year ($Y = 20.5$, $J = 20.0$, $H = 18.8$, $K = 18.4$ over 4000sq. degrees) UKIDSS LAS assuming a log–normal IMF and a constant birthrate.

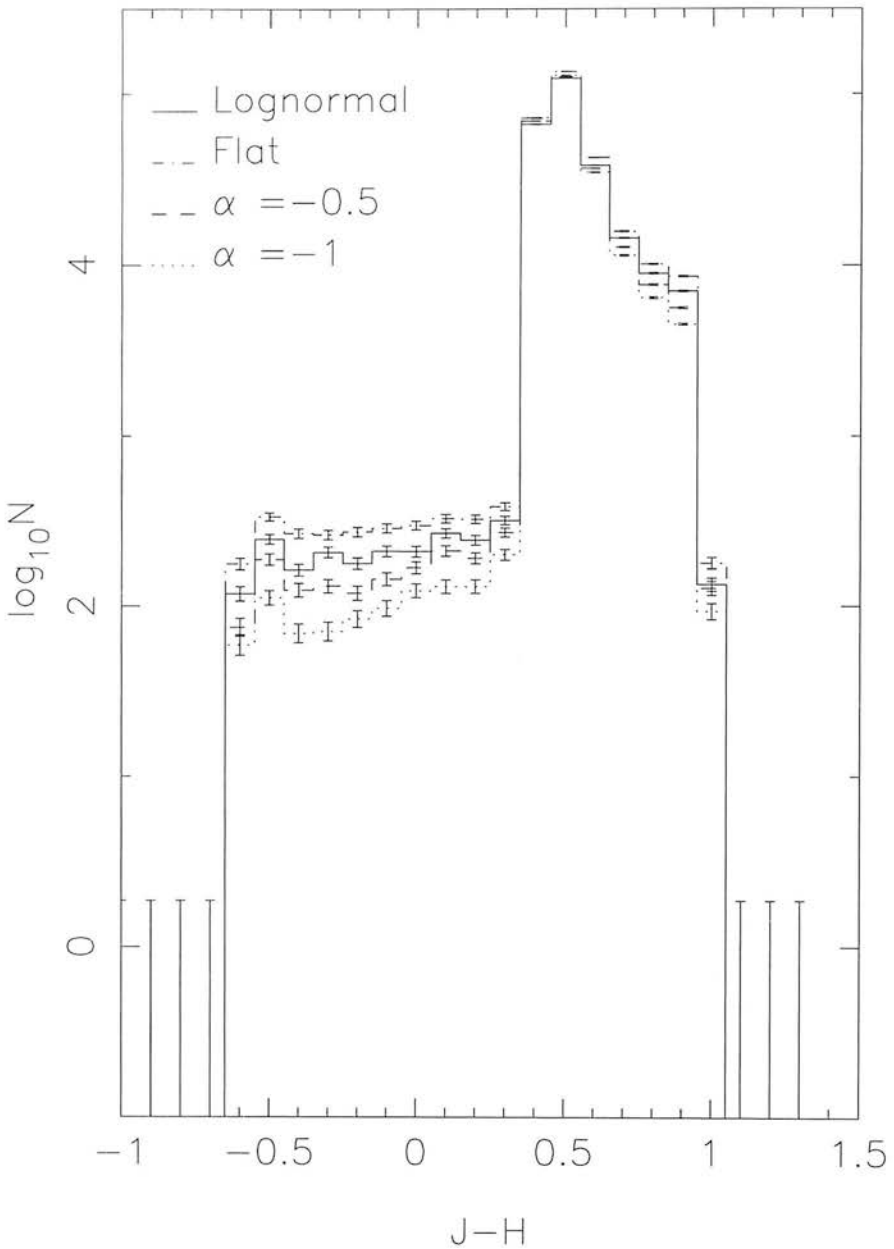

Figure 6.14: The alteration of the colour distribution caused by different Mass Functions. A constant birthrate is used here. Note the large step around $(J - H) = 0.4$. This marks the boundary between the Ys and mid-late Ts (to the left) and the L and early Ts (to the right). All J, H, and K magnitudes are in the MKO system (Tokunaga et al. 2002, Simons & Tokunaga 2002).

Table 6.2: The number of objects of different spectral types for varying birthrates and IMFs for the seven year UKIDSS LAS. Note that the τ = 1Gyr birthrate is included to illustrate the effect of a changing scale time. This should not considered to be a realistic distribution.

Mass Function	Birthrate	Early L Dwarfs	Late L Dwarfs	Early T Dwarfs	Late T Dwarfs	Y Dwarfs
Log–normal	Constant	77484	5620	968	1444	59
$\alpha = 0$	Constant	85182	6892	1235	2014	100
$\alpha = -0.5$	Constant	72476	4420	752	1060	39
$\alpha = -1$	Constant	67947	3479	513	676	25
Log–normal	$\tau = -5.0$	53559	8648	1375	1893	57
Log–normal	Constant	77484	5620	968	1444	59
Log–normal	$\tau = 10.0$	86296	4955	860	1276	42
Log–normal	$\tau = 5.0$	93316	4096	778	1173	46
Log–normal	$\tau = 1.0$	120515	1517	321	657	31

stable hydrogen burning, as early L dwarfs do, the number of detectable objects is increased by a birthrate which was historically higher. Distributions with very long scale times (either increasing or decreasing) would be difficult to distinguish from a constant birthrate. Note that in all cases the numbers of early T dwarfs are much smaller than those for late T dwarfs. This appears counterintuitive as early T dwarfs are brighter and hence more detectable. However, as the atmospheric chemistry of early T dwarfs changes quickly with effective temperature the spectral types T0-T4 cover a very small region of an effective temperature distribution (barely 100K, see Figures 6.6 and 6.7). Hence even though late T dwarfs are more difficult to detect than early T dwarfs, their larger temperature spread (and hence higher numbers) lead to a greater number of detections.

Simulated constraints of the UKIDSS LAS survey

In Section 6.4, a method for constraining the values of α and β was introduced. This utilised a grid of simulated colour distributions to produce a probability surface. Here

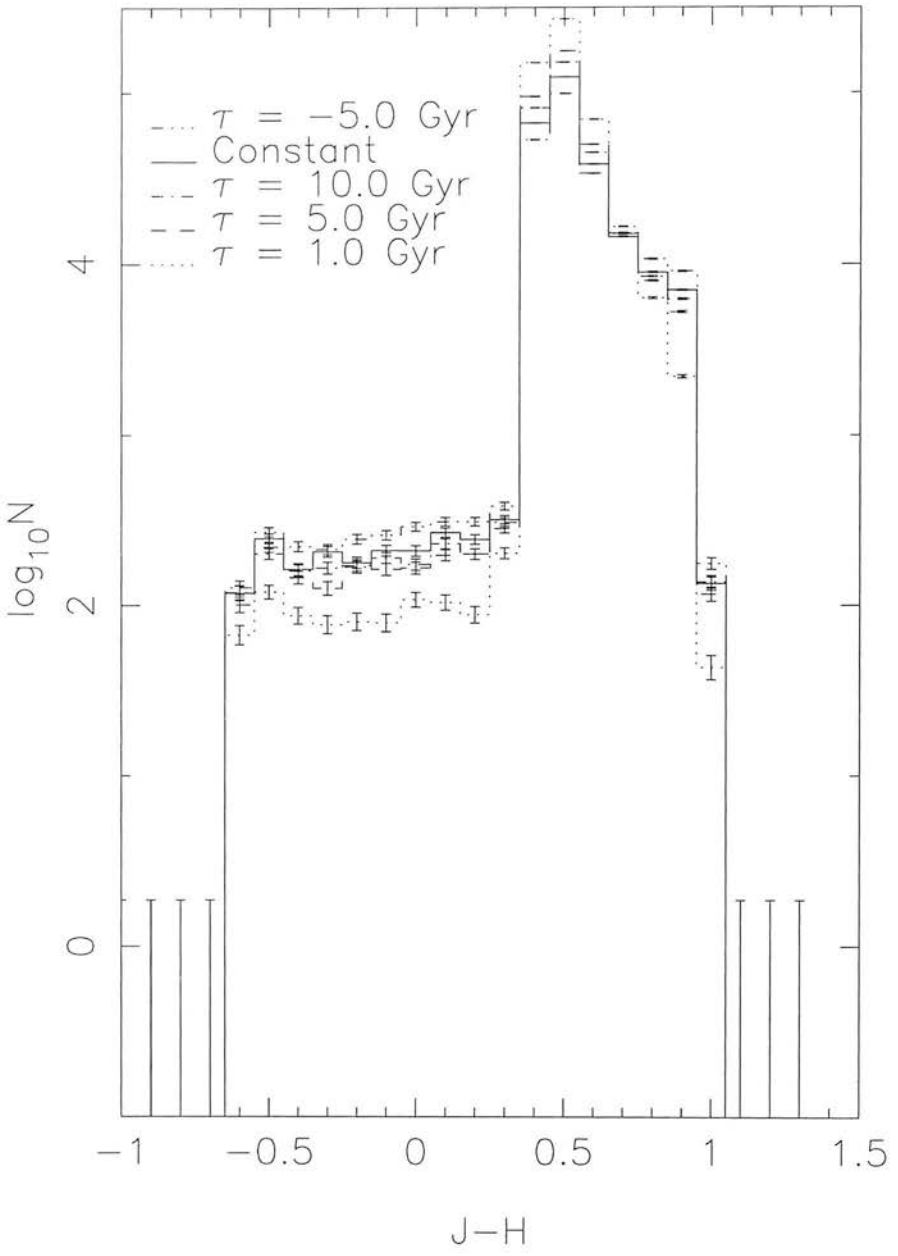

Figure 6.15: The alteration of the colour distribution caused by different birthrates. A log–normal Mass Function is used here. Note the large step around $(J - H) = 0.4$. This marks the boundary between the Ys and mid-late Ts (to the left) and the L and early Ts (to the right). J and H magnitudes are on the MKO system (Tokunaga et al. 2002; Simons & Tokunaga 2002).

Table 6.3: The calculated values for α and β for a range of different input values.

Input α	Input β	Calculated α	Calculated β
0	0	0.021 ± 0.060	0.003 ± 0.015
-1	0	-1.038±0.042	0.012±0.009
0	-0.1	0.031±0.056	-0.094±0.017

a series of $J - H$ histograms with known input values of α and β resulting from an LAS-like survey were simulated. These could be compared to a grid of such simulations to predict the potential constaints that could be set by such a survey. Three input sets of input values were, $\alpha = 0$ and $\beta = 0$, $\alpha = -1$ and $\beta = 0$ and $\alpha = 0$ and $\beta = 0.1$. Each had their own fine grid simulated and the resulting constraints are shown in Table 6.3. The probability distributions are shown in Figure 6.16 ($\alpha = 0, \beta = 0$), Figure 6.17 ($\alpha = -1, \beta = 0$) and Figure 6.18 ($\alpha = 0, \beta = -0.1$). The first thing that becomes apparent is that the noise on these finer grids means that there is not a smooth probability distribution. However it is obvious that there is a degeneracy between α and β.

This method could prove very useful in determining both the mass fucntion and birthrate from LAS data. The potential constraints (and how they relate to those from current works, including this one) are shown as an α plot in Figure 6.19. However binarity has not been taken into account in these simulations. The level of unresolved binarity will provide another parameter to characterise the results of the LAS. Furthermore, the simulations do not take contamination of the sample into account. Photometric errors will scatter objects such as hotter stars and white dwarfs across colour–colour diagrams so that they have colours similar to ultra–cool dwarfs. This contamination will have to be quantified in order for accurate comparisons to be made with the simulations. The quasar locus crosses the ultra–cool dwarf locus on a $(J - H)$ versus $(H - K)$ plot (e.g. Leggett et al. 2005), and such objects may also cause contamination of the ultra–cool dwarf sample. However Hewett et al. (2006) have produced a method to separate quasars from ultra–cool dwarfs using SDSS (Adelman-McCarthy & et al., 2006) photometry, and this should minimize quasar contamination.

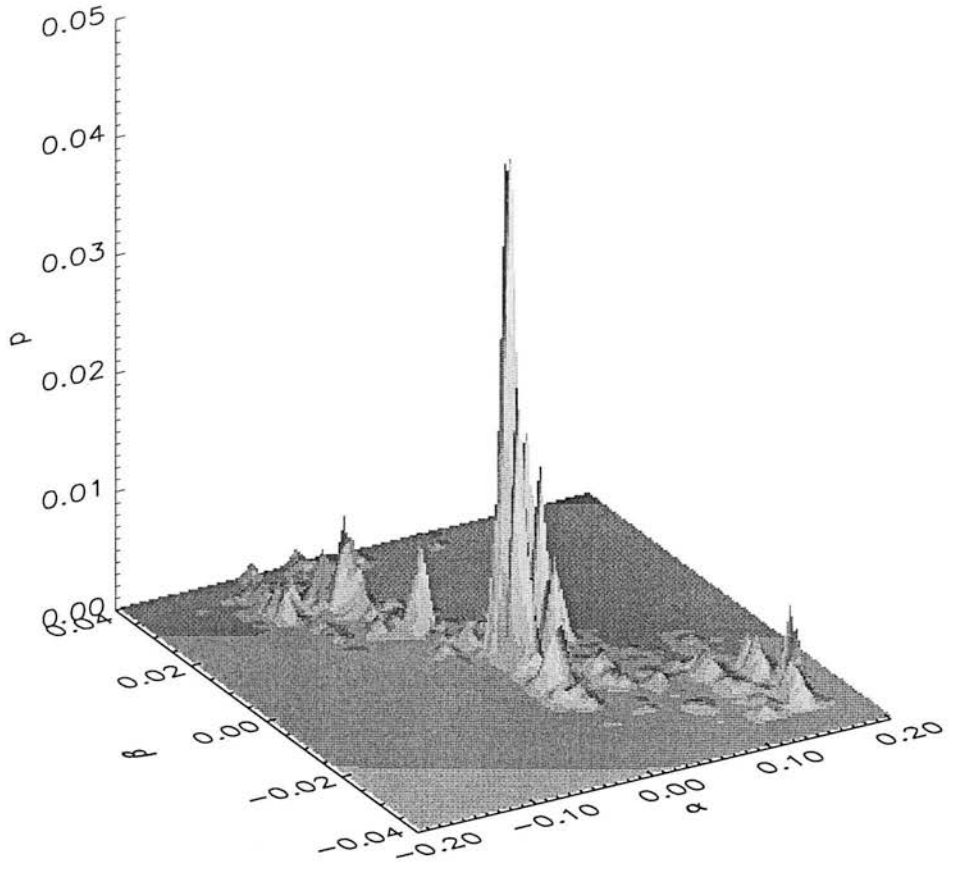

Figure 6.16: The probability surface produced by comparing an $\alpha = 0$, $\beta = 0$ distribution to a finer grid around the peak of the coarse grid. There is clearly a degeneracy between α and β.

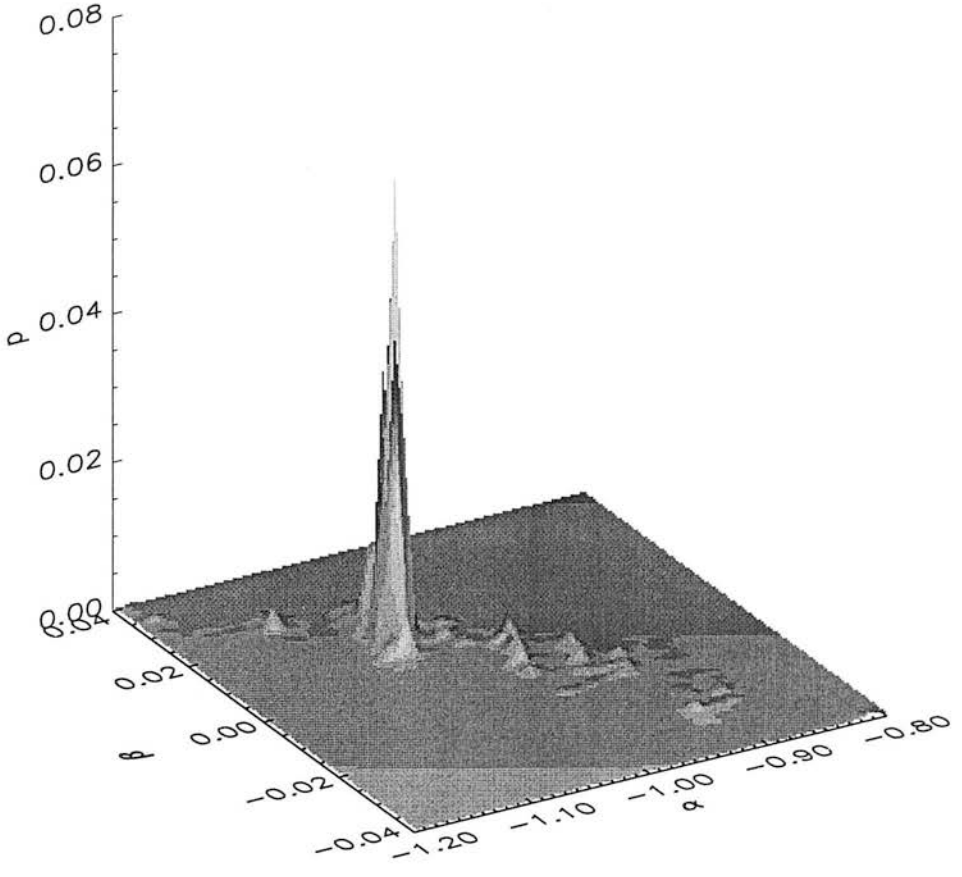

Figure 6.17: The probability surface produced by comparing an $\alpha = -1$, $\beta = 0$ distribution to a finer grid around the peak of the coarse grid. The degeneracy between α and β can be seen.

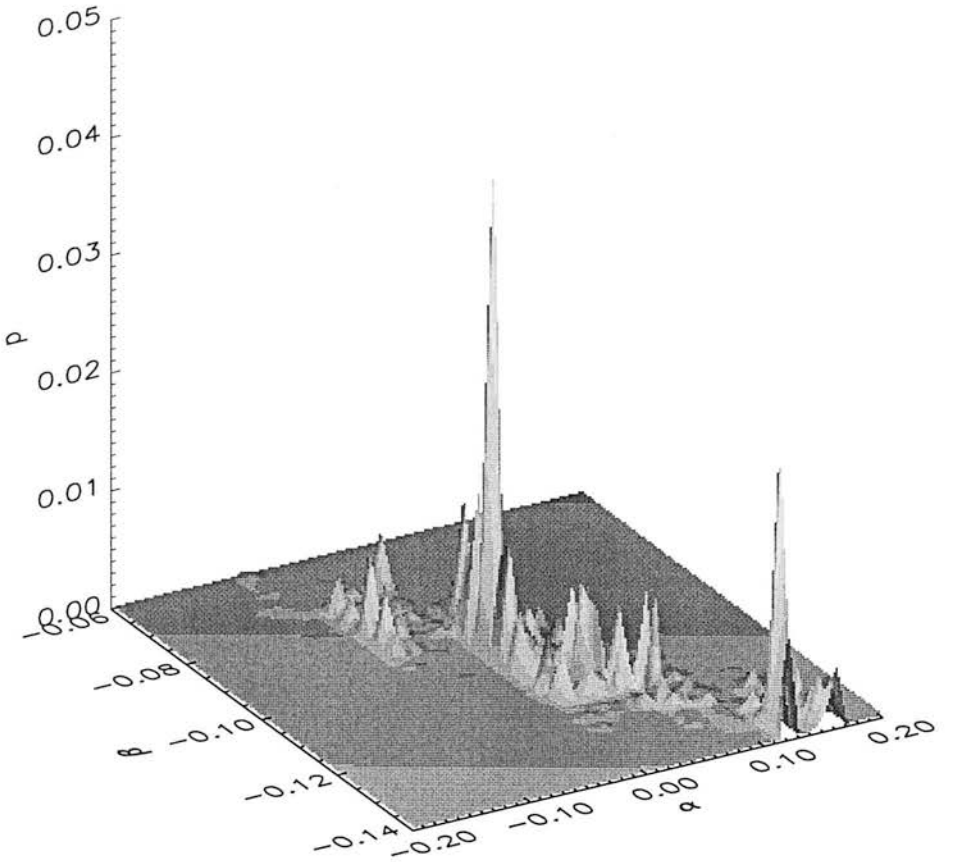

Figure 6.18: The probability surface produced by comparing an $\alpha = 0$, $\beta = -0.1$ distribution to a finer grid around the peak of the coarse grid. Again the degeneracy between α and β is clear.

Simulated results of the UKIDSS UDS survey

The UDS is a deep pencilbeam survey, covering 0.77 sq. degrees, primarily designed for extragalactic studies. For this purpose it uses the J, H and K passbands down to depths of $J = 25$, $H = 24$ and $K = 23$. This presents a problem when trying to detect ultra–cool dwarfs. T and Y dwarfs have similar near infrared colours to main sequence stars due to methane absorption around two microns. Hence with only J, H and K photometry detection can be difficult. Luckily for the study of ultra–cool dwarfs the area covered by the UDS is also covered by the Subaru/XMM-Newton Deep Survey (SXDS) which provides optical photometry. This will make it easier to distinguish ultra–cool dwarfs from other objects. Of course, many of the individual ultra–cool dwarfs found in the UDS will be too faint for spectroscopic follow-up observations. However they will still contribute to the observed sample. Note that this survey is so deep that the Galactic disk scale length had to be taken into account along with the scale height; a value of 3.5kpc (de Vaucouleurs & Pence, 1978) was used. The results are shown in Table 6.4, where it is shown that a few tens of T dwarfs, a few hundred L dwarfs and a handful of Y dwarfs will be detected. While this sample will not be as useful as that of the LAS for studying the IMF, birthrate and spectroscopic properties of these objects, it may provide valuable data on their distribution within the Galaxy.

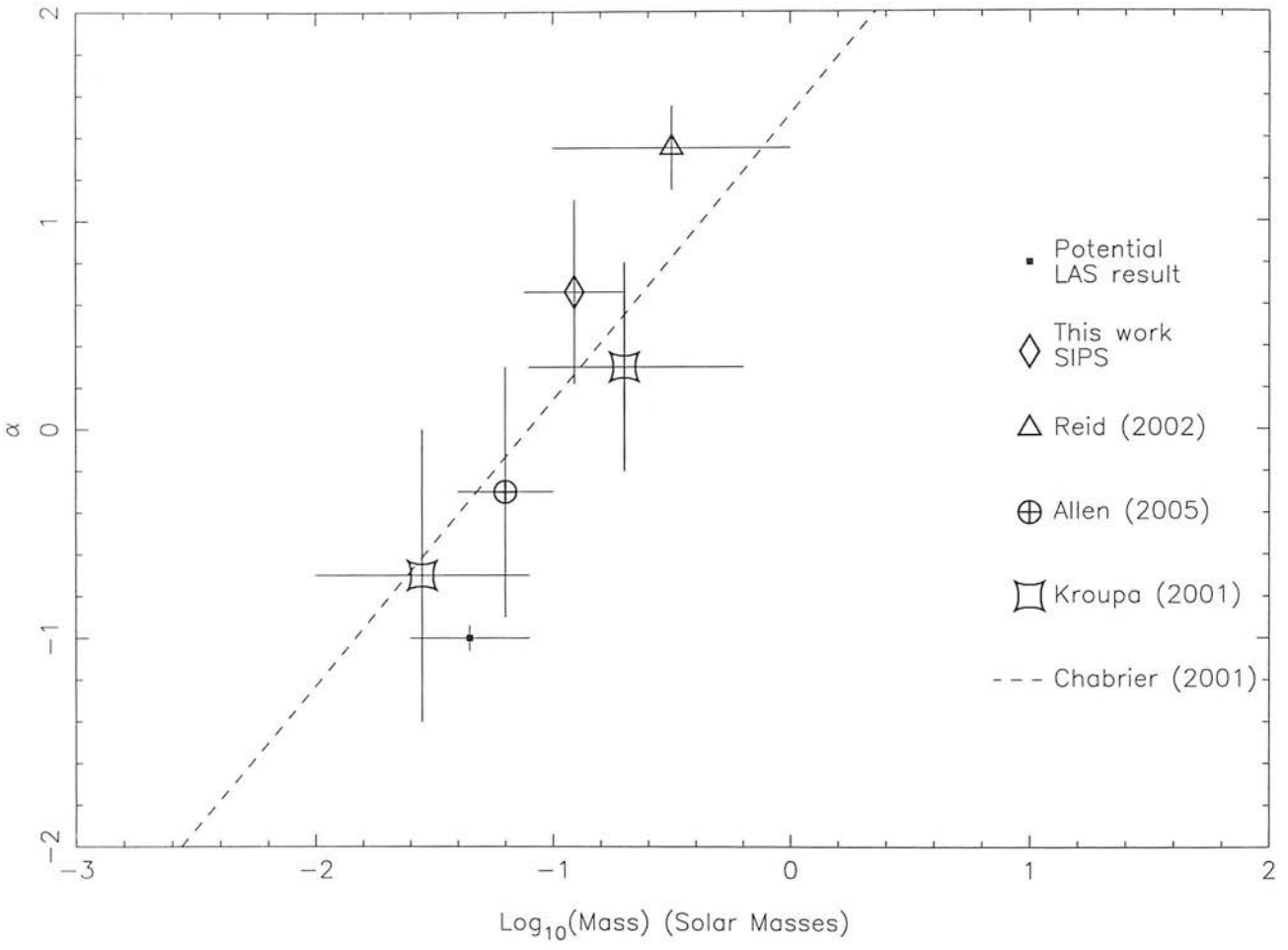

Figure 6.19: A plot showing the results of different studies of the mass function along with the result from SIPS and the potential LAS results. The values of α are shown along with their errors. The error bars in the x-axis represent a range in mass rather than an error. Only studies of the mass function in the field are shown here. Note the α value of -1 for the LAS data point is chosen arbitrarily and does not reflect any real result. The range is chosen to go from the substellar limit, down to around $0.0025 M_{\odot}$ below which few objects passed the survey selection. The constraints from the Cruz Luminosity Function are not shown as they are an order of magnitude bigger than the others in the plot.

Table 6.4: Predicted numbers of objects of different spectral types, for various birthrates and IMFs, in the seven year UKIDSS UDS.

Mass Function	Birthrate	Early L Dwarfs	Late L Dwarfs	Early T Dwarfs	Late T Dwarfs	Y Dwarfs
Log–normal	Constant	129	72	26	102	21
$\alpha = 0$	Constant	228	135	42	208	58
$\alpha = -0.5$	Constant	72	34	14	47	7
$\alpha = -1$	Constant	85	43	12	45	4
Log–normal	$\tau = -5.0$	103	69	23	106	15
Log–normal	Constant	129	72	26	102	21
Log–normal	$\tau = 10.0$	250	113	37	129	23
Log–normal	$\tau = 5.0$	288	103	39	125	23
Log–normal	$\tau = 1.0$	465	59	24	66	3

Chapter 7

Conclusions and Future Work

The work presented here shows that widefield surveys for cool dwarfs can be used not only to discover small numbers of interesting individual objects (as previous surveys have done), but also to produce large samples which can be used to constrain fundamental distributions used in both Galactic evolution and star formation.

Using the SIPS survey, over 7000 stars with proper motions greater than one tenth of an arcsecond per year have been identified. Among these are SIPS1259–4336 which appears to lie within 10pc and 44 common proper motion systems. Additionally 22 red objects which are candidate L dwarfs have been identified, although many have already been found by other surveys.

Detailed simulation of the survey results has allowed constraints to be set on the mass function parameter α (0.66 ± 0.44 in the range $0.2\mathrm{M}_{\odot} > m > 0.075\mathrm{M}_{\odot}$) and on the density of objects in the range $0.09\mathrm{M}_{\odot} < m < 0.1\mathrm{M}_{\odot}$ ($0.0053 \pm 0.0002/\mathrm{pc}^3$). A questionable constraint of -0.01 ± 0.10 has been placed on the birthrate parameter β. The result for α is more accurate than those from comparable surveys in the field and fits nicely into the general trend of results found by other authors. The stellar density result is also in good agreement with previous studies.

7.1 Future Work

The most obvious way to continue this work is to utilise new datasets to yield large samples of cooler objects. The UKIDSS LAS provides such a dataset and proper motion

surveys using both its two J epochs or the first J epoch along with 2MASS data could be carried out. The planned VISTA Hemisphere Survey will also allow an infrared proper motion survey of the southern hemisphere, while primarily optical datasets such as the SDSS Adelman-McCarthy & et al. (2006), PannSTARRS and GAIA Perryman et al. (2001) could also be used.

Additional follow-up observations could also be carried out on individual SIPS objects. One such study has been proposed by Nicholas Law and Simon Hodgkin. They are hoping to use the SIPS sample to identify close binary systems in a similar manner to those found in Law et al. (2006).

Finally with bigger samples it will be possible to add more parameters to the simulations. The most obvious shortcoming of current results is that they do not take unresolved binary systems into account. With a larger sample this could be added as an additional parameter allowing not only a more accurate constraint on other parameters, but also a constraint on the unresolved binarity itself. The mass function could also be approximated as a two parameter log-normal fit rather than a single power law. Additionally models in which the metalicity of objects changes with formation time would make the simulations more realistic.

Bibliography

Ackerman A.S., Marley M.S., 2001, ApJ, 556, 872

Adams F., Fatuzzo M., 1996, ApJ, 464, 256

Adelman-McCarthy J., et al., 2006, ApJSS, 162, 38

Allen P., Trilling D., Koerner D., Reid I., 2003, ApJ, 595, 1222

Allen P., Koerner D., Reid I., Trilling D., 2005, ApJ, 625, 385

Baraffe I., Chabrier G., Allard F., Hauschildt P.H., 1998, A&A, 337, 403

Baraffe I., Chabrier G., Barman T., Allard F., Hauschildt P., 2003, A&A, 402, 701

Bate M., Bonnell I., 2005, MNRAS, 356, 1202

Béjar V.J.S., et al., 2001, ApJ, 556, 830

Berriman G., Reid I., 1987, MNRAS, 227, 315

Bessell M., 1986, PASP, 98, 1303

Biller B.A., Kasper M., Close L.M., Brandner W., Kellner S., 2006, ApJ, 641, L141

Boesharr P., 1976, The spectral classification of M dwarf stars. Ph.D. thesis, Ohio State Univ.

Boissier S., Prantzos N., 1999, MNRAS, 307, 857

Bonnell I.A., Bate M.R., 2006, MNRAS, 370, 488

Burgasser A., 2004, ApJSS, 155, 191

Burgasser A., Kirkpatrick J., Leibert J., Burrows A., 2003, ApJ, 594, 510

Burgasser A., Kirkpatrick J., McGovern M., McLean I., Prato L., Reid I., 2004a, ApJ, 604, 827

Burgasser A., McElwain M., Kirkpatrick J., Cruz K., Tinney C., Reid I., 2004b, AJ, 127, 2856

Burgasser A., et al., 2002, ApJ, 564, 421

Burgasser A.J., Marley M.S., Ackerman A.S., Saumon D., Lodders K., Dahn C.C., Harris H.C., Kirkpatrick J.D., 2002, ApJ, 571, L151

Burrows A., et al., 1997, ApJ, 491, 856

Chabrier G., 2001, ApJ, 554, 1274

Chabrier G., 2003a, PASP, 115, 763

Chabrier G., 2003b, PASP, 115, 763

Chabrier G., Baraffe I., 1997, A&A, 327, 1039

Chabrier G., Baraffe I., Allard F., Hauschildt P., 2000, ApJ, 542, 464

Chiu K., Fan X., Leggett S.K., Golimowski D.A., Zheng W., Geballe T.R., Schneider D.P., Brinkmann J., 2006, AJ, 131, 2722

Close L., et al., 2005, Nature, 433, 286

Cruz K., Reid I., Liebert J., Kirkpatrick J., Lowrance P., 2003, AJ, 126, 2421

Dahn C., Harris H., Vrba F.J. e.a., 2002, AJ, 124, 1170

Deacon N., Hambly N., 2006, MNRAS, 371, 1722

Deacon N., Hambly N., 2007a, A&A

Deacon N., Hambly N., 2007b, A&A

Deacon N., Hambly N., Cooke J., 2005a, A&A, 435, 363

Deacon N., Hambly N., T.J. H., J.P. S., M.A. B., 2005b, AJ, 129, 409

Deacon N.R., Hambly N.C., 2001, A&A, 380, 148

Deacon N.R., Hambly N.C., 2004, A&A, 416, 125

Delfosse X., et al., 1997, A&A, 327, L25

Dobbie P.D., Kenyon F., Jameson R.F., Hodgkin S.T., Hambly N.C., Hawkins M.R.S., 2002, MNRAS, 329, 543

Epchtein N., et al., 1994, ApSS, 217, 3

Fan X., et al., 2000, AJ, 119, 928

Förster Schreiber N.M., Genzel R., Lutz D., Sternberg A., 2003, ApJ, 599, 193

Geballe T.R., et al., 2002, ApJ, 564, 466

Giclas H.L., Burnham R., Thomas N.G., 1971, Lowell proper motion survey Northern Hemisphere. The G numbered stars. 8991 stars fainter than magnitude 8 with motions ¿ 0.26"/year. Flagstaff, Arizona: Lowell Observatory, 1971

Gizis J.E., Monet D.G., Reid I.N., Kirkpatrick J.D., Liebert J., Williams R.J., 2000, AJ, 120, 1085

Golimowski D., et al., 2004, AJ, 127, 3516

Gorlova N.I., Meyer M.R., Rieke G.H., Liebert J., 2003, ApJ

Grossman A., 1970, ApJ, 161, 619

Hambly N., Henry T., Subasavage J., Brown M., Jao W., 2004, AJ, 128, 437

Hambly N.C., Irwin M.J., MacGillivray H.T., 2001a, MNRAS, 326, 1295

Hambly N.C., et al., 2001b, MNRAS, 326, 1279

Henry D., et al., 2003, In Proceedings of the SPIE, vol. 4841, p. 63

Henry T., Subsavage J., Brown M., Beaulieu T., Hambly N., 2004, AJ, 128, 2460

Henry T.J., Jao W.C., Subasavage J.P., Beaulieu T.D., Ianna P.A., Costa E., Méndez R.A., 2006, AJ, 132, 2360

Henry, T.J., 2006, Website of the research consortium on nearby stars. http://www.chara.gsu.edu/RECONS/

Hewett P.C., Warren S.J., Leggett S.K., Hodgkin S.T., 2006, MNRAS, 367, 454

Innes R., Worsell W., Wood H., 1915, Union Obs. Circ., No. 30

Kendall T.R., Delfosse X., Martin E.L., Forveille T., 2004, A&A, 416, L17

Kendall T.R., Jones H.R.A., Pinfield D.J., Pokorny R.S., Folkes S., Weights D., Jenkins J.S., Mauron N., 2006, MNRAS, pp. 1334–+

Kirkpatrick J., et al., 2000, AJ, 120, 447

Kirkpatrick J.D., Henry T.J., McCarthy Jr. D.W., 1991, ApJSS, 77, 417

Kirkpatrick J.D., et al., 1999, ApJ, 519, 802

Kleinmann S., et al., 1994, Ap&SS, 217, 11

Knox R., Hawkins M., Hambly N., 1999, MNRAS, 306, 736

Kroupa P., 2001, In Deiters S., Fuchs B., Spurzem R., Just A., Wielen R., eds., Dynamics of Star Clusters and the Milky Way, vol. 228 of ASP Conference Series, p. 187

Krumholz R., McKee C., Klein R., 2005, Nature, 438, 332

Kumar S.S., 1963, ApJ, 137, 1121

Larson R., 1976, MNRAS, 176, 31

Larson R., 1981, MNRAS, 194, 809

Larson R.B., 1979, MNRAS, 186, 479

Lasker B.M., Sturch C.R., McLean B.J., Russell J.L., Jenkner H., Shara M.M., 1990, AJ, 99, 2019

Law N.M., Hodgkin S.T., Mackay C.D., 2006, MNRAS, 368, 1917

Lawerence A., et al., 2006, astro-ph/0604426

Leggett S., Allard F., Burgasser A., Jones H., Marley M., Tsuji T., 2005, In Proceedings of the 13th Cool Stars Workshop, ESA Special Publications Series

Lepine S., Shara M., 2002, AJ, 124, 1190

Lewis J.S., 1969, Icarus, 10, 365

Lodders K., Fegley B., 2002, Icarus, 155, 393

Lucas P.W., Roche P.F., Tamura M., 2005, MNRAS, 361, 211

Luhman K.L., Rieke G.H., 1999, ApJ, 525, 440

Luhman K.L., Stauffer J.R., Mamajek E.E., 2005, ApJ, 628, L69

Luyten W., 1941, NYASA, 42, 201

Luyten W., 1979, Luyten Half Arcsecond Catalogue. Ph.D. thesis, University of Minnesota, Minneaplois

Luyten W.J., 1968, MNRAS, 139, 221

Luyten W.J., 1980, NLTT Catalogue. Ph.D. thesis, Minneapolis: Univ. Minnesota

Luyten W.J., 1988, Ap&SS, 142, 17

Magazzu A., Martin E., Rebolo R., 1993, ApJ, 404, L17

Martín E.L., Delfosse X., Basri G., Goldman B., Forveille T., Zapatero Osorio M.R., 1999, AJ, 118, 2466

Martín E.L., Zapatero Osorio M.R., Barrado y Navascués D., Béjar V. J. S. andRebolo R., 2001, ApJ, 558, L117

Massey P., Hunter D., 1998, ApJ, 493, 180

Massey P., Johnson K., Degioia-Eastwood K., 1995, ApJ, 454, 151

McCaughrean M., Close L., Scholz R., Lenzen R., 2004, A&A, 413, 1029

McCluskey S., 1966, In Beer A., ed., Vistas in Astronomy, Oxford: Pergamon, vol. 7, p. 141

Miller G., Scalo J., 1979, ApJ, 41, 513

Montagnier G., et al., 2006, A&A, 460, L19

Moraux E., Bouvier J., Stauffer J.R., Cuillandre J.C., 2003, A&A, 400, 891

Motte F., André P., Neri R., 1998, A&A, 336, 150

Barrado y Navascués D., Bouvier J., Stauffer J.R., Lodieu N., McCaughrean M.J., 2002, A&A, 395, 813

Barrado y Navascués D., Stauffer J.R., Bouvier J., Jayawardhana R., Cuillandre J.C., 2004, ApJ, 610, 1064

N.C. H., A.C. D., M.J. I., MacGillivray H., 2001, MNRAS, 326, 1315

Nielsen E.L., Close L.M., Guirado J.C., Biller B.A., Lenzen R., Brandner W., Hartung M., Lidman C., 2005, Ast. Nach., 326, 1033

Padoan P., Nordlund A., 2002, ApJ, 576, 870

Padoan P., Nordlund A., Jones B., 1997, MNRAS, 288, 145

Perryman M.A.C., et al., 1997, A&A, 323, L49

Perryman M.A.C., et al., 2001, A&A, 369, 339

Pinfield D., Jones H., Lucas P., Kendall T., Folkes S., Day-Jones A., 2006, MNRAS, 368, 1281

Pokorny R., Jones H., Hambly N., 2003, A&A, 397, 575

Pozio F., 1991, Memorie della Societa Astronomica Italiana, 62, 171

Puget P.e.a., 2004, In Moorwood A., Masanori I., eds., Proceedings of the SPIE, vol. 5492, p. 978

Ramsay G., Hakala P., 2005, MNRAS, 360, 314

Reid I., Gizis J., Hawley S., 2002, AJ, 124, 2721

Reid I., et al., 2007, AJ

Reid I.N., Hawley S.L., 2005, New light on dark stars : red dwarfs, low-mass stars, brown dwarfs. New Light on Dark Stars Red Dwarfs, Low-Mass Stars, Brown Stars, by I.N. Reid and S.L. Hawley. Springer-Praxis books in astrophysics and astronomy. Praxis Publishing Ltd, 2005. ISBN 3-540-25124-3

Rocha-Pinto H.J., Scalo J., Maciel W.J., Flynn C., 2000, A&A, 358, 869

Ruiz M., Wischnjewsky M., Rojo P., Gonzalez L., 2001, ApJSS, 133, 119

Salpeter E., 1955, ApJ, 121, 161

Saumon D., Chabrier G., van Horn H.M., 1995, ApJS, 99, 713

Scalo J., 1986, In Fundamentals of Cosmic Physics, vol. 11, p. 1

Schmidt M., 1959, ApJ, 129, 243

Scholz R., Ibata R., Irwin M., Lehmann I., Salvato M. andSchweitzer A., 2002, MNRAS, 329, 109

Scholz R., McCaughrean M., Lodieu N., Kuhlbrodt B., 2003, A&A, 398, L29

Scholz R., Lodieu N., Ibata R., Beinayme O., Irwin M., McCaughrean M., 2004, MNRAS

Schonfeld E., 1886, In Eds Marcus and Weber's Verlag, Bonn (1886), pp. 0–+

Simons D., Tokunaga A., 2002, PASP, 114, 169

Skrutskie M., Cutri R., Stiening R.e.a., 2006, AJ, 131, 1163

Slesnick C., Hillenbrand L., Carpenter J., 2004, ApJ, 610, 1045

Stevenson D.J., 1991, ARA&A, 29, 163

Subasavage J.P., Henry T.J., Hambly N.C., Brown M.A., Jao W.C., Finch C.T., 2005, AJ, 130, 1658

Tokunaga A., Simons D., Vacca W., 2002, PASP, 114, 180

Tsuji T., 2005, ApJ, 621, 1033

Twarog B., 1980, ApJ, 242, 242

Van Rhijn P., 1936, Pub. Astr. Lab. Groningen

de Vaucouleurs G., Pence W., 1978, AJ, 83, 1163

Veltchev T., Nedialkov P., Borisov G., 2004, A&A, 426, 495

Vrba F., et al., 2004, AJ, 127, 2948

Wallace P., 2003, Starlink User Note No. 67.61: SLALIB: Postitional Astronomy Library. CCLRC/Rutherford Appleton Laboratory, PPARC

Wielen R., 1974, In Contopoulos G., ed., Highlights of Astronomy, Reidel, Dordrecht, vol. 3, p. 395

Wroblewski H., Costa E., 2001, A&A, 367, 725

Appendix A

Objects Identified in the SIPS Survey

The SIPS survey has identified over 7000 objects with proper motions greater than a tenth of an arcsecond per year. Details of these are given in the following tables. Table A.1 shows objects newly discovered in the SIPS–I sample. Table A.2 gives details of objects in the SIPS–I sample which had previously been found by other studies. Table C3 (which can be found on the CD along with Tables C3a, C4 and C4a) lists all the objects with proper motions between 0.1"/yr and 0.5"/yr found in the SIPS–II survey. Table C4 gives details of object with proper motions above 0.5"/yr identified in the SIPS–II sample. Tables C3a and C4a give details of any previous names for the objects in the corresponding table.

In all tables see Luyten (1979) for LHS objects, Luyten (1980) for NLTT objects, Pokorny et al. (2003) for LEHPM objects, Wroblewski & Costa (2001) for WT objects, Ruiz et al. (2001) for CE objects and Scholz et al. (2002) and references therein for APMPM objects.

Table A.1: New objects found in the SIPS–I survey. PA = Position Angle. Objects marked with * were simulatiously found by Subasavage et al. (2005).

Name	Position J2000	μ ("/yr)	PA (°)	$\sigma\mu$	I	J	H	K_s
SIPS0308–8212*	03 08 53.50 -82 12 34.9	0.511	28.900	0.0170	13.087	11.7040	11.14	10.894
SIPS1240–8209*	12 40 53.21 -82 09 03.9	0.541	276.700	0.0190	12.490	10.8550	10.196	9.933
SIPS2130–7710*	21 30 06.31 -77 10 36.2	0.653	118.100	0.0370	13.476	11.2920	10.666	10.365
SIPS1633–7603	16 33 57.58 -76 03 54.4	0.510	198.900	0.0550	16.655	14.2610	13.644	13.298
SIPS2150–7520	21 50 14.20 -75 20 34.7	1.019	106.000	0.0500	17.260	14.0560	13.176	12.673
SIPS0452–7322*	04 52 04.61 -73 22 03.6	0.582	54.200	0.0150	13.621	11.9760	11.442	11.124
SIPS0321–7046	03 21 14.80 -70 46 11.5	0.553	40.300	0.0250	11.746	10.3940	9.840	9.574
SIPS1924–6920	19 24 35.60 -69 20 13.0	0.817	148.300	0.0420	14.267	12.3920	11.908	11.607
SIPS2032–6918	20 32 32.62 -69 18 56.4	0.585	147.200	0.0270	16.298	13.6360	12.983	12.579
SIPS1932–6506	19 32 36.39 -65 06 44.9	0.510	168.300	0.0300	14.784	12.6640	12.048	11.719
SIPS0052–6201	00 52 14.49 -62 01 55.1	1.123	82.800	0.0500	14.184	12.1530	11.742	11.370
SIPS1943–6125	19 43 33.11 -61 25 37.0	0.791	179.000	0.0340	16.115	13.1990	12.700	12.287
SIPS0523–5608	05 23 03.82 -56 08 42.5	0.683	341.800	0.0240	15.580	13.5540	12.948	12.602
SIPS1936–5502	19 36 01.69 -55 02 30.7	0.836	133.800	0.0510	17.474	14.4860	13.628	13.046
SIPS2053–5409	20 53 03.74 -54 09 33.7	0.722	158.100	0.0330	13.916	12.1700	11.656	11.345
SIPS2242–4514	22 42 04.80 -45 14 57.1	0.836	280.500	0.2250	17.501	15.9810	15.586	15.120
SIPS1410–4425	14 10 41.08 -44 25 55.9	0.537	195.900	0.0240	17.980	15.8740	15.066	14.544
SIPS1259–4336	12 59 03.87 -43 36 22.1	1.133	104.000	0.0210	12.799	10.5340	9.954	9.520
SIPS0641–4322	06 41 18.30 -43 22 36.2	0.689	19.200	0.0400	17.170	13.7510	12.941	12.451
SIPS1337–4311	13 37 56.25 -43 11 28.2	0.552	227.400	0.0460	12.850	11.7010	11.112	10.794
SIPS1910–4132	19 10 33.49 -41 32 38.8	0.738	174.700	0.0160	12.577	11.1470	10.552	10.249
SIPS1231–4018	12 31 21.55 -40 18 37.1	0.679	274.000	0.0330	11.538	10.4440	9.940	9.635
SIPS1149–4012	11 49 50.12 -40 12 42.0	0.566	253.200	0.0340	17.269	13.9990	13.322	12.834
SIPS0013–3921	00 13 00.54 -39 21 19.9	0.522	102.700	0.0330	17.551	14.7870	14.216	13.809
SIPS1251–3846	12 51 32.08 -38 46 13.1	0.593	278.900	0.0360	13.758	12.0860	11.558	11.246
SIPS0031–3840	00 31 18.84 -38 40 35.1	0.568	96.800	0.0350	17.442	14.1010	13.399	12.924
SIPS1039–3819	10 39 32.57 -38 19 57.2	0.724	203.600	0.0350	12.535	10.8460	10.30	9.998
SIPS1338–3752	13 38 28.14 -37 52 50.2	1.278	269.600	0.0140	13.141	11.7470	11.281	10.965
SIPS1141–3624	11 41 21.05 -36 24 38.3	0.556	57.100	0.0130	10.108	8.4900	7.967	7.699
SIPS1541–3609	15 41 19.25 -36 09 10.5	0.507	263.700	0.0380	14.467	11.9700	11.450	11.109
SIPS1342–3534	13 42 22.47 -35 34 47.9	0.931	259.100	0.0150	14.790	13.7550	13.216	12.935
SIPS2050–3358	20 50 44.01 -33 58 37.5	0.510	120.400	0.0220	15.858	13.8150	13.146	12.854
SIPS0417–3211	04 17 58.82 -32 11 49.4	0.855	283.700	0.1110	17.562	14.8640	14.196	13.739
SIPS2346–3153	23 46 54.50 -31 53 50.5	0.649	134.900	0.0430	15.838	13.2790	12.680	12.198
SIPS0405–3138	04 05 29.44 -31 38 44.6	0.846	261.200	0.0530	13.978	12.9240	12.282	11.989
SIPS2314–2929	23 14 26.40 -29 29 52.8	0.620	132.700	0.0430	17.329	14.6080	14.101	13.682
SIPS1529–2907	15 29 14.08 -29 07 28.8	1.078	185.800	0.0250	15.475	13.3190	12.855	12.499
SIPS1548–2859	15 48 21.55 -28 59 33.9	0.546	219.000	0.0520	15.468	13.1180	12.551	12.260
SIPS2313–2826	23 13 59.28 -28 26 36.9	0.825	117.500	0.0540	14.499	12.6600	12.149	11.878
SIPS0422–2802	04 22 31.25 -28 02 30.6	0.914	281.500	0.0770	16.250	14.7550	14.091	13.775
SIPS2231–2756	22 31 22.38 -27 56 47.3	1.677	105.800	0.4070	17.859	15.8080	15.318	14.903
SIPS1025–2730	10 25 55.01 -27 30 59.6	0.502	223.900	0.0410	16.699	14.5510	14.048	13.625
SIPS2157–2726	21 57 54.53 -27 26 28.8	0.855	131.400	0.0530	17.914	14.6720	13.887	13.401
SIPS2308–2721	23 08 11.23 -27 21 59.1	0.597	124.700	0.0670	17.819	14.6620	13.833	13.332
SIPS1019–2707	10 19 24.68 -27 07 17.3	0.582	272.300	0.0440	16.753	13.5260	12.906	12.471
SIPS1540–2613	15 40 30.18 -26 13 35.4	1.623	224.900	0.0210	14.600	11.6460711.145	10.730	
SIPS1424–2535	14 24 53.94 -25 35 17.9	0.641	105.500	0.1750	17.751	15.6650	15.123	14.784
SIPS1627–2518	16 27 49.75 -25 18 13.5	0.582	210.800	0.0150	17.706	14.8880	14.368	14.016

Name	Position J2000	μ ("/yr)	PA (°)	$\sigma\mu$	I	J	H	K_s
SIPS1513–2243	15 13 59.26 -22 43 47.6	0.574	206.400	0.0260	17.064	14.1960	13.601	13.231
SIPS1250–2121	12 50 52.43 -21 21 11.4	0.578	126.000	0.0420	13.336	11.1600	10.550	10.128
SIPS0921–2104	09 21 13.97 -21 04 38.1	0.965	162.600	0.0160	16.031	12.7790	12.152	11.690
SIPS0004–2058	00 04 41.17 -20 58 30.3	0.826	90.600	0.1070	15.647	12.4040	11.834	11.396
SIPS2359–2007	23 59 57.48 -20 07 37.6	0.798	127.700	0.0400	17.380	14.3820	13.623	13.248
SIPS2210–1952	22 10 50.04 -19 52 22.1	0.830	188.600	0.0510	16.456	14.0000	13.498	13.151
SIPS1048–1925	10 48 18.98 -19 25 33.3	0.957	264.400	0.1120	17.830	14.8760	14.276	13.692
SIPS1121–1653	11 21 09.57 -16 53 52.1	0.602	204.800	0.0473	13.856	12.5530	12.073	11.762
SIPS0227–1624	02 27 10.17 -16 24 46.2	0.592	120.800	0.0190	16.711	13.5730	12.630	12.143
SIPS1109–1606	11 09 27.58 -16 06 50.4	0.520	233.900	0.0500	17.856	14.9700	14.348	13.892
SIPS0933–1602	09 33 49.78 -16 02 50.7	1.357	188.300	0.0720	15.307	12.7200	12.232	11.890
SIPS0050–1538	00 50 24.35 -15 38 20.0	0.674	227.300	0.0420	16.880	13.7790	13.077	12.647
SIPS0258–1220	02 58 35.03 -12 20 18.3	0.827	91.400	0.0420	15.822	13.9210	13.410	13.030
SIPS1413–1201	14 13 05.33 -12 01 22.4	0.715	237.200	0.0250	10.446	9.0400	8.453	8.163
SIPS1542–1007	15 42 25.44 -10 07 02.3	0.552	166.000	0.0620	16.859	14.3720	13.801	13.437
SIPS2025–0835	20 25 47.58 -08 35 29.0	0.578	151.800	0.0520	15.699	13.1530	12.403	12.029
SIPS1956–0422	19 56 50.17 -04 22 39.3	0.563	115.000	0.0260	16.949	13.4410	12.921	12.510
SIPS0820–0355	08 20 44.43 -03 55 04.5	0.594	146.600	0.1230	17.319	15.8840	15.257	15.025
SIPS0346–0218	03 46 11.89 -02 18 18.1	0.850	155.400	0.0210	15.255	13.1300	12.642	12.346
SIPS0937–0214	09 37 31.35 -02 14 32.4	0.528	127.600	0.0250	16.979	14.4100	13.883	13.585
SIPS2343–0155	23 43 04.40 -01 55 06.0	1.359	279.400	0.2880	17.868	15.5980	15.044	14.757
SIPS1512–0112	15 12 17.92 -01 12 28.3	0.671	191.600	0.0310	16.607	15.2440	14.873	14.469

Table A.2: Previously known objects identified in the SIPS–I survey. PA = Position Angle.

Name	Position J2000	μ ("/yr)	PA (°)	$\sigma\mu$	I	J	H	K_s	Previous Name
SIPS1845–6357	18 45 02.32 -63 57 52.6	2.541	74.100	0.1530	12.528	9.5440	8.967	8.508	SCR 1845-6357
SIPS2256–6003	22 56 25.04 -60 03 44.4	1.020	206.600	0.0240	10.653	8.9840	8.360	8.108	LHS 532
SIPS1951–5055	19 51 31.35 -50 55 33.1	0.815	192.200	0.0330	12.288	10.9700	10.493	10.188	LHS 3492
SIPS0451–5818	04 51 37.56 -58 18 44.5	0.701	192.600	0.0250	13.980	11.6910	11.089	10.705	APMPM J0452–5819
SIPS0152–5747	01 52 00.00 -57 47 55.7	0.636	216.500	0.0370	13.213	11.4500	10.846	10.568	WT 60
SIPS2204–5646	22 04 09.46 -56 46 52.6	4.840	120.800	0.0480	16.567	11.9080	11.306	11.208	ϵ Indi B
SIPS0523–5607	05 23 30.59 -56 07 06.4	0.782	5.800	0.0290	13.960	12.3370	11.715	11.370	APMPM J0524–5607
SIPS0134–5511	01 34 59.74 -55 11 34.9	0.644	135.000	0.0420	15.211	13.2270	12.709	12.427	LEHPM 1683
SIPS0247–5256	02 47 20.63 -52 56 45.9	0.776	47.100	0.1020	13.097	11.7480	11.184	10.873	APMPM J0247–5257
SIPS0255–5140	02 55 14.27 -51 40 21.8	0.656	70.500	0.0940	11.125	9.9380	9.366	9.082	LHS 1471
SIPS0334–4953	03 34 08.52 -49 53 39.5	2.448	77.600	0.0550	13.916	11.3760	10.823	10.392	LEHPM 3396
SIPS0255–4700	02 55 03.18 -47 00 48.6	1.197	120.500	70.1260	17.025	13.2460	12.204	11.558	DENIS J0255–4700
SIPS2334–4044	23 34 15.53 -40 44 03.8	0.857	105.200	0.0230	12.683	11.2480	10.713	10.435	LHS 3971
SIPS0308–4006	03 08 49.00 -40 06 40.4	0.739	142.900	0.0580	13.925	12.6230	12.105	11.840	LHS 1502
SIPS1048–3955	10 48 15.39 -39 55 59.3	1.541	231.000	0.0130	12.097	9.5380	8.905	8.447	DENIS J1048–3956
SIPS0302–3950	03 02 06.56 -39 50 49.3	0.792	221.500	0.0250	11.926	10.7050	10.178	9.885	LHS 1490
SIPS2315–3733	23 15 51.15 -37 33 32.1	1.352	71.100	0.0840	11.556	10.4030	9.872	9.592	LHS 539
SIPS1155–3727	11 55 39.51 -37 27 32.5	0.868	172.500	0.0390	16.370	12.8110	12.040	11.462	2MASSWJ1155–3727
SIPS0319–3703	03 19 17.03 -37 03 42.0	0.818	124.800	0.0390	13.367	12.1600	11.676	11.344	LHS 1531
SIPS0306–3647	03 06 11.65 -36 47 50.3	0.571	179.800	0.2430	13.764	11.6900	11.068	10.631	LEHPM 3070
SIPS1011–3536	10 11 13.49 -35 36 21.6	0.509	293.200	0.0300	12.750	11.6660	11.070	10.807	CE 136
SIPS0105–3434	01 05 52.14 -34 34 48.5	0.607	92.200	0.0350	12.808	11.1600	10.569	10.272	LHS 1192
SIPS0212–3352	02 12 39.83 -33 52 06.1	1.045	93.500	0.0830	12.668	11.1410	10.625	10.319	LHS 1355
SIPS1203–3301	12 03 58.50 -33 01 26.8	0.768	275.400	0.0330	10.618	9.5290	9.073	8.744	LHS 2506
SIPS1045–3249	10 45 34.15 -32 49 53.5	0.551	306.600	0.0460	11.055	9.9869	9.233	8.966	CE 220

Name	Position J2000	μ ("/yr)	PA (°)	$\sigma\mu$	I	J	H	K_s	Previous Name
SIPS1406-3018	14 06 49.79 -30 18 27.6	0.852	264.300	0.0280	13.538	11.3610	10.687	10.366	APMPM J1407-3018
SIPS2039-2926	20 39 23.68 -29 26 30.6	0.832	154.100	0.0410	13.682	11.3570	10.743	10.367	LHS 3566
SIPS2123-2809	21 23 07.74 -28 09 54.4	0.715	132.900	0.0570	12.589	11.0620	10.523	10.247	LHS 3662
SIPS1223-2757	12 23 56.82 -27 57 48.4	1.247	282.900	0.0270	14.151	11.9770	11.401	11.069	APMPM J1224-2758
SIPS2331-2749	23 31 21.70 -27 49 53.6	0.781	1.439	0.1360	14.404	11.6460	11.055	10.651	APMPM J2331-2750
SIPS1158-2743	11 58 57.02 -27 43 07.5	0.501	295.400	0.0310	14.359	12.7630	12.238	11.963	LHS 2487
SIPS1456-2747	14 56 01.44 -27 47 34.7	0.821	197.300	0.0280	16.503	13.2500	12.655	12.189	2MASSJ1456-2747
SIPS1239-2658	12 39 36.56 -26 58 10.6	0.713	259.500	0.0360	11.424	10.0420	9.581	9.233	LHS 2597
SIPS1430-2403	14 30 18.06 -24 03 15.3	0.637	228.800	0.0620	11.857	10.7420	10.237	9.917	LHS 2928
SIPS0005-2157	00 05 48.18 -21 57 19.0	0.778	104.700	0.0450	16.461	13.2740	12.617	12.201	LEHPM 162
SIPS2333-2133	23 33 40.41 -21 33 51.9	0.794	103.200	0.0270	13.725	11.8580	11.312	10.929	LHS 3970
SIPS0024-2054	00 24 39.49 -20 54 09.1	0.507	198.700	0.0420	14.627	12.8730	12.312	12.014	LHS 1069
SIPS0009-1942	00 09 16.95 -19 42 34.5	1.093	60.800	0.0360	12.532	10.8830	10.327	10.074	LHS 105
SIPS2149-1810	21 49 23.86 -18 10 36.6	0.590	206.400	0.0520	13.994	12.5320	12.052	11.747	LHS 3718
SIPS2223-1736	22 23 06.98 -17 36 26.0	0.929	164.500	0.2400	9.268	8.2420	7.638	7.319	LHS 3799
SIPS0112-1659	01 12 30.28 -16 59 59.1	1.386	63.600	0.1600	8.523	7.2580	6.749	6.420	LHS 138
SIPS1507-1627	15 07 47.70 -16 27 37.5	1.038	182.400	0.2550	16.134	12.8300	11.895	11.312	2MASSJ1507-1627
SIPS0223-1616	02 23 01.78 -16 16 43.5	0.781	125.700	0.0330	15.159	13.4900	13.027	12.645	LHS 1396
SIPS1120-1439	11 20 26.46 -14 39 59.8	0.509	215.100	0.0380	14.877	13.4440	12.903	12.641	LHS 2397
SIPS0252-1431	02 52 39.40 -14 31 44.6	0.865	195.700	0.0420	14.094	12.6950	12.227	11.900	LHS 1462
SIPS2055-1403	20 55 35.92 -14 03 49.2	1.484	107.800	0.0130	11.248	9.7170	9.218	8.915	LHS 500
SIPS2228-1325	22 28 54.36 -13 25 19.1	1.222	209.100	0.1290	12.639	10.7680	10.217	9.843	LHS 523
SIPS1519-1245	15 19 11.90 -12 45 05.6	0.772	236.600	0.0770	9.640	8.5070	7.862	7.582	LHS 3056
SIPS2321-1137	23 21 13.24 -11 37 23.1	0.760	104.300	0.0480	13.986	12.2960	11.761	11.512	LHS 3935
SIPS2313-1106	23 13 19.35 -11 06 17.1	0.926	101.900	0.0720	12.866	11.1250	10.607	10.299	LHS 3911
SIPS1555-0955	15 55 15.28 -09 55 59.8	1.273	131.100	0.0220	16.057	12.5570	11.984	11.443	2MASSWJ1555-0956
SIPS2157-0928	21 57 39.27 -09 28 13.6	0.541	248.900	0.0610	12.019	10.4500	9.822	9.537	LHS 3735
SIPS1330-0842	13 30 03.00 -08 42 24.3	1.362	249.200	0.0410	10.731	9.5990	9.047	8.749	LHS 353
SIPS0335-0829	03 35 38.61 -08 29 22.9	1.748	112.200	0.0500	11.596	10.3770	9.801	9.456	LHS 176
SIPS1655-0823	16 55 35.58 -08 23 35.1	1.163	221.503	0.0310	11.595	9.7760	9.201	8.816	LHS 424
SIPS0006-0732	00 06 43.16 -07 32 18.5	2.063	201.300	0.1200	9.876	8.3230	7.792	7.439	LHS 2
SIPS1231-0638	12 31 23.99 -06 38 00.2	0.533	117.000	0.0450	12.527	11.3280	10.747	10.434	LHS 5217
SIPS1604-0616	16 04 20.02 -06 16 39.6	0.867	182.900	0.0280	11.683	10.4520	9.880	9.548	LHS 3149
SIPS1539-0520	15 39 41.61 -05 20 43.3	0.644	83.300	0.0420	17.805	13.9220	13.060	12.575	DENIS J1539-0520
SIPS2101-0523	21 01 53.75 -05 23 40.1	0.528	179.600	0.0250	14.000	12.8390	12.330	12.006	LHS 3611
SIPS0547-0512	05 47 08.98 -05 12 09.3	0.787	136.400	0.0370	11.096	10.0390	9.514	9.177	LHS 1785
SIPS1131-0503	11 31 26.85 -05 03 36.3	0.582	278.700	0.0290	15.216	13.6820	13.171	12.860	LHS 2419
SIPS2306-0502	23 06 28.98 -05 02 26.0	1.042	119.700	0.0250	13.580	11.3540	10.718	10.296	2MASSJ2306-0502
SIPS0246-0459	02 46 14.21 -04 59 08.8	2.488	137.900	0.0410	12.102	10.9700	10.499	10.152	LHS 17
SIPS0013-0457	00 13 46.38 -04 57 36.2	0.685	107.400	0.0390	13.925	11.4620	10.866	10.479	DENIS J0012-0457
SIPS0320-0446	03 20 28.43 -04 46 33.4	0.678	190.600	0.0380	16.558	13.2590	12.535	12.134	2MASSJ0320-0446
SIPS0214-0357	02 14 12.38 -03 57 42.8	0.504	105.000	0.0790	11.956	10.4810	9.858	9.485	LHS 1363
SIPS0251-0352	02 51 14.53 -03 52 36.3	2.185	149.300	0.0570	16.214	13.0590	12.254	11.662	2MASSJ0251-0352
SIPS1249-0317	12 49 48.72 -03 17 32.3	0.608	195.600	0.0490	11.874	10.7590	10.261	9.925	LHS 2641
SIPS1542-0315	15 42 30.00 -03 15 51.7	0.504	253.700	0.0270	14.941	12.6570	12.162	11.810	LHS 3104
SIPS0204-0152	02 04 27.97 -01 52 49.9	0.799	225.200	0.0130	10.744	9.5850	9.092	8.804	LHS 1332
SIPS0250-0150	02 50 06.29 -01 50 32.8	0.801	76.900	0.0210	14.520	12.9140	12.430	12.119	LHS 1451
SIPS1003-0105	10 03 19.26 -01 05 08.1	0.538	284.000	0.0600	14.774	12.3270	11.667	11.236	LHS 5165
SIPS1610-0040	16 10 28.93 -00 40 54.3	1.719	226.600	0.0880	14.903	12.9110	12.302	12.019	LSRJ1610-0040